ISAS - INTERNATIONAL SCHOOL
FOR ADVANCED STUDIES

October 1988

Spectral Classification
in
T Tauri stars

Thesis submitted for the degree of
"Magister Philosophiae"

Candidate
Mariagrazia Franchini

Supervisor
Prof. Roberto Stalio

TRIESTE

SISSA - SCUOLA
INTERNAZIONALE
SUPERIORE
STUDI AVANZATI
TRIESTE
Strada Costiera 11

October 1988

Spectral Classification in T Tauri Stars

Thesis submitted for the degree of "Magister Philosophiae"

Candidate

Mariagrazia Franchini

Supervisor

Prof. Roberto Stalio

CONTENTS

Preface 1

CHAPTER I - Pre–Main Sequence Stars: T Tauri Stars

§1.1 - *Introduction* 3

§1.2 - *Spectroscopic Characteristic* 5

§1.3 - *The Evolutionary State and Ages of the T Tauri Stars* 9

Tables 12

Figures 14

CHAPTER II - The T Tauri Phenomenon: The Veiling Problem

§2.1 - *Observational Evidence of Veiling* 21

2.1.1 - *Blue Veiling* 21

2.1.2 - *Differential Veiling* 24

§2.2 - *The Origine of the Veiling* 25

2.2.1 - *Photospere and Cromosphere* 27

2.2.2 - *The envelope* 31

2.2.3 - *Disks* 34

Figures 41

CHAPTER III - Data Reduction

§3.1 - *Introduction* 51

§3.2 - *Echelle Reduction* 52

3.2.1 - *MIDAS Reduction* 52

3.2.1.1 - *Order Definition* 54

3.2.1.2 - *Background Definition* 56

3.2.1.3 - *Flat Field Correction* 59

3.2.1.4 - *Order Extraction* 61
3.2.1.5 - *Wavelength Calibration* 62
3.2.1.6 - *Response Correction Using Standard Stars (Standard Method)* 65
3.2.1.7 - *Response Correction Using the Blaze Function (IUE–Like Method)* 66
3.2.2 - *IRAF Reduction* 67
§3.3 - *Comparison Between Standard and IUE–Like Reduction* 68
§3.4 - *Comparison Between MIDAS and IRAF Reduction* 66
Tables 72
Figures 75

CHAPTER IV - Spectral Classification Criteria

§4.1 - *Introduction* 92
§4.2 - *Spectral Type Classification* 92
4.2.1 - *First Rough Spectral Classification* 94
4.2.2 - *Spectral Type Criteria* 96
4.2.3 - *Effective Temperature by the Curve of Growth* 98
Tables 100
Figures 105
Conclusions and Future Work 116
References 120
Ackowledgements 126

Appendix A

Preface

In the last two decades there has been considerable progress in the theoretical understanding of the protostar phase in the star formation processes.

Model computations of the hydrodynamic evolution of protostars allow to obtain evolutionary tracks of protostars (see e.g. Appenzeller and Tscharnuter, 1975). According to these computation the low mass protostars should appear in the same general region of the HR-diagram where the T Tauri variables are observed. T Tauri stars are very young objects in which matter is probably still infalling and also being ejected from the stellar surface. Most authors suggest that these objects are the protostars predicted by the theoretical computations.

In order to learn more about the final stages of the formation and the very early stages of the evolution of the low mass stars we have started to study a sample of T Tauri stars in the Chamaeleon 1 and Chamaeleon 2 dark clouds. In particular, in the present work we will study the spectral classification problem for these stars. In a previous study (Franchini et al. 1988) we have derived the projected rotational velocities, $v * \sin i$, for the same sample of stars. In order to locate in the HR diagram the studied stars and thus interpret their evolutionary state, one has to know both bolometric luminosity and effective temperature. The spectral classification that we want to obtain will give us mostly informations on the effective temperatures; luminosity estimates must be obtained by other methods. Still, as we will see, the T_{eff} determination is a very complex task.

We have used échelle spectra obtained with the CASPEC spectrograph attached at the 3.6 m ESO telescope. A large fraction of this study concerns

the data reduction. Thus the analysis described in the last chapter of the thesis is only preliminar and some of the results have to be completed and checked. In the first chapter we make a brief review of the T Tauri stars in order to introduce these objects on the basis of published observational and theoretical studies. In Chapter II we will treat a particular aspect of the T Tauri stars which is directly related to the classification problem : the activity of T Tauri stars and its origin. In Chapter III we describe the data reduction procedures adopted and in Chapter IV we describe the spectral classification criteria that we have used and give the indications for future work.

CHAPTER I

Pre-Main Sequence Stars: T Tauri Stars

§1.1 *Introduction*

According to various recent catalogues (Herbig and Rao 1972, Cohen and Kuhi 1979, Appenzeller *et al.* 1983, Finkenzeller and Mundt 1984) we know at least 600 stars which are so young that energetically significant nuclear reaction have not yet started in their interior. These stars derive all or most of their luminosity from the compressional heating of a slow quasistatic gravitational contraction (e.g. Appenzeller, 1980).

Today these "contracting" or "pre-main sequence" (PMS) stars are usually divided into three distinct subgroups:

1. *T Tauri stars* - contracting stars with $M/M_{\odot} < 3$;
2. *Herbig - Ae - Be stars*: contracting stars of $4 < M/M_{\odot} < 7$;
3. *post - T Tauri stars* (PTT): $M/M_{\odot} < 3$ which are in an evolutionary state between the T Tauri and the main sequence stars.

T Tauri stars and PTT are well recognized as PMS star by the presence of atmospheric lithium (which is destroyed when the star reaches the main sequence), by their location in HR diagram and by their association with dense molecular clouds where very young OB stars, IR sources, H_2O masers, and other signs of recent or ongoing star formation.

The identification of Herbig – Ae – Be stars (which are the more massive than the PMS) is more difficult because the lithium criterion cannot be applied. Strom *et al.* (1972) and Finkenzeller and Mundt (1984) demonstrate by the presence of circumstellar dust and other observational characteristics that these objects are contracting stars too.

All known or suspected contracting stars have relatively low masses: $M/M_{\odot} <$ 7. This observational results is in good agreement with theoretical calculations which indicate that the contracting star should occur only if

$$t_{KH} \gg t_{acc}$$

where t_{KH} is the Kelvin-Helmoltz time scale and t_{acc} is the hydrodinamic accretion time scale which is of the order of or longer than the free-fall time scale t_{ff} (as defined e.g. in Appenzeller, 1980 and Spitzer, 1968)

Since $t_{KH} \sim M^{-3}$, and t_{ff} depends only on the initial density but not on the mass the condition:

$$t_{KH} \gg t_{ff} \qquad [1.1]$$

is obtained only for low mass stars.

In massive stars where

$$t_{KH} \ll t_{ff} \qquad [1.2]$$

the nuclear reactions start already in the hydrostatic cores of the hydrodynamically collapsing protostars. Then, these massive protostars arrive to the main sequence without a quasistatic contraction phase: they are not caracterized by the so called pre-main sequence phase.

We will discuss in this chapter the largest subgroup of the known contracting stars: the *T Tauri stars.*

The T Tauri stars show a large variety of spectral peculiarities and variability. They are relatively faint; the brightest has magnitude 10; most of the T Tauri stars are fainter than $12th$ magnitude. High quality observations are required in order to understand their characterictics. In the last few years, due to the possibilities of the modern instruments and the availability of sophysticated data reduction packages this has been done. As a result a coherent picture is emerging, although many major problems are still unsolved.

There are recent reviews to consult (e.g. Kuhi, 1983, Cohen 1984, Bertout 1984, Appenzeller 1985, Cohen 1988, Shu *et al.* 1988). In this chapter, we will try to give a general description of these objects in order have a general idea of the recent developments in this field.

§1.2 *Spectroscopic Characteristics*

There is little doubt today that T Tauri stars are young stellar objects of age from 10^5 to 10^7 years.

Herbig (1962) gave the classification criteria of T Tauri stars on the basis of their spectroscopic caracteristics. According to him the T Tauri stars display G, K, M, subgiants optical absorption spectrum superimposed by H_α emission and other emission lines. Subsequently Walker (1972) showed that they display an infrared excess relative to their main sequence counterparts, and Giampapa (1984) showed that the ultraviolet line fluxes are up by a factor 10^4 with respect to the corresponding fluxes in the Sun. X-ray luminosities of a factor 10^3 larger than the solar luminosities were measured by Gahm (1980), Feigelson and DeCampli (1981).

Other characteristics of the T Tauri stars are:

1. close association with dark clouds which leads to their identification with stars on pre-main sequence tracks which have recently become visible;
2. clear signs of mass loss and, in some cases of mass infall;
3. photometric variability with irregular light changes up to a few magnitudes and sometimes regular photometric modulation;
4. line spectrum variability, particularly in the stronger absorption lines and emission lines, with time-scales from minutes to years.

Most of the T Tauri stars have a classificable photospheric spectrum (Cohen

and Kuhi 1979). They are K or M stars, as espected from their position in the H–R diagram.

A closer inspection of the absorption line spectrum often reveals some abnormalities, especially in the stronger lines. In addition, the photospheric spectrum may be "filled in" by an apparently external source of continuum light, which acts differentially in the stronger and the weaker lines. This is what would be expected if the upper photosphere were a "hot chromosphere".

The lines which are classically ascribed to the chromosphere and transition region tend to show strong emission. These lines are the H and K CaII resonance lines (Fig. 1.2), the CaI infrared triplet lines, and the h and k Mg II resonance lines (Fig. 1.3). Other strong optical lines are seen in emission in the more active stars, including NaI, MgI, HeI, FeI and FeII, and others. To ascribe all these lines to classical stellar activity is an oversimplification. In particular, some of these lines also show narrow Doppler shifted components and the widths and shapes of these lines sometimes are quite different than would be expected from a classical active stellar chromosphere.

The Balmer lines are often found in emission, H_α is usually particularly intense.

H_α is the best studied feature of T Tauri spectra. The profile of this line can be very different: symmetric, asymmetric, double peaked with absorption components, etc. Fig. 1.4 shows some examples of H_α profiles taken from our sample. It is usually the most prominent feature in the spectrum, with emission equivalent widths sometimes as high as $100\mathring{A}$ (typically $\approx 10^{-11}\ erg \cdot cm^{-2} \cdot s^{-1}$ for a star with $V = 10.5$) or more. The profile extends over several hundred km/s on both sides of line center. The higher Balmer lines can be in absorption, even when H_α is reasonably strong. All the Balmer lines can be variable. The higher Balmer lines sometimes show inverse P Cygni profiles. An individual star

can display a variety of profile types.

The photospheric spectrum of these stars ranges from almost normal to completely absent (Fig. 1.1). The latter spectrum is that of the so called "extreme" T Tauri star caracterized by a anomalous activity compared to main sequence stars and the other "normal" T Tauri stars. It seems that the photospheric lines weaken as though an extra source of continuum light were present. This extra continuum is stronger in the blu part of the spectrum and is caracterized by the fact that the lines which are the strongest in a normal star tend to fill in faster than the weak line (see section 2.2). These two effects are called *blue veiling* and *differential veiling* respectively. The blue veiling can be seen seen at increasingly long wavelengths in the extreme stars. Eventually the absorption lines are completely masked. For this reason it could be difficult to assign a spectral type to the underlying star by using the photospheric spectrum. (e.g. Cohen and Kuhi, 1979, Vogel and Kuhi, 1981, Finkenzeller and Basri, 1985, etc).

This aspect of the activity of the T Tauri stars is particularly important for the present work. We will treat more accurately this point and we will present some of the accepted interpretations of the "veiling" problem. We note, however, that many questions are still open.

In the IUE spectral range lines (e.g. CII, CIV, SiII, SiIV, OI etc.) are often found strongly in emission. The observed value for the UV line fluxes is of the order of 10^4 times the solar value. But the lines corresponding to the highest temperature diagnostic (e.g. NV which corresponds to about $2 \cdot 10^5$ K) are weak or even absent in the strongest H_α emitters or where there is evidence of strong winds. Thus it is thought that mass loss could explain the lack of high temperature UV lines: the maximum temperature in the outer atmosphere does not reach coronal values. The available energy goes into driving a strong wind.

The UV spectrum (after dereddening) tends to show an excess compared

to inactive main sequence stars. This will be treated with more accuracy in Chapter II where we will present the observational evidences and some of the possible interpretations.

Observations with the Einstein satellite in X–rays have shown that at least in a number of TTS, the atmospheric gas reaches temperatures of order $10^6 K$ (Gahm 1980, Feigelson and De Campli 1981, Walter and Kuhi 1981). In those stars for which X–rays have been detected, the observations imply that the extension of the corona is small compared to the stellar radius.

Bouvier and Bertout (1985) found that the ratio of X-ray flux to CaII K line flux and the rotation period is related (Fig. 1.6). Although the sample used by Bertout and Bouvier was too small, and the uncertainties in the fluxes too large they noted a trend toward higher activity at shorter rotation periods.

Mendoza (1966) discovered that many T Tauri stars have strong "excess" radiation in the $1 - 3\ \mu$ region. The continuous emission rises well above the value expected from fitting a normal spectral energy distribution to the visual part of the spectrum. Mendoza proposed a model in which this excess arises in an optically thick circumstellar (CS) dust shell. The recent studies have confermed this idea.

In order to summarize the overall picture which is emerging, Basri (1987) has arranged the T Tauri stars into several distinct classes. Table 1.1 reports the observational properties of these classes and Table 1.2 gives the underlying physical motivations for the class distinctions. As Basri says - the T Tauri stars are very iconoclastic and many exceptions to most statements can be found, so the tables above should not be taken too literally.

Basically, the proposed model is that the newly emerging stars themselves have fairly normal, deep photospheres covered with very strong magnetic stellar activity. As one moves to the more active classes, one begins perhaps to see

increasing amounts of circumstellar material arranged primarily into bipolar outflows and equatorial disks. As the disks become more prevalent, one moves from the regime of "passive" (namely a disk which merely reprocesses the stellar light) orbiting material to continuing accretion into the star through the disk (section 2.2.3). As the accretion rate increases, the luminosity of the disk and its accompanying boundary layer (where the disk meets the stars) begins to overwhelm the stellar spectrum. First the disk appears in the infrared, then it begins to dominate the emission lines and the UV and blue region. In the most extreme cases, the star is no longer visible and all the light comes from the disk, boundary layer, and outflow regions.

So far, it is evident how the different physical regions and processes contribute to make the T Tauri phenomenon very complicate. In order to understand this, it is necessary to identify the processes which are operative on a given stars and to be able to separate their various effects in the spectrum. All this requires observations in the optical, infrared, and ultraviolet spectral regions which include both the overall continuum distribution and detailed line profiles. Even more, due to the variability, it is desirable to obtain all the data at the same time. The possibly to obtain this one has greatly increased these last years with the advent of the large telescopes, the échelle spectrometer, the efficient CCD detectors.

§1.3 *The Evolutionary State and Ages of the T Tauri Stars*

Usually it is possible to determine the evolutionary state and age of an individual star by locating the star into H–R diagram, namely by comparing the effective temperature and the bolometric luminosity observed with the corresponding theoretical values obtained with the evolutionary model computations.

But, even if the procedure is usually accepted for the most phases of stellar evolution, in the case of contracting stars this procedure has been criticized, since neither the "observed" stellar parameters neither theoretical models of PMS objects appear to be reliable.

The surface temperature of stars are normally determinated by a quantitative analysis of the photospheric absorption spectra by comparing it with the spectrum of a "standard star" of known photospheric temperature. But for the "veiling" problem (Chapter II and IV) a comparison with standard absorption spectra may be misleading. In second place the spectral type is usually converted into effective temperature by using a temperature scale appropriate to main sequence stars of luminosity class V (Cohen and Kuhi, 1979).

In order to obtain the bolometric luminosity we must integrate the emitted radiation over a wide range wavelengths. Due to the variabitity of these stars we should have all the data obtained simultaneusly at the same time. Usually this is not possible. Moreover, for the T Tauri stars the meaning of "stellar luminosity" is a bit subtle due to the presence of extended envelopes or disks (section 2.3).

On the other hand from a theoretical point of view the evolutionary tracks for PMS stars are not fully reliable. In fact they depend on the initial condition. Unfortunately relatively little is known on these initial conditions and all published conventional PMS computation are based on arbitrarily assumed initial models. In addition there are unexplained discrepancies between the computational results obtained for similar initial conditions by different authors. This is illustrated by Fig. 1.7 where computed (hydrodynamic) evolutionary tracks are compared. All the tracks assume that rotation and magnetic effects are negligible and all start from qualitatively similar initial conditions. While the tracks labeled AT and SST agree resonably well in the $L-T_{eff}$ range characterizing the T Tauri stars, the computations of WN resulted in considerably higher effective

temperature during the T Tauri stage. These discrepancies seems due to a subtle differences in the radiative transfer approximation during the earlier hydrodynamic phases. All the published models use crude approximations during the hydrodynamic phase so that none of these models may realistic. Furthermore, neglecting the effects of the magnetic fields alone may result in drastic changes of the evolutionary tracks.

Due to uncertainties discussed above, evolutionary ages and mass values derived from HR diagrams of T Tauri associations remain unreliable and may be affected by large systematic errors. In Fig. 1.8 the H-R diagram of the Taurus-Auriga stars of the Taurus-Auriga complex and the approximate PMS evolutionary tracks are also included. From this figure it is possible to see that small uncertainties on the bolometric luminosities produce a small effect on the mass estimate for most stars in Taurus-Auriga since they lie on the convective (almost vertical) tracks. However, small errors in temperature can move stars from one convective track to another. It is, therefore better to use the derived masses and ages for statistical purposes. Ages have even more problems than masses. By considering Fig. 1.9, typically T Tauri stars can be caracterized as roughly 1 $M_{\odot}$, age between a few 10^5 and 10^6 yr (in Taurus-Auriga). However, Stahler (1983) has shown that these ages tend to be significant understimated of the age of the youngest stars and that one should augment these ages by the duration of accretion phase.

We have pointed out only few of the several problems unsolved about the evolutionary state of the T Tauri stars; in order to improve this situation, more accurate theoretical models of the atmospheres and the interior of contracting stars are nedeed.

These improved models must include the effects of the T Tauri chromospheres, surface magnetic fields, and rotation.

Table 1.1: Observational Characteristics of Pre–Main Sequence Stars

	PMS 0	PMS 1	PMS 2	PMS 3	PMS 4
Absorp. lines	normal	strong lines filled in	differential line filling	blue (IR?) veiling	fully veiled
Ca II	narrow symmetric emission	strong narrow sym. emission	plus occaisional broad comp.	mostly broad asym. em.	very broad emission like Hα
UV lines and cont.	like active M.S. stars	see PMS 0	see PMS 1 or even more	add cont. excess	PMS 3 and more
Hα	normal	filled in or weak emission < 5Å eq.w.	broad, asym. em. with abs. ≥ 5Å (var.)	broader asym. wings, variable	very strong broad comps., variable
X-rays	coronal	coronal, strong flares	some coronae strong flares	fewer observed?	fewer observed
Infrared	normal	occaisional slight excess	excesses, var. slopes, var. levels	str. excess some flat spectra	more extreme, bright
Total Lumin.	L_{star}	L_{star}	$\leq 1.5L_*$	$>1.5L_*$	up to 15-20L_*

Table 1.2: PhysicalClassification of Pre–Main Sequence Stars

Class	Name (Abrv.) [Garb]	Physical Defining Characteristics
PMS 0	Post T Tauri (PTTS) ["just stepped out"]	radiative track active chromosphere, corona spinning up
PMS 1	Naked T Tauri (NTTS) [Negligé or less]	on convective track more active chromos., corona low to moderate mass loss (remnant dust)
PMS 2	T Tauri (TTS) [Bathing Suit]	PMS 1 + passive disk strong mass loss $L_{sys} \leq 1.5 L_*$
PMS 3	Classical TTS (TTS) [Evening Gown]	PMS 1 + active disk strong (bipolar?) flows $L_{sys} \sim 1 - 20 L_*$
PMS 4	Continuum Stars (C) [Chador]	Active disk masking PMS 1 bipolar flows, HH objects, jets (?) extended mass loss region

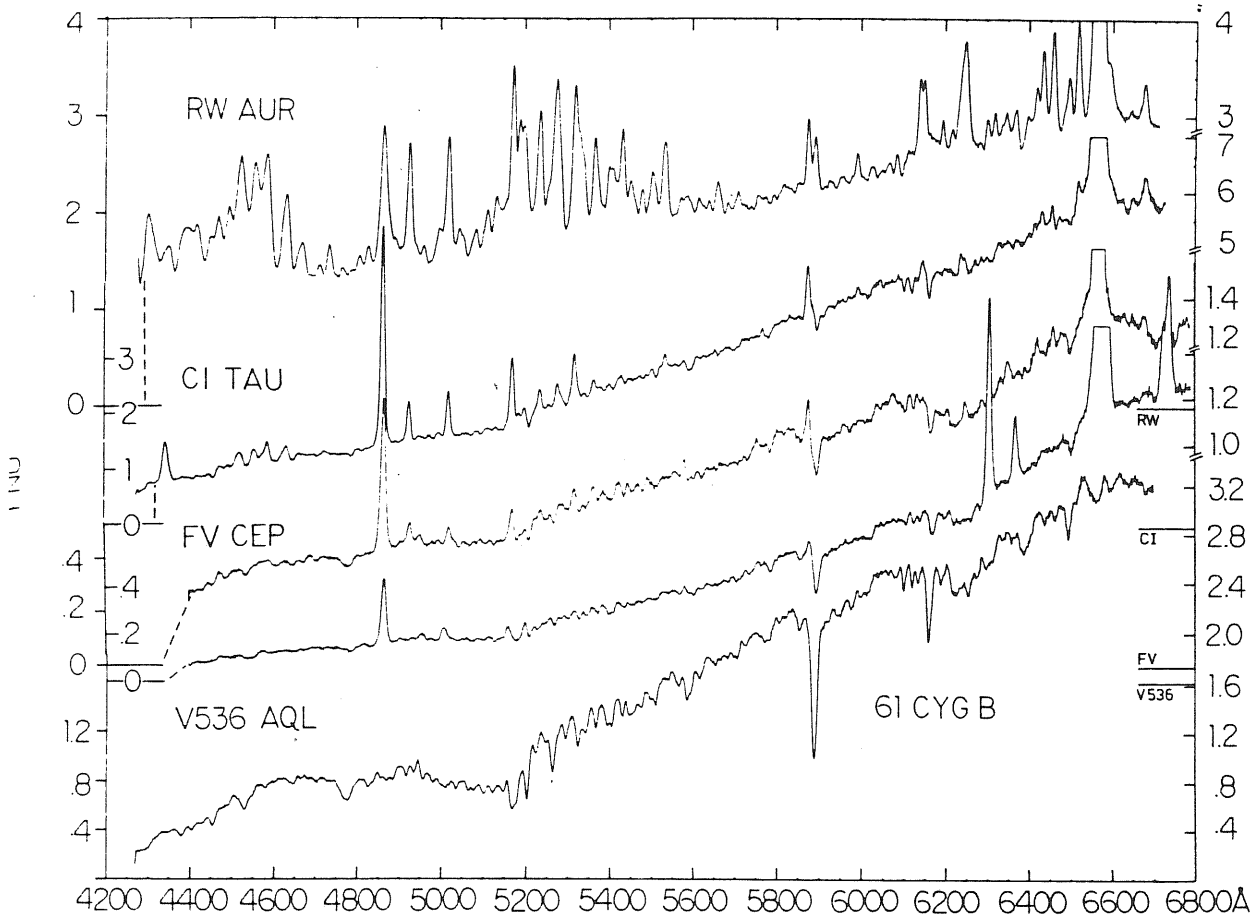

Fig. 1.1: A sequence of K7 photospheres (surface temperature 4000 K) beginning with the normal star 61 Cyg B, showing the effect of increasing emission lines upon the underlying stellar absorption features. The continuum star RW Aur completes the sequence, although no photospheric type can be assigned. The absorption near 5900$\AA$ is not photospheric; it arises from circumstellar cool neutral sodium gas (Cohen and Kuhi, 1979).

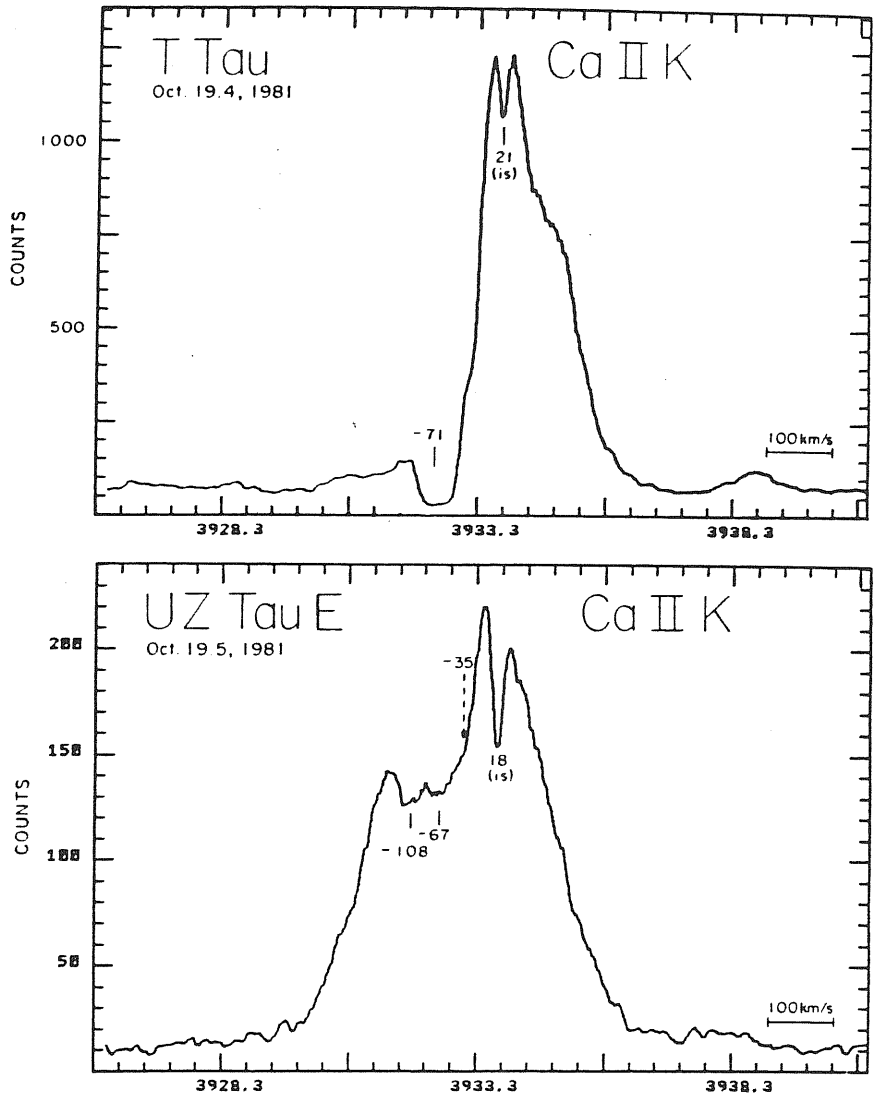

Fig. 1.2: Line profile of the CaII K line of the T Tau, UZ Tau E. The interstellar absorption is indicated by "is".

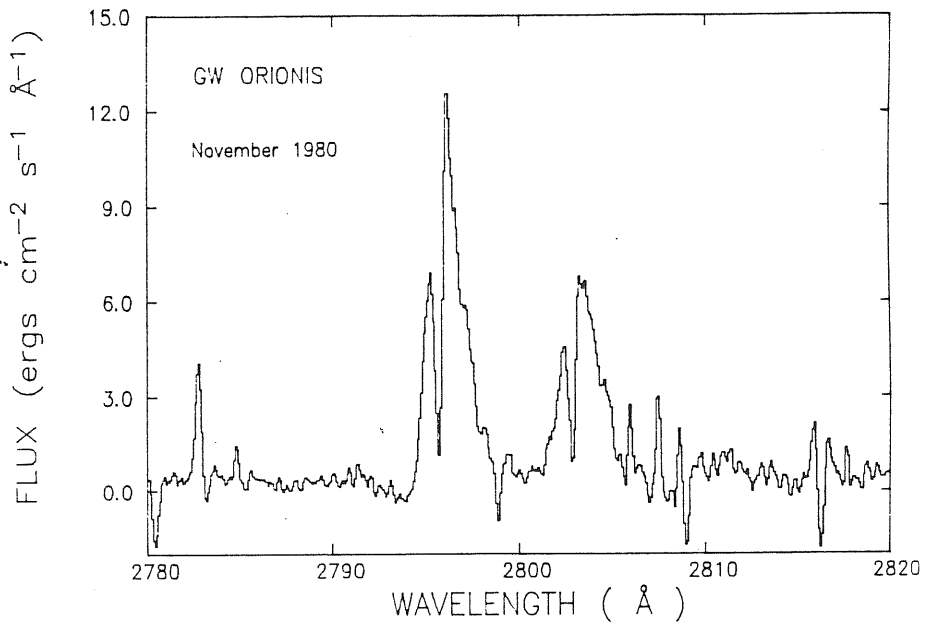

Fig. 1.3: MgII h and k line profiles for the T Tauri star GW Ori. Observed fluxes are given, in units of 10^{-13} $erg\ cm^{-2}\ s^{-1}\ \AA^{-1}$. The lines are broad, and each emission component is cut by a narrow absorption component. The other small, narrow spikes are noise (Catherine *et al.*, 1986).

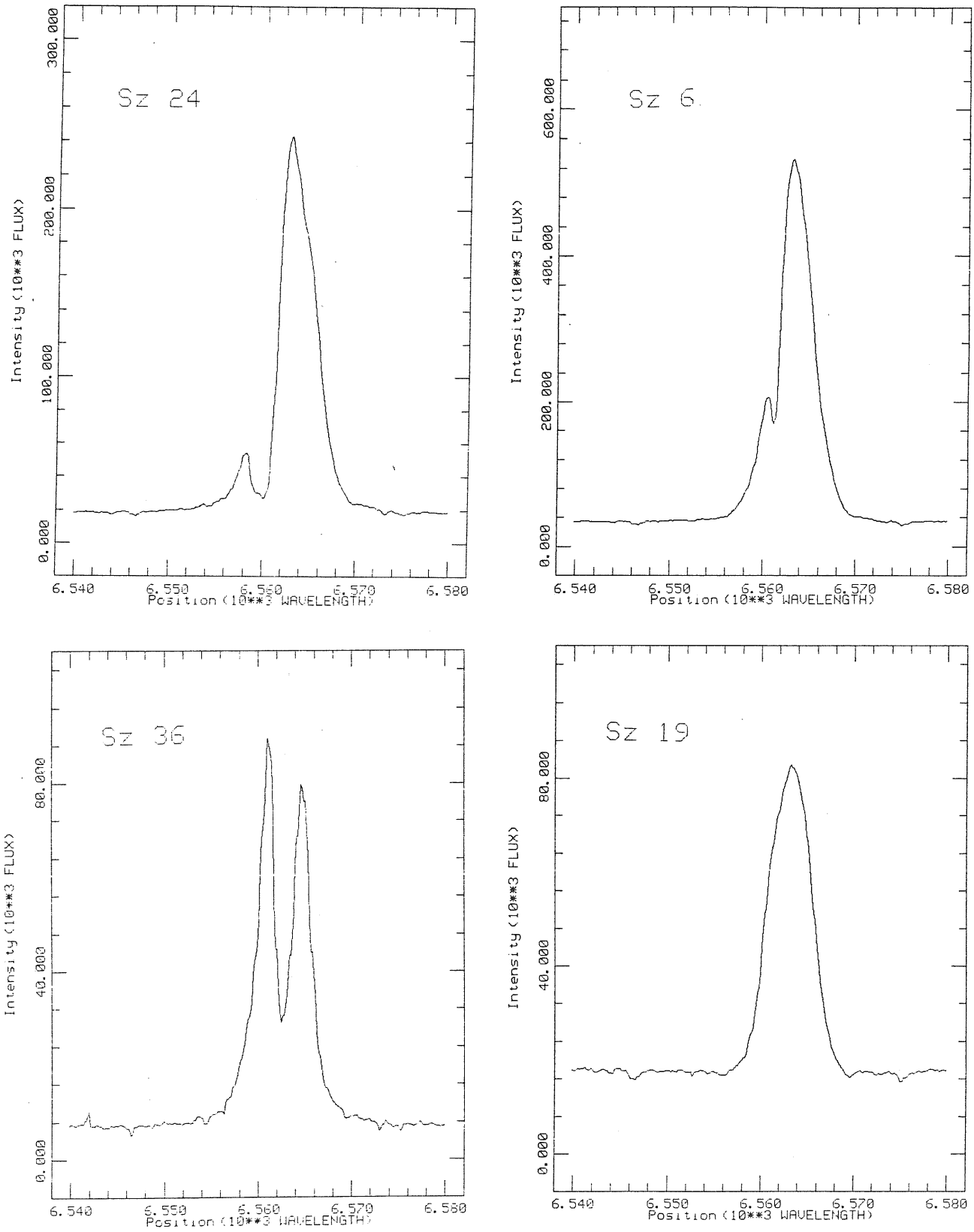

Fig. 1.4: H_α lines profiles of our sample.

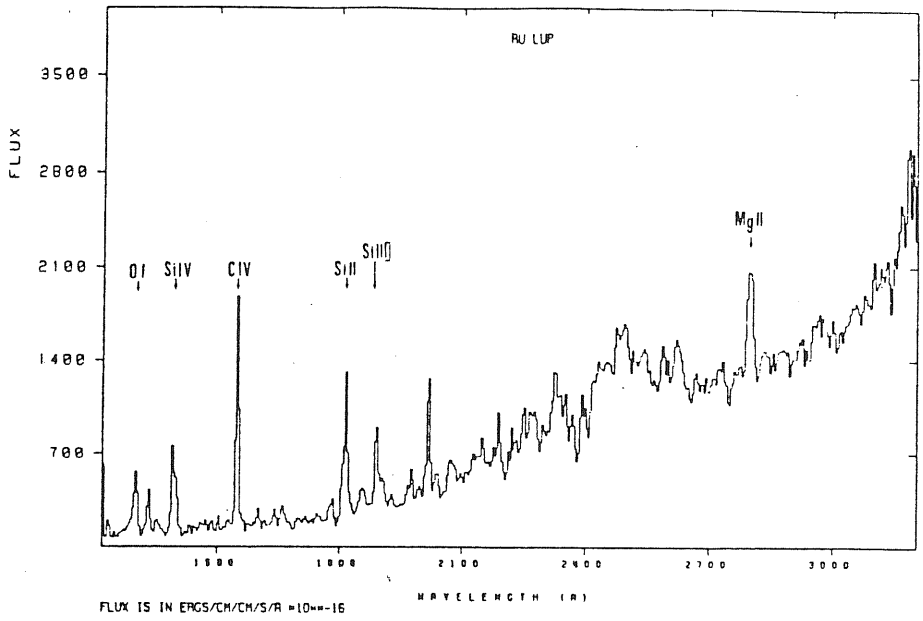

Fig. 1.5*a*: IUE low dispersion spectrum of the T Tauri star RU Lupi. The spectrum is a combination of short and long wavelength spectra (Catherine *et al.*, 1986).

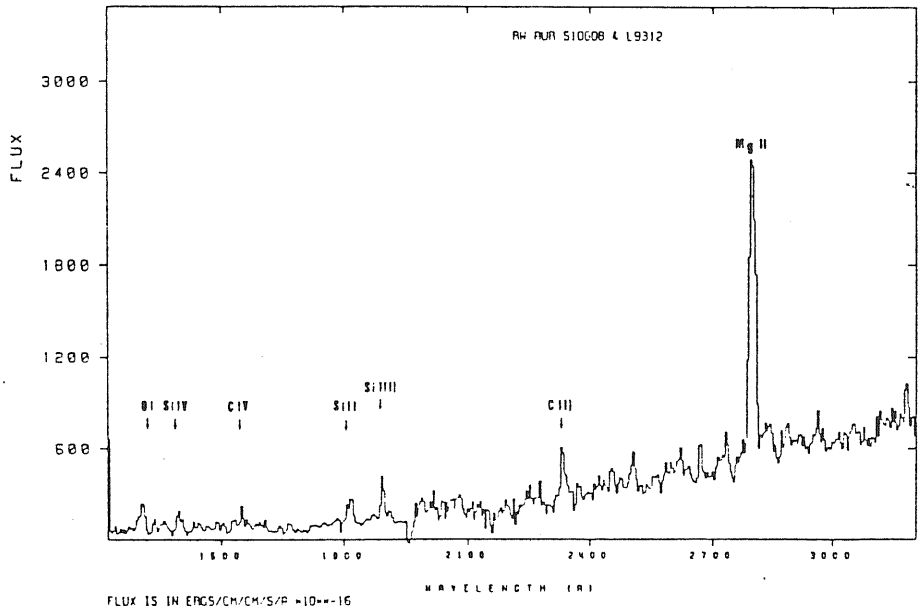

Fig. 1.5*b*: IUE low dispersion spectrum of the T Tauri star RW Aur. The spectrum is a combination of short and long wavelength spectra. The position of the main emission lines is given. Note the weakness of the emission features in RW Aur when compared with RU Lupi (Catherine *et al.*, 1986).

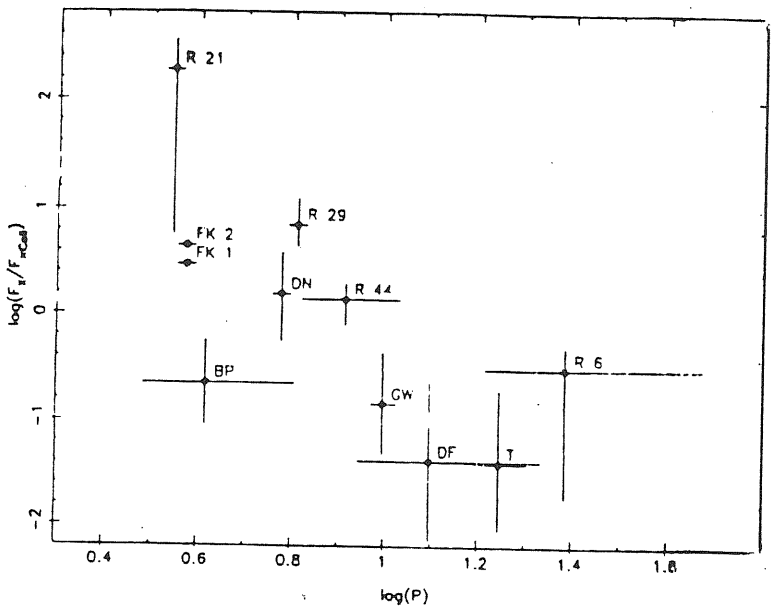

Fig. 1.6: Ratio of X–ray flux to CaII flux versus rotation period for T Tauri stars.

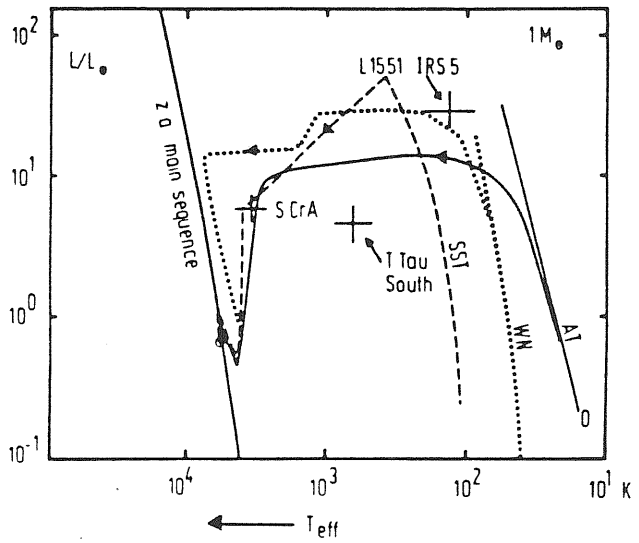

Fig. 1.7: Computed 1 $M_\odot$ evolutionary tracks in an H–R diagram. The tracks labeled SST, WN, and AT are taken from Stahler *et al.* (1980), Winkler *et al.* (1980), Appenzeller *et al.* (1975), respectively. (In the case of the SST track the section $4 \cdot 10^2 \leq t_{eff} \leq 3 \cdot 10^3$ K is assumed to be very short-lived and unosservable).

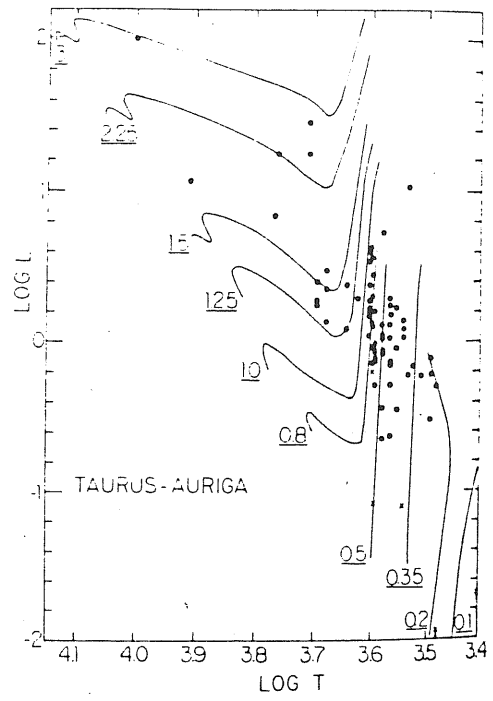

Fig. 1.8: The H–R diagram for stars in the Taurus–Auriga dark clouds. A series of convective–radiative evolutionary tracks are also shown. Filled circles, stars observed in the infrared region. Crosses, stars observed only in the optical region. Their true bolometric luminosities will exceed the values plotted (Cohen and Kuhi, 1979).

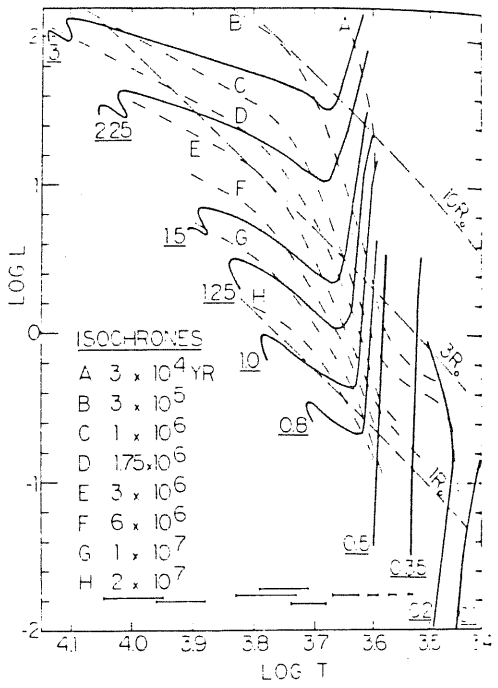

Fig. 1.9: Interpretive H–R diagram for Fig. 1.8. Shown are lines of constant radius, isochrones, convective–radiative tracks for stars of different mass, and error bars in $\log T$ for tipical stars of different spectral type (Cohen and Kuhi, 1979).

CHAPTER II

The T Tauri Phenomenon: The Veiling Problem

§2.1 *Observational Evidences of Veiling*

In section 1.2 we have seen which are the main spectroscopic caracteristics of the T Tauri stars. The absorption spectrum is characteristic of K–M main sequence stars and the emission spectrum is dominated by FeII emissions. Indeed, as seen in Fig. 1.1, it is perfectly possible for the emission lines to mask completely any absorption lines, at least at low to moderate spectral resolution. In some cases, even at high-dispersion we fail to get evidence of absorption features. There is a continuous range of spectra between pure absorption line spectrum and emission dominated spectrum. This is in essence the "*veiling*" problem for the T Tauri stars. As we have seen before it produces two effects:

a) *the blue veiling*, i.e. a stronger continuum in the blue part of the spectrum;

b) *differential veiling*, which makes the lines which are strongest in a dwarf star to fill in faster than the weak lines.

2.1.1 *Blue Veiling*

The veiling of T Tauri spectra was described by Joy as apparently due to an overlying continuous emission which fills in the photospheric absorption features in the blue ($\lambda < 5000\mathring{A}$) spectral region. Herbig (1962) discusses two components of this emission continuum: the component noted by Joy and a *strong ultraviolet* ($\lambda < 3800\mathring{A}$) *continuum* component. Kuhi (1970) shows (from scanner observations) that the ultraviolet continuum very likely arises from Balmer continuum emission and from the crowding of the Balmer emission lines near the series limit. Fig. 2.1*a,b* illustrate the spectral energy distribution (including the

emission lines) for several stars all classified as having the same spectral type. (Kuhi 1974). A standard G5 V star is included for comparison. The continuous energy distributions does indeed resemble that of a normal dwarf except for those stars having a strong emission line spectrum (e.g. RW Aur and DG Tau). A strong excess radiation is evident shortward of $\lambda \sim 4500\mathring{A}$ as well. The rich emission-line spectrum makes it very difficult to say exactly how much of the flux measured at a supposed continuum wavelength is really due to emission-lines. Despite the "blueness" of the emission continuum, there is no preferred wavelength which defines the onset of veiling. Rather, the perceptible veiling may, in some cases, be restricted to the blue. In the other cases it extends well beyond $5000\mathring{A}$. These data strongly suggest that the observed spectrum of a typical T Tauri star is the sum of a photospheric spectrum of a late type star and an emission continuum bluer than the photosphere. The contribution of the emission continuum relative to the photospheric continuum spans over a wide range of values.

The nature of the ultraviolet and blue continuous emission can be seen more clearly if we subtract the spectral energy distribution of a standard star from that of the T Tauri star of the same spectral type (Kuhi, 1974). With such a subtraction we make the assumption that the region producing the excess continuous emission is optically thin to the underlying photosperic radiation. If the emission is produced in a large envelope, this is very likely to be the case. However, if it is produced in a chromosphere, then it has, very likely, optical depth greater than one; thus the subtraction can only give an indication of the peculiarities of the T Tauri spectrum. Fig. 2.2 shows the results of the subtraction in four different spectral observations of DG Tau, a star with a considerable ultraviolet excess.

On the optically thin assumption, a temperature of the emitting region can be computed from the ratio of the flux differences at $\lambda 3320$ and $\lambda 3620$ between

the T Tauri and the standard star assuming that the emission is free–bound (level 2). Such temperatures are all in excess of $\sim 50000K$. Viceversa on the optically thick assumption, all the radiation comes from this region (i.e. none from the photosphere) and the temperature derived from the ratio of the flux at $\lambda 3320$ and $\lambda 3620$ typically ranges from 7750 to $8710K$. These values are clearly lower limits for the temperature of the emitting region, since the optical depth is probably not infinitely large.

The strength of the ultraviolet and blue veiling emission correlates positively with the emission line strength. Qualitative confirmation of the correlation between the ultraviolet continuum flux and H_α is provided by the spectrum scanner observations of Kuhi (1974). He uses the dereddered continuum fluxes $F_{\lambda 3620}$ and the H_α fluxes to illustrate this point (Fig. 2.3). The flux at $\lambda 3620$ will be predominantly the excess ultraviolet radiation for those stars with large emission and primarily the photospheric radiation for those stars with very little emission. A correlation between $F_{\lambda 3680}$ and $F(H_\alpha)$ exists, but there is a great deal of scatter. The same correlation between H_α strength and the blue veiling emission is demostrated also in Fig. 2.4 where Rydgren (1976) presents histograms illustrating the distribution of observed H_α equivalent widths for the T Tauri stars located in the Taurus and ϱ Oph clouds. The H_α equivalent widths are mean values computed from the spectrum scanner observations of Kuhi (1974). The atched regions in these histograms indicate the stars with strong blue veiling (no blue photosperic absorption features). It appears that spectral veiling just sufficient to hide the blue part of the photospheric spectrum corresponds to a particolare H_α equivalent width. These data strongly implies a close connection between the origin of H_α emission and the ultraviolet emission: Balmer free-bound emission is the obvious suggestion.

Many T Tauri stars show a discontinuous increase in their spectral energy distributions just shortward of the Balmer limit. This feature is apparent in

Kuhi's (1974) spectrum scanner observations and more dramatically in Rydgren *et al.* (1976) spectra. For those stars, it is certain that the ultraviolet emission arises from Balmer continuum radiation.

The evidence presented above indicate that the ultraviolet continuum results from Balmer continuum emission together with unresolved Balmer line emission near the series limit, and that the blue veiling is due to a related continuous emission process with a spectral distribution somewhat bluer than a late-type photosphere. It is extremely tempting to identify the *blue veiling* with Paschen continuum emission. The B-V color of optically thin Paschen continuum emission from a hot gas is on the order of 0.5 mag; this is fully compatible with the observed properties of the blue veiling. This leads Rydgren *et al.* (1976) to the following working hypotesis: *the veiling emission observed in T Tauri spectra is free-bound and free-free hydrogen continuous emission from a hot ionized envelope surrounding the star.*

2.1.2 *Differential Veiling*

We said that the photospheric absorption features of T Tauri stars are often much weaker (or "veiled") than in the standard stars with same spectral type. But as illustrated by Fig. 2.5, in the standard stars only the weak lines occur in absorption, while the strong lines appear affected by chromospheric emission (e.g. Cram 1979). The photospheric absorption spectra of the weak-emission T Tauri stars usually appear normal. In most cases the spectrum in the blue spectral range gives higher value of T_{eff} than the red spectrum. This effect is illustrated in Fig. 2.6 where Appenzeller (1985) compares two sections of the spectrum of the mild T Tauri or PTT star ROX 3 with the spectra of standard stars of known effective temperature. It is possible see that ROX 3, discovered by Montmerle *et al.* (1983) as an X-ray emitter, shows only very

little chromospheric emission. In fact, H_α is the only (weak) emission line. On the other hand, the great strength of the Li I resonance blend clearly proves the PMS character of ROX3.

As shown in Fig. 2.6 the strength of the ground-state lines of CaI and CrI relative to the G-band and the FeI lines and other criteria which are usually used in the blue spectral range indicate for ROX 3 a spectral type near K4 and definitively earlier than K9. On the other hand, the TiO bands in the red part of the spectrum are much stronger than in the K4 star and have a measured strength which is in close agreement with the corresponding values in MO standard. Hence even in this marginal T Tauri star the effective temperature values derived from blue and red classification spectra differ by as much as 660 K or 15%.

§2.2 *The Origine of the Veiling*

Whatever causes the "T Tauri phenomenon", its manifest effect upon the optical spectrum is to produce emission in spectral lines that, in normal stars of the same photospheric temperature, would be purely in absorption.

There has been, and still is, a good deal of controvery in the literature as to the nature of this masking of absorptions features; one asks if this is due solely to emission at specific line wavelengths or if it represent "veiling" by a genuine continuum.

The opinion is that the emissions described above are due to a possible contamination of continuum emission from the atmospheric layers overlying the photosphere (maybe a *chromosphere* or a *circumstellar envelope*).

Several authors (e.g. Appenzeller, 1983; Kuhi, 1983) discuss how the presence of this extra continuum could produce this "veiling" of the photospheric absorption spectrum by filling the lines and thus, making the star to appear hotter.

This opinion is confirmed from the continuum energy distribution of the T Tauri stars. Fig. 2.7 shows the observed continuum energy distribution of the star T Tau between 140 *nm* and 11 *cm*. As shown by Bertout (1980). This spectrum is readily explained by a superposition of three components:

a) radiation from a normal late type stellar photosphere;

b) free-free and free-bound emission from a thin ionized circumstellar envelope;

c) thermal radiation from circumstellar dust.

Although the well investigated "prototype" T Tau is probably a special case, where most of the dust radiation is produced by a cool companion, the presence of the three emission mechanisms seems to be a general property of the T Tauri stars, and in most cases a superposition of these three mechanisms results in a good fit of the observed energy distribution. However, some T Tauri stars with strong emission spectra show an excess in the blue spectral range, which cannot be explained by a superposition of a normal photosphere and the radiation of the ionized envelope (see e.g. Strom, Strom and Grasdalen 1975). Usually the same stars also show a strongly weakened or "veiled" photospheric absorption spectrum. Two mechanisms have been suggested to explain this phenomenon:

a) an additional absorption line free blue continuum light source, which dilutes the photospheric radiation;

b) the existence of "deep chromospheres" (section 2.2.1) i.e. an atmospheric temperature minimum occuring already at a density and optical depth much (i.e. $\sim$ 100 times) higher than in the Sun.

As additional light sources *viscous accretion disks* or *extended hot layers* heated by turbulence (Ulrich 1983) have been suggested. The *deep chromospere* model has been studied by Dumont *et al.* (1973) and Cram (1979). A temperature minimum at a high optical depth may be caused either by excessive mechanical or magnetohydrodynamic heating from below or by accretion shocks. One of the most important theoretical contribution to the problem of

the origin of the blue continuum and the veiling in T Tauri spectra are the synthetic spectra computed and reproduced by Cram (1979), which supports the deep chromosphere hypothesis.

None of the models proposed above can explain all the emission properties described in section 2.1 and we can anticipate that the observed energy distribution of the T Tauri stars could be explained by a combination of:

i) a late type photosphere,

ii) a "deep chromosphere" (in some cases possibly resulting from an accretion shock),

iii) a partly ionized and (again at least sometimes) dusty circumstellar envelope.,

iv) accretion disks.

Now let us see in more detail what observational evidences can be explained by the different proposed models.

2.2.1 *Photosphere and Chromosphere*

Part of the T Tauri phenomenon could be explained by a model involving a small emitting region lying close to the star where the temperature increases with the geometrical heigh i.e. a *chromosphere.*

Such a model was first proposed by Herbig (1970) who suggested that the T Tauri temperature minimum was located deeper in the atmosphere at $\tau_{5000} \sim 10^{-1}$ or 10^{-2} as compared to 10^{-3} for the Sun. Fig. 2.8 shows schematically the temperature profile for this model. Weak lines form deep in the atmosphere and appear in absorption, while strong lines form in the rising temperature zone and appear in emission.

If a star has a sufficiently dense chromosphere $\tau_\nu = 1$ for a *strong line* is reached already in the chromosphere, where the positive temperature gradient allows the formation of emission lines only. On the other hand for *weak lines*

the small line absorption coefficient may allow to look down into the deeper photospheric layers where the temperature gradient is normal. Hence in contrast to the standard star spectra, in the T Tauri stars an *increase* with temperature of a line absorption coefficent may result in a *weakening* or *disappearance* of the corresponding absorption line.

Fig. 2.6 can be explained on the basis of the assumption of a T Tauri star with dense chromosphere.

In more extreme T Tauri stars the strong CaI and CrI ground state lines tend to occur in emission. In the case of ROX 3 the lines appear in absorption, but they are probably contaminated by chromospheric emission. In addition, because of the high line absorption coefficient, these lines are probably formed relatively high in the photosphere near the temperature minimum, where the flat temperature gradient weakens the absorption strength. In the weaker FeI lines, where we look deeper into the photosphere, these effects are less pronounced. Hence, the chromospheric effects mimic a higher effective temperature.

Chromospheric TiO emission is very unlikely. But the high optical depth of the temperature minimum will certainly influence the molecular bands as well.

So, on the basis of chromospheric model, it is possible to explain several characteristics of the T Tauri stars. But for this model the H_α line is a problem in most stars; its strength typically requires a chromosphere with much greater mass column density than is implied by the other diagnostics. Its breadth is even less likely to come from a classical chromospheric temperature distribution; opacity broadening can be ruled out. Dumonit *et al.* (1973), Heidmann and Thomas (1980) used a very schematic deep chromosphere - type model to reproduce the ultraviolet continuum and the flux in H_α, with limited success.

Calvet, Basri and Kuhi (1984) also showed that as the chromosphere becomes sufficiently deep, the continuum picks up a contribution from it. This drives

the Balmer continuum into emission and yields a "blue veiling" contribution from the Paschen continuum at wavelengths short enough to provide sufficient contrast in the Plack function between photosphere and chromosphere. They have constructed semi-empirical homogeneous models for the photosphere and chromosphere of TTS by taking into account the observed fluxes in CaII , MgII k, H_α, the UV lines and the continuum energy distribution. The basic photospheric parameter used are $T_{eff} = 4000K$ and $\log g = 3.5$, which correspond to a typical T Tauri in the Taurus-Auriga cloud (Cohen e Kuhi 1979). In the costruction of these models, the position of the temperature minimum is adjusted to reproduce the observed width of the CaII k line. The transition region location, m_{tr}, is in agreement with densities determinated from ultraviolet line fluxes (Cram, Giampapa, and Imhoff 1980) and is adjusted to produce fluxes in CaII k and Mg II k comparable to observations.

The most important results from this study are the following:

1. the photospheric - chromospheric temperature profile of TTS, shown in Fig. 2.9, are characterized by a deep temperature minimum, in agreement with early estimates for the positions of this minimum (Herbig 1970, Dumont *et al.* 1973).
2. The chromospheric temperature profile is characterized by a plateau at $T \sim 6000K$, similar to that found for the Sun (Vernazza *et al.* 1981) but less broad and extending to deeper column density.
3. The continuum energy distribution of TTS is determinated by both the photosphere and the chromosphere. (Fig. 2.10). A late-type photosphere has its maximum continuum flux at $\lambda > 8000\AA$. Accordingly, the photospheric contribution of the flux dominates in the red region of the spectrum, unless the chromosphere has an extremely deep transition region. On the other hand, the photospheric flux in late-type stars falls sharply at$\lambda < 4560\AA$, because of the effect of line blanketing. For this reason, radiation from the

chromosphere becomes increasingly important as the wavelength decreases, creating an excess of flux over the normal photospheric level which could be identified with the "blue excess" observed in TTS. Because of the wavelength dependence of line blanketing, this excess is differential, increasing toward shorter wavelengths. Fig. 2.11 shows this effect.

At infrared wavelengths, longer than $\sim 3\mu$, radiation from the chromosphere is dominant again. However it cannot account for the IR excess observed in TTS (Mendoza 1966, 1968; Cohen and Schwartz 1976, Rydgren, Strom and Strom 1976, Rydgren and Vrba 1981). This excess must be due to thermal emission from a dust distribution around the star (Cohen and Kuhi 1979; Rydgren and Vrba 1981), as confirmed by a correlation existing between the IR excess and degree of polarization (Bastien 1982), and the indication that the polarization arises from a dust distribution located outside the main emission-line region (Bastien and Handstreed 1979).

4. The energy output from the chromosphere is determinated mainly by the location of the beginning of the transition region. Moreover, changes in m_{tr} determine changes in the ultraviolet continuum flux which may account for the observed short-term variability.
5. Neither the large observed H_α fluxes neither the steep Balmer decrement observed in TTS can be obtained by the chromosphere, except in the case of the less active stars.
6. One would ask the origin of the energy needed to produce such a chromosphere. The values implied become appreciable fractions of the stellar luminosity when the continuum is changed substantially. The effects on the line spectrum are always more dramatic than in the continuum because the lines are optically thicker, so one would not expect large continuum excesses to be associated with anything like a normal photospheric spectrum. Thus, although the chromospheric model could explain even the extreme T Tauri

stars in principle, in practice there are serious objections to this. In the strong emission lines other than H_α, one must be careful in ascribing it to chromospheric origin. Most of the modelling work has dealt with prediction of the integrated line flux, and this can be done successfully for many of the observed CaII and MgII line fluxes, for example. On the other hand, a chromosphere which lies near the stellar surface would be expected to produce a relatively narrow and symmetric line profile. The surface velocity fields could be tens of km/s, but are unlikely to be hundreds of km/s. Thus, a crucial part of identifying where a line is coming from is to obtain a resolved line profile. This has been done for a number of stars at MgII, H_β, and NaI D, for fewer stars at CaII, and for a big number of stars at H_α. The MgII profiles tend to be fairly similar to H_α, while the CaII profiles look chromospheric in the less active T Tauri stars and more like H_α in the more active stars. In looking at lines of different optical depths (e.g. the k line and the IR triplet of CaII) one can see the broad component increasing in the thicker lines.

An example of these effects is given in Fig. 2.12 for the classical T Tauri star BP Tau with observations obtained with the Hamilton spectrometer at the Lick Observatory. It appears reasonable to suppose that most T Tauri stars have a chromospheric emission component in their strong lines, but that this component can be overwhelmed by an envelope contribution in the more active stars. This means that analyses of line fluxes should really be completed with high resolution work, in order to distinguish where the different components of the line profiles are produced.

2.2.2 *The Envelope*

The strong emission lines which cannot be explained by chromospheric emission because of their strength, breadth, and shapes presumably arise from a region of formation outside the stellar surface. Such region is generally called

"envelope". Even if several spectroscopic and photometric (optical and infrared) observations of T Tauri stars (e.g. Rydgren 1976) have allowed to understand several envelope properties it remains one of the mysteries of the T Tauri stars.

What is fairly clear is that mass loss produces part of the envelope profile; in fact there is often either a narrow or broad blueshifted absorption component superposed on the broad emission. It is almost certainly a mistake to think that a single paradigm will fully explain the profile observed. Among the possible regions which may contribute to there are:

1. a turbulent boundary layer (see section 2.2.3);
2. a spherical or bipolar outflow or wind;
3. an extended "chromosphere" or heated region (section 2.2.1);
4. cooler shells or patches of circumstellar matter due either to remnant inflow or piled out outflow;
5. extended structures in the stellar atmospheres such as magnetic loops.

To explain the observation a variety of models involving an hot extended envelope with some kind of "ad hoc" velocities have been calculated. This envelope is taken to be:

- *in expansion*, to reproduce the emission line profile (Kuhi, 1964; Kuan, 1975);
- *static*, to reproduce the general emission characteristics (Rydgren, Strom, and Strom, 1976);
- *infalling*, to reproduce observations indicating infall (Ulrich, 1976; Appenzeller, and Wolf, 1977; Wolf, Appenzeller, and Bertout, 1977; Mundt, 1979). No detailed spectrum calculation has been done yet. An appealing feature of this type of model is that it can account in a natural way for the source of energy for the emission with the kinetic energy of the infalling material.

We can try to characterize the envelope properties taking H_α as the canonical envelope diagnostic.

It is clear from variety of profiles observed that there is not a single phenomenon responsible. Most of the lines have widths of a few hundred km/s. If it is due to Doppler motions, they might involve orbital motions, turbulence, outflow, inflow or some combination of these. It is interesting that the line tipically extends as far as to the red as to the blue although it is usually asymmetric. When one wings is more extended it is usually the blue wing.

Forbidden line emission, which must arise over a region of tens or hundreds of AU in size, is seen in a significant fraction of the stars (Cohen and Kuhi 1979), but almost never in the redshifted wing. The lack of receding emission and the predominance of negative radial velocities has been interpreted as due to the presence of an absorbing screen or disk (Appenzeller *et al.* 1984) (Fig. 2.13*a,b*). Since the red wing is seen in H_α, one must either suppose that the disk does not extend all the way to the star (within a few stellar radii), or that the red emission comes from both sides of the equatorial plane. The former possibility is difficult when, as discussed in next section, we see the boundary layer emission from the star-disk interface. The latter possibility implies that H_α does not arise purely from a simple expanding geometry, either spherical or bipolar.

One alternative is that the H_α line is broadened by turbulence. This would have to be highly supersonic, and so it is not likely to be microscopic in nature. One possibility is that it is due to the wave motions that drive the wind, as proposed by Hartmann, Edwards, and Evrett (1982). They were able to reproduce many of the properties of observed profiles with this model. A variety of other models have been reviewed by Bertout (1984). Another possibility is that the turbulence is due to the violent motions of the gas, near an accretion boundary layer (a region where the disk meets the star). If so, however, one should expect somewhat different profiles from stars which are no longer actively accreting.

Observational tests of accretion (though it has been suggested for many years as a possibility) are necessary to conferm the accretion hypothesis; we cannot yet

say whether H_α shows convincing evidence for boundary layer emission. Even if accretion itself is not occuring, the orbital velocities in the disk near the star are still a few hundred km/s, leaving the possibility of generating broad profiles.

Apart from theoretical analyses of the line formation, there are often more direct reasons for thinking that H_α arises somewhere within a few stellar radii of the surface. The line can be quite variable, with sometimes dramatic changes in the whole profiles (including the far wings). These can occur as rapidly as within a few hours, or an timescales ranging from a day or a few days, to weeks, months or years. Some examples of the changes observed can be found in Mundt and Giampapa (1982), Hartmann (1982), or Basri (1987). The most rapid changes must be occurring near the star, perhaps in discrete structures (magnetic ?).

The only way to finally distingue all the possible effects will be through repeated high resolution coverage of a number of diagnostic lines together. This has became possible width the advent of échelle CCD spectrometers. With these, we may be finally able to resolve ambiguities about the geometry and location of the emitting and absorbing regions that go into making up the envelope profiles seen in the T Tauri stars, and derive the physical properties of the various envelope components.

2.2.3 *Disks*

One of the most exciting developments of the last few years in T Tauri research has been the increasing evidence that many of these stars are *surrounded by equatorial disks of gas and dust* probably a remnant of the original cloud. For a few stars there is direct imaging information from the infrared (e.g. Beckwith *et al.* 1984) suggesting an anisotropic continuum distribution. There has also been a series of observations which fairly directly observe the effects of a disk in the spectrum of FU Ori stars. For these stars, the disk is so active that it influence

the stellar temperatures, completely masking the light of the underlying star and changing the apparent spectral type. More commonly, the disks are too cool to display stellar absorption lines in their spectra. They are typically not very massive ($\ll 1M_{\odot}$) but they can still be major contributors to the infrared continuum. It is now thought that the infrared excess observed in most T Tauri stars is primarily due to a disk. Adams *et al.* (1987) assume that all of the (intrinsinc) luminosity of the outburst source FU Orionis comes from a star with surface temperature $T_{\star} = 7000\ K$. They find that a stellar luminosity $400L_{\odot}$ with $A_v = 2.4$ is required in order to reproduce the spectrum; the result is shown as the solid curve in Fig. 2.14*a*. Inclusion of the emission from a circumstellar dust shell yields a somewhat better fit to the observed data, the dashed curve in Fig. 2.14*a*.

The spectrum of FU Orionis can also be explained if Adams *et al.* (1987) make the assumption that *all* of the luminosity of this source arises from a Keplerian disk, presumably through some accretion process involving a disk. In this picture, the star radiates due to the heating by the disk. If they assume an intrinsic disk luminosity $L_D = 400L_{\odot}$ (where the intrinsic stellar luminosity $L_{\star}$ has been set equal to zero for semplicity) and $A_v = 2.4\ mag$, they obtain an almost identical fit so the observed spectrum, as shown by the radial curve in Fig. 2.14*b*. Also shown (dashed curve) is a theoretical model including emission from a circumstellar dust envelope using the same parameters as in the stellar outburst model.

Another good piece of evidence of disks in some systems is a comparison of the bolometric luminosity of the system compared with the bolometric luminosity of the star. This comparison can best be made when the underlying T Tauri star shows an unveiled spectrum in the optical. In section 2.2.1 evidence that the deep photospheres of these stars are normal was presented.

If a normal photospheric spectrum is seen, then by comparison with other

stars with similar photospheres but no signs of circumstellar material the stellar bolometric luminosity can be found. One difficulty is to properly determine the extinction in the presence of possible continuum excesses. One technique is to compare the spectral slope only in the part of the spectrum where there is no veiling. The extinction which forces this to match the standard spectrum is adopted. Ideally one should use a high resolution spectrum to properly measure the veiling at each wavelength and remove it first before maching the continuous. This has only recently become practical and will be tried in the near feature. For some stars it is difficult to do this well enough that a well determined value for the extinction can be found. Another problem not fully solved is whether standard extinction curves can be used for the T Tauri stars. The indications are that this is largely true in the optical, but the UV extinction (especially below 2300$\mathring{A}$) is more debatable (Herbig and Goodrich, 1986).

Once one has the intrinsic stellar continuum, extrapolated outside of the optical by use of standards, the bolometric luminosity is determinated. The actual observed bolometric luminosity (including especially the far infrared) will be equal to or greater than the purely stellar value. If it is greater than $L_{\star}$, this may be evidence for an anisotropic distribution of dust. A disk captures stellar light that would not normally go towards the observer, reprocesses it to the infrared, and send it to the observer. One can show that for a flat disk seen pole-one will obtain a bolometric luminosity of $1.25L_{\star}$. If the disk is not flat, but flares up on the outside, this can be as high as $1.5L_{\star}$. Thus a careful determination of the intrinsic stellar luminosity is very valuable for detecting the presence of a disk. So we must be careful when we speak of "stellar luminosity". Its meaning in fact is a bit subtle. One point is the treatment of extinction. If the extinction occurs near the star, it will heat the dust up and the radiation removed from the line of sight will be returned to it in the infrared. One potentially counts this energy twice if the optical light is fully dereddened and all infrared

light is also counted. If the extinction occurs sufficiently far from the star then this is not a problem. Another problem is that one does not actually observe a luminosity - one *measures* a flux and *deduces or infers* a luminosity, usually under the assumption that one is looking at a full hemisphere of a star and that the other hemisphere looks the same. In the presence of a large disk, the full stellar hemisphere can only be seen from the pole. Only half a hemisphere can be seen from near the equator.

By "stellar luminosity"one usually means the inferred luminosity from the observed flux with the assumption of no occultation. But, to complicate matters further, an observed flux may contain direct starlight and also contain light reprocessed through the disk which normally would not have been included in the observed flux (and therefore in the inferred luminosity) because it was not headed in the observer's direction. A large flat disk intercepts 24% of the starlight *over the whole sky seen from the star*, but this is not relevant for the conversion of an observed flux to an inferred luminosity. Such a conversion cannot properly be done (except in a statistical sense) without knowledge of the inclination angle of the disk. Thus when Basri (1987) refers to "stellar luminosity" he means the luminosity that is inferred from starlight without the presence of the disk. Looking at a passive disk system pole on and comparing that with the observed bolometric luminosity (which includes both direct starlight and reprocessed radiation) will cause one to decide $L_{bol} = 1.25 L_{\star}$ (presuming that disk light and starlight are separable and being sure to correct the inferred disk contribution for the unseen side). At other angles, the amount of starlight observed will be less because of occultation by the disk, and the amount of disk light observed will also be less (if the disk is optically thick) because the disk is seen increasingly edge on.

Above it has been assumed that the disk only acts as a "passive" reprocesser of stellar light. But it is evident that, if accretion is continuing through the disk

then additional light will be added from the release of gravitational potential energy. Lynden - Bell and Pringle (1974) worked out the general properties of a simple accretion disk which can be applied to the T Tauri stars. It turns out that the spectrum from such a disk has almost the same shape as from a flat reprocessing disk. This means that in the infrared one does not know whether active accretion is occurring unless the bolometric luminosity is greater than the limits above. For a number of observed systems among the classical T Tauri stars these limits are exceeded, so that is already excellent evidence for continuing accretion. Fortunately there is a good way to cheek on this and also detect accretion in lower luminosity system. This involves the boundary layer where the matter from the disk finally encounters the star. The luminosity of accretion in the disk is only half the available energy; if the material (assumed to be in Keplerian orbits) encounters a slowly rotating star the other half of the energy available will be released in bringing it to a stop. Bertout, Basri and Bouvier (1988) suggested that the UV excess observed for many stars may be due to this release.

If one makes a simple model for the boundary layer, one finds that an optically thick region with emitting area of $\approx 2\%$ the stellar surface will radiate with (backbody) temperatures in the 8-10 thousand degree range. Depending on the accretion luminosity it will veil the starlight into the blue part of the spectrum. Because as much luminosity comes out in the UV as from the infrared disk (which can be comparable to the stellar luminosity), one expect a major impact on the spectrum. Indeed the infrared spectrum of T Tauri systems a few microns is entirely from the disk in this model. The reason why the UV continuum appears to drop steeply is that extinction has a rapidly increasing effect toward shorter wavelengths; one has to ask how the star would have appeared with the some extinction but without the UV light from the boundary layer.

The first major study of T Tauri boudary layers using IUE observations has

just been made by Bertout, Basri and Bouvier (1988). The study of continuum excesses in different parts of the spectrum is complicated for the T Tauri stars by the problem of variability. If one wants to compare the UV flux to the optical flux, and each varies by several tenths of a magnitude or more then observations from same epoch should be used. This is particularly important if one wants to mach the observations to a single self-consistent model. Some progress can be made by knowing the range within which each part of the spectrum varies. These authors use simultaneous optical and UV spectrophotometry along with optical and infrared photometric variability studies to deduce the properties of disks and boundary layers in the context of the simple model. They pay particular attention to the question of to what extent the active chromospheres on these stars can account for the UV excess (see section 2.2.1). They conclude that there is a good evidence on a number of "ordinary" T Tauri stars where active accretion is present. The accretion rates are at order $10^{-7} M_{\odot} yr^{-1}$. In BP Tau, since one can see the chromospheric component of CaII K, it would be difficult to argue that the very strong UV excess observed come solely from the chromosphere which produces that not particularly strong line (though the low broad wings of the K-line might indeed be associated somehow with the boundary layer). Thus Basri (1987) believes there is good evidence for both active and passive disks among the T Tauri stars, and that is a major motivation for the classification in Tables 1.1 and 1.2.

Many of the details of how a boundary layer should actually look in both the continuum and in emission lines are not yet known.

Several problems have still to be solved:

1. will the emission come from an optically thick or thin region or some of each?
2. will all the energy be released as radiation, or is some of it converted to mechanical energy?
3. what is the real size of the boundary layer?

4. what effect will the stellar magnetic fields have on the disk as it approaches the star (the Alfvén radius is at a few $R_\star$)?

Anyway, the idea, which is coming out is that the layer is probably secure, because one has a big quantity of UV energy to explain in any case for some stars. The blackbody model for the emission is much more dubious, indeed the observations show that excess luminosity often appears as Balmer line and continuum emission which indicates that it cannot be the whole story. Presumably material is decelerated in shocks at high temperatures. Depending on the optical depth to the surface of the boundary layer this radiation will be partially thermalized to lower temperatures, and then the temperature structure of the boundary layer where it is becoming optically thin will further determine the emergent spectrum. The stellar magnetic fields would interact with the disk. It is also of interest to work out in more detail whether the effect of the disk on the underlying stellar atmosphere has interesting observable consequences. Could it, for example, be partially responsible for the appearence of very deep chromospheres in some stars?

The general picture presented in this chapter shows many problems of the T Tauri phenomenon that have been solved but shows that much work still is to be done before these peculiar stars are fully understood.

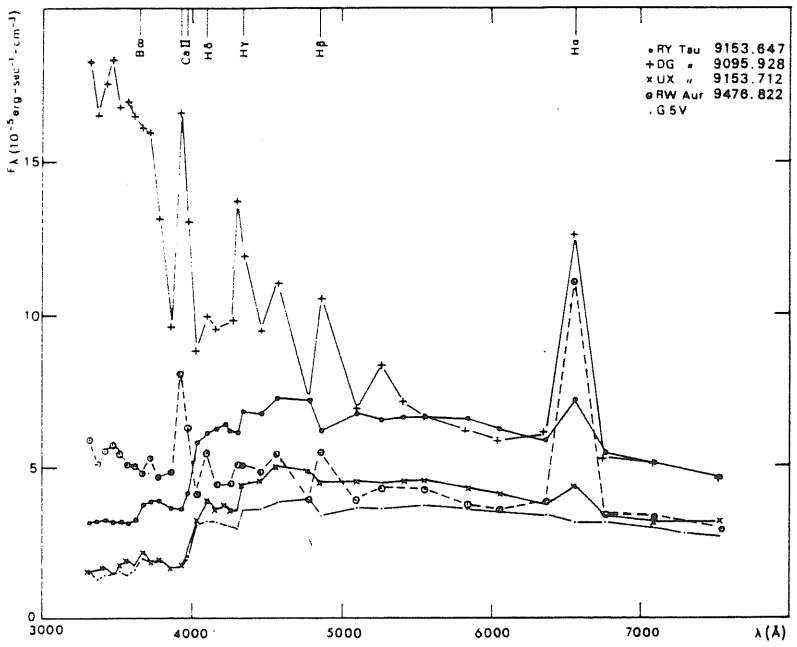

Fig. 2.1*a*: The spectral energy distributions from λ3320 to λ7530 of T Tauri stars all classified as dG5. The lowest curve is that of a standard G5 V star on an arbitral scale (Kuhi, 1974).

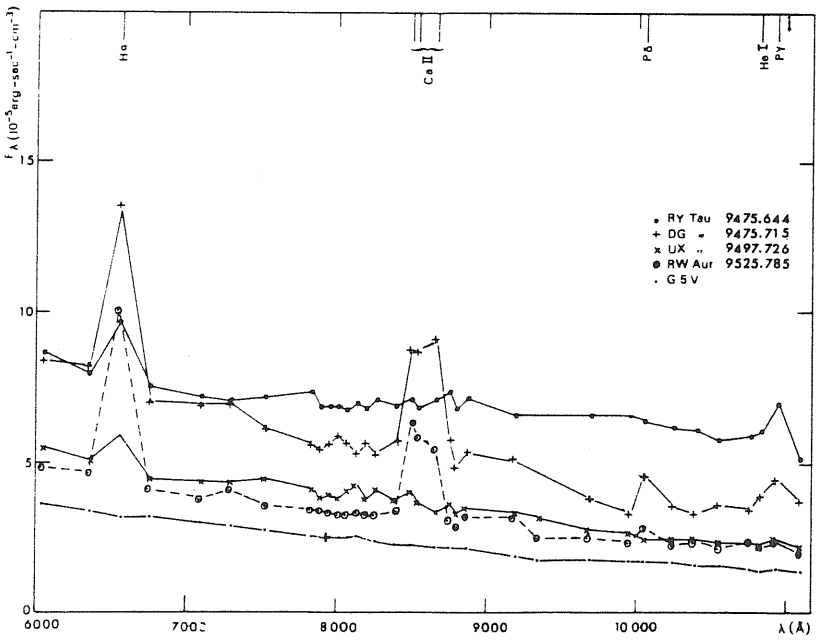

Fig. 2.1*b*: The spectral energy distributions from λ6056 to λ11100 (corrected for reddening) of the same T Tauri stars shown in Fig. 2.1*a*.

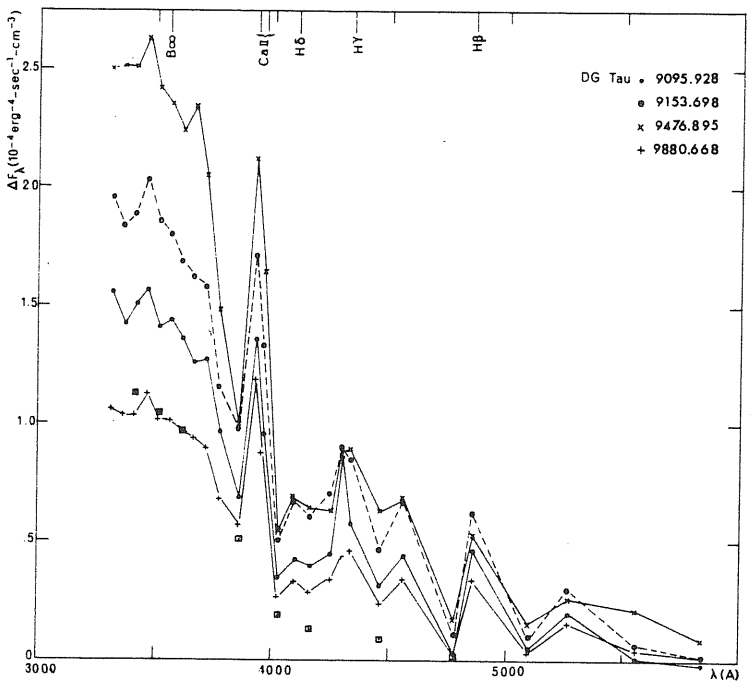

Fig. 2.2: The difference $\Delta F_\lambda (= F_\lambda(\star) - F_\lambda(std))$ between the continuous energy distribution of DG Tau at different dates and that of a G5 V star normalized to zero at λ6362. The squared symbols indicate the fluxes for 9880.668 corrected approximately for the effects of emission and absorption lines. Continuous emission is seen to persist to $\sim \lambda$4785.

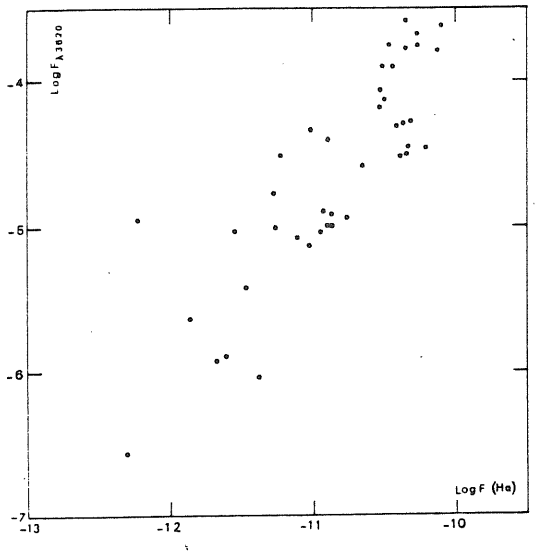

Fig. 2.3: The flux at $\lambda 3620 (F_\lambda$ in $erg\ sec^{-1}\ cm^{-3})$ vs the emission flux in $H_\alpha (F(H_\alpha)$ in $erg\ sec^{-1}\ cm^{-2})$. Individual observations for all the stars in Taurus Auriga are plotted.

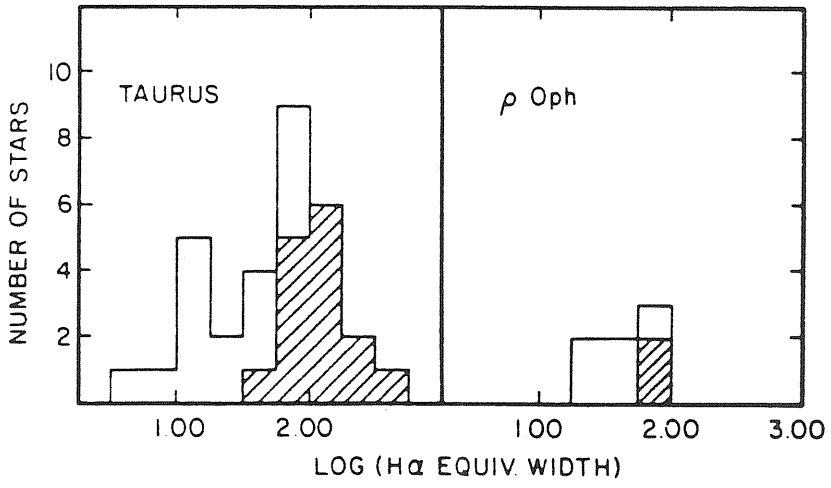

Fig. 2.4: Histograms showing the number of T Tauri stars in the Taurus and ϱ Oph dark clouds as a function of H_α equivalent width; stars with strong blue veiling are indicated by hatching.

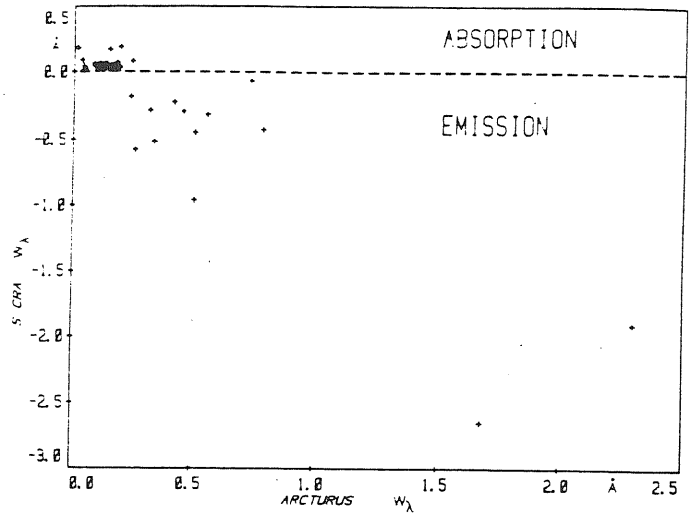

Fig. 2.5: Comparison of equivalent width values W_λ of atomic lines in the spectra of the K2 giant Arcturus and the T Tauri star S CrA. $W_\lambda < 0$ denotes emission lines. Note that in the T Tauri star only the (in the standard star spectrum) very weak photospheric lines are observed in absorption. The stronger lines occur in emission. (Appenzeller, 1985).

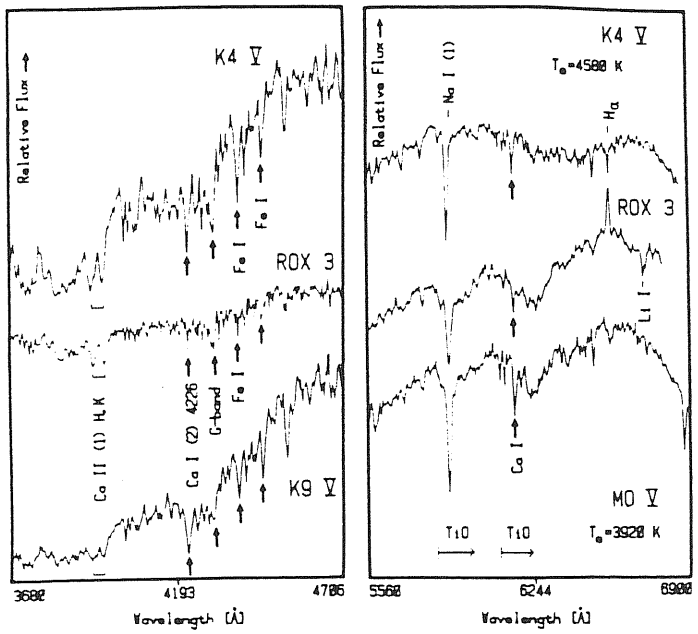

Fig. 2.6 Comparison of a blue and a red spectrogram of the "mild" T Tauri or PPT star ROX 3 with standard spectra. All spectrograms were obtained by J. Bouvier using the Image Dissector Scanner at the Cassegrain spectrograph of the ESO 1.5 *m* telescope. Note that the blue spectrum of ROX 3 resemples that of a K4 standard, while the red spectrum agrees closely with that of an M0 standard.

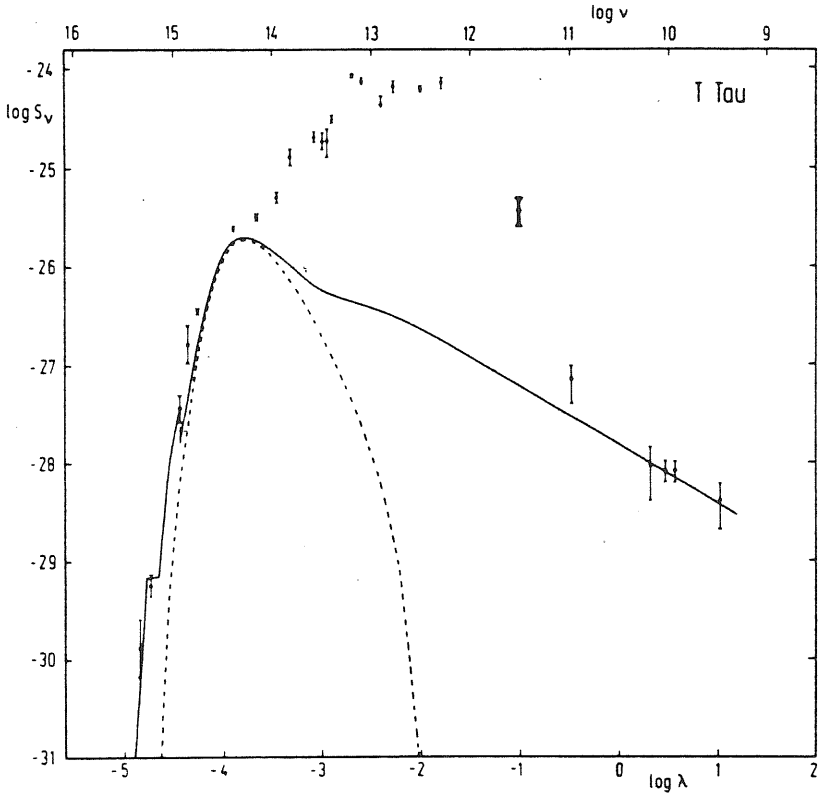

Fig. 2.7: Continuum energy distribution of the star T Tau (according to Bertout, 1980). The units of S_ν are in $W\ m^{-2}\ Hz_{-1}$, λ is given in cm, ν in Hz. The broken line indicates the contribution of the star's photosphere, the solid line the combined contribution of the photosphere and the ionized part of the circumstellar envelope. The remaining IR excess is attributed to dust emission.

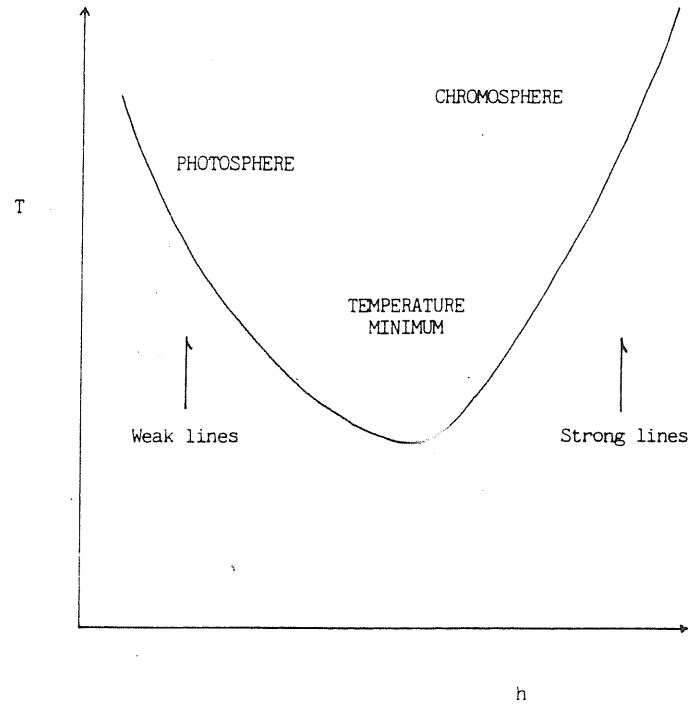

Fig. 2.8: Schematic temperature profile showing temperature rise above the photosphere corresponding to the chromosphere. Arrows show regions where weak and strong lines form.

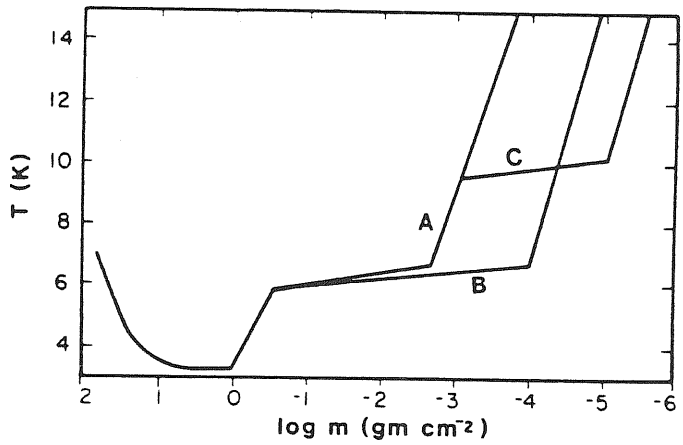

Fig. 2.9: The distribution of temperature vs. mass column density is shown for the three different chromospheric models (Calvet, Basri, and Kuhi, 1984).

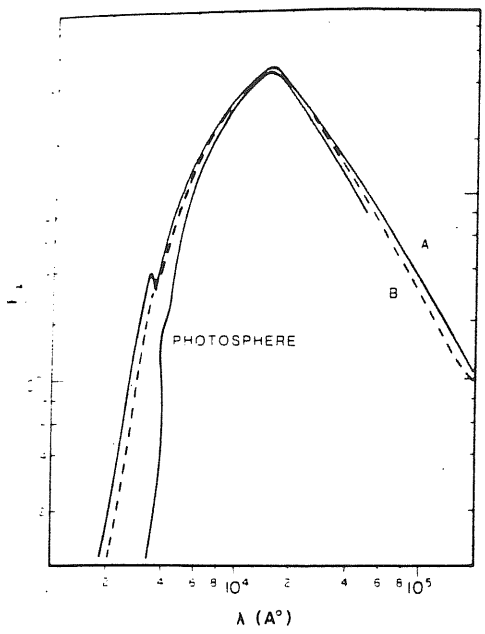

Fig. 2.10: The continuum surface fluxes calculated for models A and B of Fig. 2.9 are shown along with radiative equilibrium photosphere adopted from Carbon and Gingerich (1969). Note that the presence of a chromosphere shows up largely as an ultraviolet excess. The units for all fluxes and source functions in the figures are $ergs\ cm^{-2}\ s^{-1}\ Hz^{-1}$.

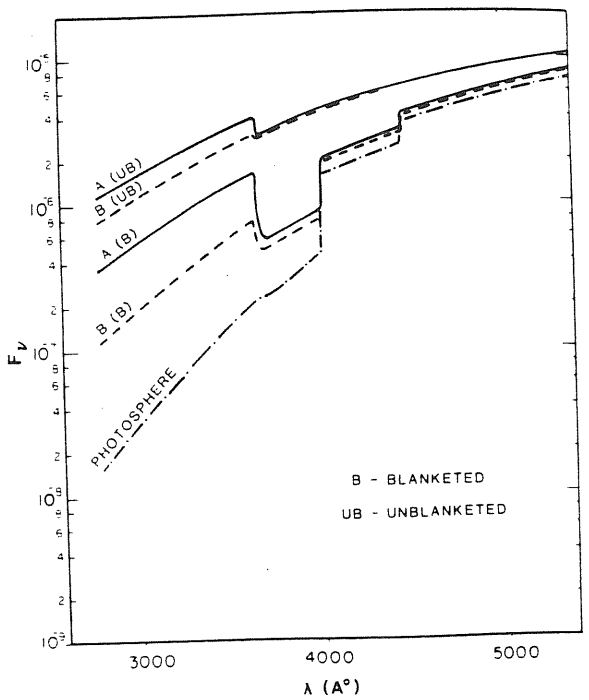

Fig. 2.11: Calculated continuum surface fluxes for several cases showing both the contributions of the chromosphere and line blanketing to the observed continuum. The lowest curve is just the blanketed photosphere which Calvet *et al.* (1984) adopte from Carbon and Gingerich (1969).The jumps longward of the Balmer continuum are due to their approximate treatment of line blanketing. Addition of the chromospheric contribution from models A and B to this curve leads to the middle curves, while adding those to the unblanketed photospheric continuum (not shown) leads to the upper curves.

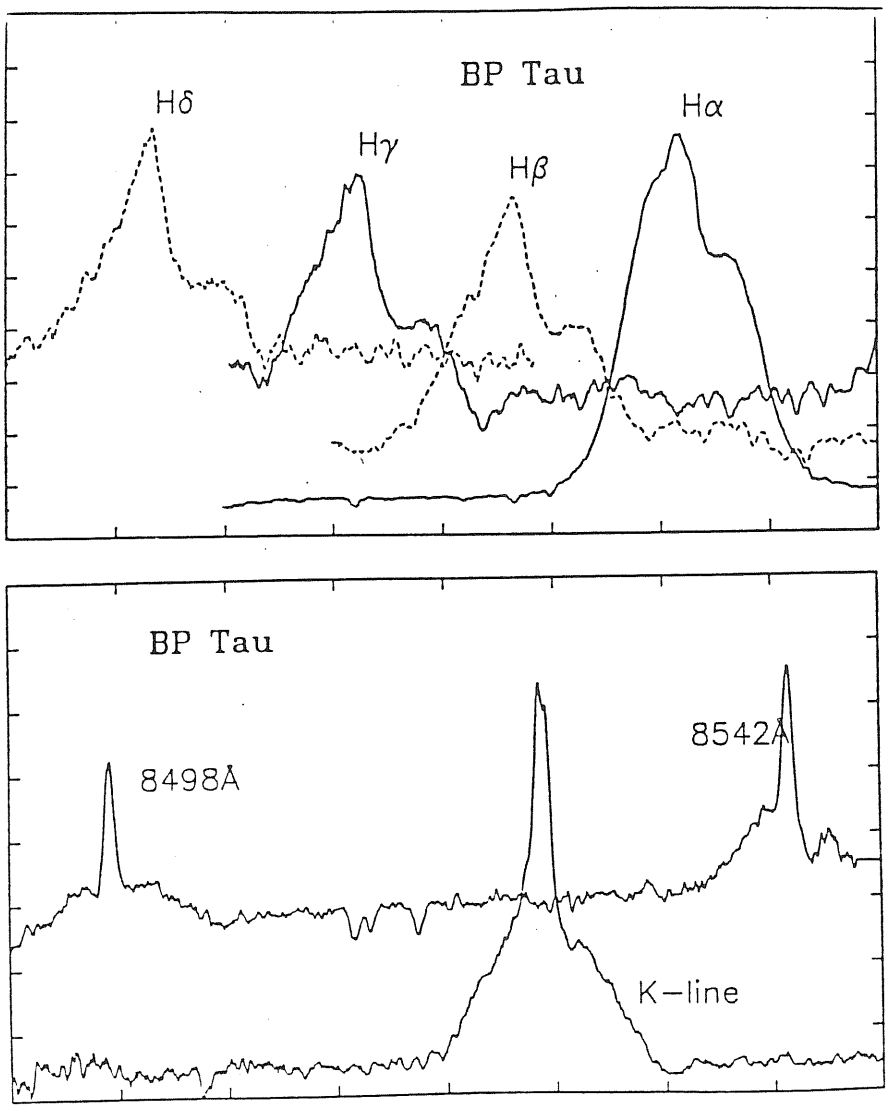

Fig. 2.12: Emission lines in the classical T Tauri star BP Tau. Lines from HI (upper panel) and CaII (lower panel). The spectra have been shifted and normalized arbitrarly, but the relative velocity scale is the same for each line. Observations were obtained with the Hamilton CCD échelle spectrograph at Lick Observatory. The two échelle frames contain almost the entire spectrum from $3850\mathring{A} - 8700\mathring{A}$ (Basri,1987).

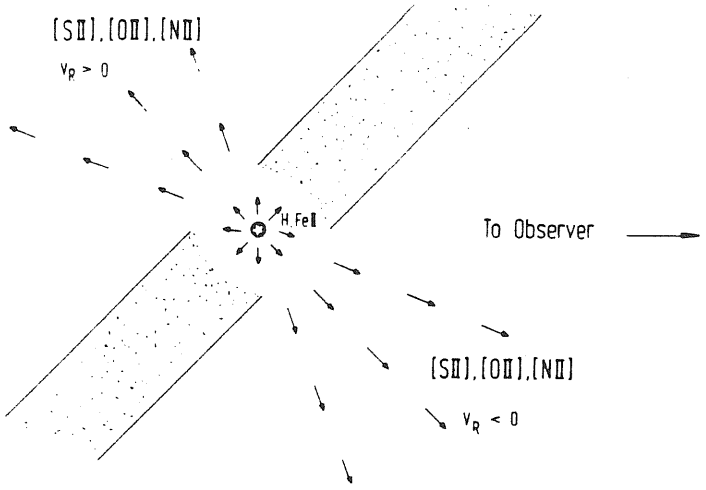

Fig. 2.13*a*: Schematic representation of the geometric obscuration scenario used to explain the predominantly negative radial velocities of the forbidden lines in T Tauri spectra.

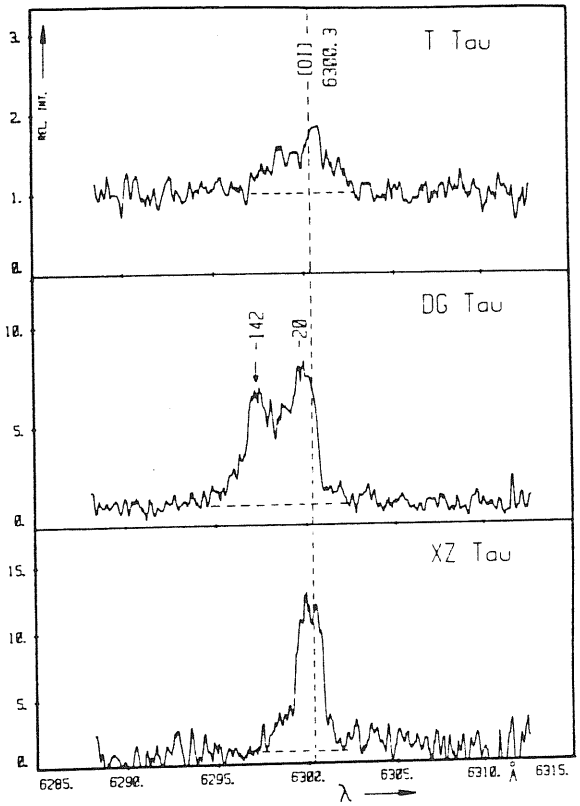

Fig. 2.13*b*: The [OI] λ6300 line profiles. The vertical broken lines indicates the rest wavelength of the line and the numbers give the radial velocities in km/s of the lines features marked by arrows. The predominance of negative radial velocities has been interpreted as due to a presence of an absorbing screen or disk (Fig. 2.13*a*).

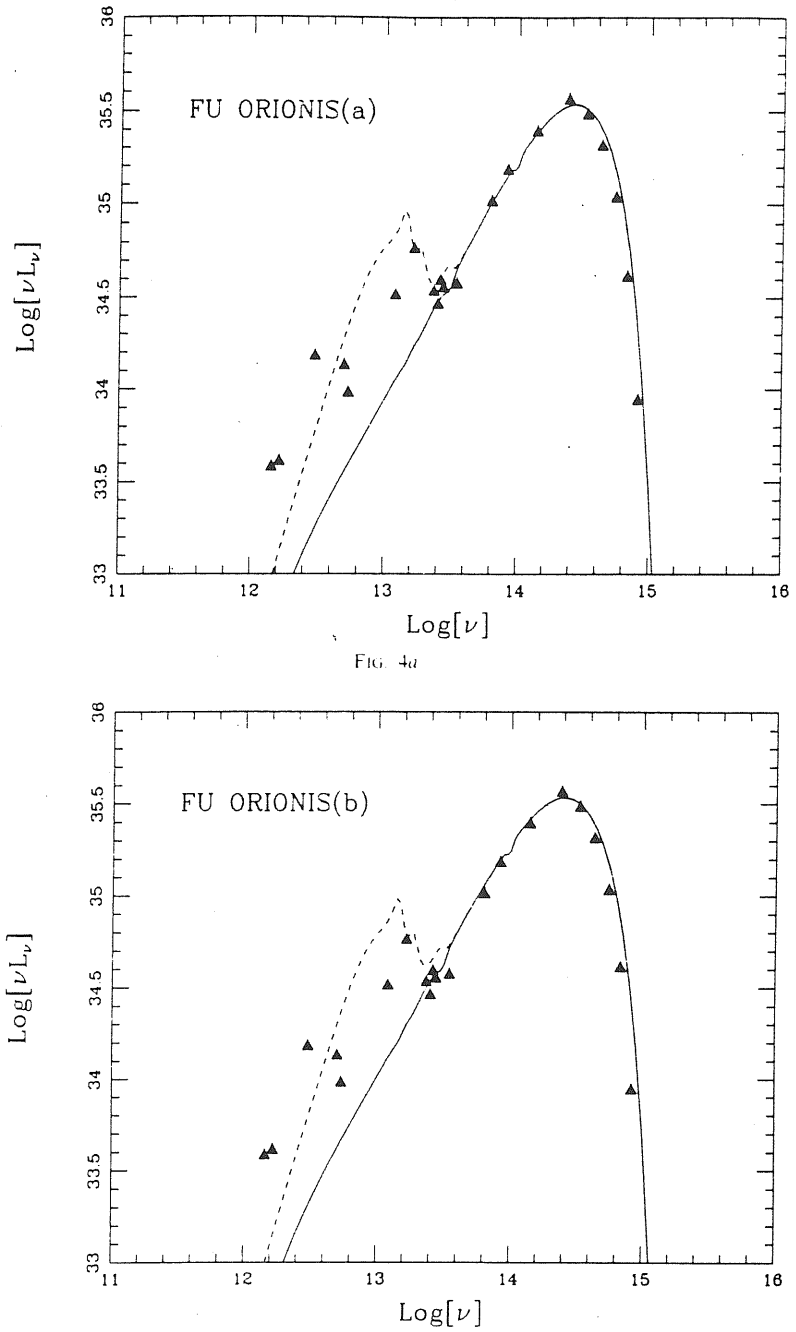

Fig. 2.14: FU Orionis: data from Smith *et al.* (1982); (a) the disk is passive and only radiates photons intercepted from the (outbursting) star with temperature $T_\star = 7000\ K$; (b) the disk is active and provides all of the outburst luminosity in an accretion process through a Keplerian disk. The dashed curve in both figures shows the emission from a surrounding dust shell with a covering faction equal to 0.1). Both cases require $L = 400.0\ L_\odot$and $A_v = 2.4 mag$ (Adams *et al.*, 1982).

CHAPTER III

Data Reduction

§3.1 *Introduction*

We aim at determining the spectral types and effective temperatures of a group of T Tauri stars members of the Chamaleon 1 and 2 dark clouds. In order to achieve our goals we have collected ESO–CASPEC medium–high resolution spectra of 15 T Tauri stars members of the two clouds and of 6 spectral type standard stars.

The spectral range covered is between $\lambda 5750$ and $\lambda 6570$ and the resolving power is $\frac{\lambda}{\Delta\lambda} = 20,000$. The spectrograph CASPEC on the ESO 3.6 m telescope is a very powerful instrument for mediun–high dispersion spectroscopy. The optical layout of CASPEC is outlined in Fig. 3.1. In the standard configuration, which is presently offered to the observers, an échelle grating with 31.6 $lines/mm$, a cross disperser at 300 $lines/mm$ and the so-called short camera (291 $mm, f/1.46$) are used. As it is well known, the role of the cross disperser, a low dispersion grating or prism whose dispersion is perpendicular to that of the échelle, is to eliminate the overlapping of the orders (e.g. Kitchin, 1984). Very high spectral orders must be used to obtain high resolving power. (1985). A thin back illuminated RCA chip is used as a detector; it is 512 rows by 320 columns device with pixel size of $30 \cdot 30\mu m$. This size corresponds to 1.22 *arcsec* in the direction of the disperser and to 0.7 *arcsec* perpendicular to it. The columns of the CCD are normally in the direction of long dimension of the slit. An example of a spectrum is shown in Fig. 3.2. The CCD detectors are presently the most commonly used detectors for astronomy. Useful references for astronomy applications are in Ford (1979), Timothy (1983), Mac Kay (1986).

In this section we discuss the reduction of our échelle data in order to put in evidence some of the important problems which we have encountered in this study.

§3.2 *Echelle Reduction.*

For the reduction of our échelle data we have used the échelle package inside MIDAS (1988). We will describe the standard reduction (STANDARD) method and an alternative method (IUE-like) that we have both used to performe the échelle reduction and to check the results. Useful references available are Ponz and Brinks (1986) and D'Odorico and Ponz (1984).

We have also used the échelle package inside IRAF (1987) only for one star (Sz 17) of our sample. The aim is to compare the two packages to see if there are some differences or one of them give a more conveniente method for the échelle reduction. Preliminarly we can say our test has shown that there are no significative differences in the results and the two échelle reduction package are equally efficient.

3.2.1 *MIDAS Reduction*

In this section we descrive the reduction method used with MIDAS. However we must emphasize that the reduction strategy is the same for all échelle data reduction packages, IRAF included.

In order to properly reduce the échelle spectrum of an astronomical source (OBJ) we must obtain the following sequence of échelle images (to be taken with the same instrumental configuration):

i) short exposure of dark (BIA)

ii) wavelength calibration image (WLC) (Fig. 3.2)

iii) flat field image (FLT) (Fig. 3.3)

iv) astronomical objects (OBJ) (Fig 3.4)

v) dark image (DRK)

Optionally, if we are interested in obtaining internally consistent fluxes (relative), we observe a calibration standard stars. The reduction of the standard star needs the same sequence of images as the OBJ, namely:

i) short exposure of dark (BIA)

ii) wavelength calibration image (WLC)

iii) flat field image (FLT)

iv) standard star (STD)

v) dark image (DRK)

At very last step of the OBJ reduction process we use the *response* of the STD reduced in the same way as the OBJ in order to get internally relative fluxes (section 3.2.1.6).

The WLC image is the spectrum of the Thorium calibration lamp, while the FLT image corresponds to the spectrum of the Quarz lamp, both taken with the same configuration as the object(s). For the wavelength calibration we used the Atlas of Thorium emission lines (of D'Odorico *et al.* 1986).

The main goals of the data reduction procedure is to extract the orders and to find the dispersion relation in one dimension. In order to achieve these goals we perform the following steps:

1. determination of the correspondence between the space (λ, m), i.e. wavelength λ and spectral order m and the space (x, y) i.e. column x and row y in the raw image. The aim is to identify the position of the order on the raw image and to define the wavelength scale of the reduced spectrum;
2. estimate of the image background;

3. correction of the interference fringes produced within the silicon. These fringes are especially important at long wavelengths ($\lambda > 6000\mathring{A}$);
4. order extraction;
5. wavelength calibration;
6. correction of the photometric profiles of the spectral order by the instrumental effects;
7. conversion of the counts into relative fluxes.

The steps summarized above are for the STANDARD reduction method. There is an alternative method applicable to the échelle reduction. The only difference from the standard method concerne points 6 and 7. It uses a different way to correct the instrumental effects (point 6) and it does not use standard stars (point 6). Table 3.1 shows the process scheme in a typical reduction session: italic fonts indicate optional operations. We now describe this with more accuracy.

3.2.1.1 *Order Definition*

As said before the first point is to find the order position in the raw image. This is defined by the following equation

$$y = f_1(x, m)$$

where m is a given order and the function f_1 is approximated by a polynomial of the form:

$$y = f_1(x, m) \approx \sum_{i=0}^{I} \sum_{j=0}^{J} a_{ij} x^i m^j \qquad [3.1]$$

the coefficients a_{ij} are evaluated using least square techniques on a grid (x_k, y_k), i.e. column number x_k and line number y_k of points located within the spectral order of the image. These points in the grid are found automatically by a maxima–following algorithm, normally using the flat image, as follows:

- A first guess of the order is found on a trace perpendicular to the dispersion direction done in the middle of the flat field image, in this way we define the set of points (x_o, y_{om}), m being the relative order number.
- For each order, a maxima–following algorithm finds the series of points located on the order at $x_n = x_o + n \cdot \Delta x$ for points on the right half of the order, and at $x_{-n} = x_o - n \cdot \Delta x$ for points on the left half of the order, where n=1,2,.. integer and Δx is the step of the grid.

This set of points forms the basic grid with the geometric positions of the orders. Typical values of the standard deviation of the residuals of this approximation are below 0.5 pixel. Good results are obtained with I=1, I=2, that is, each order is approximated by a straight line with distances between orders changing gradually.

Experience has shown, however, that it is hard to accomplish a global good fit for all regions within a frame. Polynomial degrees too low will not take into account small spatial variations on the slight distortions introduced by the spectrograph camera. On the other hand, polynomial degrees too high will introduce the well known wiggling effects which make the software slit run across the signal like a drunken driver speeding on a highway. In general both effects are worst at the extreme ends of all orders and at the uppermost and lowermost orders of a particular frame. In the finally reduced spectrograms this can lead to ugly wiggling at wavelengths where the orders usually overlap and a loss of calibration at the very beginning and end.

The algorithm used to detect the position of the orders is also used in the detection of the comparison lines during the wavelength calibration. This method works as follows: let us consider a vertical (almost perpendicular to the orders) trace in the row image in order to obtain one dimensional scan $h(x)$ like in Fig. 3.5. This allows to detect emission lines of width, say, w pixels which is the expected order width. Then the algorithm filters the scan with a running

median filter, using a window of $2 \cdot w + 1$ pixels, to obtain the resulting scan $h_1(x)$ without the emission features. The orders (or lines if you are using the algorithm for wavelength calibration) are detected if $h(x) - h_1(x)$ is greater than a given threshold t. The combination of these two parameters, w and t, provides a clean way to detect emission-like feature and during the reduction it is convenient to check both.

3.2.1.2 *Background Definition*

The background depends mainly on the characteristics of the detector, but includes the additional components of the scattered light in the optics of the spectrograph. The determination of the background is one of the critical aspects of the échelle spectra reduction (e.g. Finkenzeller and Basri, 1986) and particular care has to go in estimating the background in either FLT, the OBJ or (optionally) the STD for two reasons:

it affects the determination of the relative fluxes of the object spectrum, and it affects the accuracy with which instrumental effects can be corrected for.

The background of a CASPEC image consists of:

- a constant of CASPEC introduced by the electronics (BIA);
- an optical constant due to the pre–flashing of the CCD (when a preflashing is used);
- the dark current;
- the scattered light;
- the diffuse light in the interorder space coming from adjacent orders.

The BIA can be measured by obtaining a series of DRK exposures of short duration which are averaged to reduce the effect of the read-out noise of CCD. If *preflashing* is necessary to improve poor charge transfer efficiency, a set of preflashed DRK exposures must be obtained in a similar manner. To monitor

the *dark current*, it is convenient to obtain a set of DRKs of similar exposure times as the object and standard frames. Regarding the *general scattered light* and the *diffuse light* in the interorder spacings, a analysis of a flat field image shows that, in the long wavelength range and for a high level of exposure, most of the background contribution is coming from scattered light. For images taken at shorter wavelengths, and/or with a lower exposure level, the diffuse light from adjacent orders is the main component of the background.

After a BIA frame (or a preflashed BIA), has been constructed, it should first be subtracted from the FLT, OBJ and STD frames. Due to time limitations one has, in general, only a few long DARK exposures, for each exposure time. As no fine scale structure is present in these frames, the noise level can be suppressed by applying a suitable filter. The resulting DRK exposures can then be subtracted from the OBJ and STD frames. The remaining background is estimated from points located in the interorder space. These points are used to approximate the observed background by a polynomial of two variables, x and y as:

$$B(x,m) \approx \sum_{i=0}^{I} \sum_{j=0}^{J} b_{ij} x^i y^j \qquad [3.2]$$

where b_{ij} are the coefficients of the polynomial.

In our case we have observed that the background of flat field images was generally well modelled by $2-D$ polynomial of degrees $I = 3$ and $J = 3$. The number I refers to the degree of the polynomial in the x-direction (along the dispersion); the number J is the polynomial degree in the y-direction (perpendicular to the dispersion). Fig. 3.6 shows a trace perpendicular to the dispersion direction through a flat field frame and the background fitted to the interorder locations. For OBJ exposures of low signal–to–noise ratio we must use a polynomial of a lower degree. If the BIA and DRK components are subtracted from the OBJ frame, a plane is very often a good approximation to the background component. The value $I = 1$ and $J = 1$ is usually appropriate for faint sources.

The fitting of this background can be very difficult to impossible if in addition the object spectrum is complex with strong lines. When working with bright objects it is easy to see how errors of the order of 10% in the intensity measurements near strong lines (either emission or absorption) could occur. It is clear that the background subtraction for faint sources is very delicate. For these reasons, together with the fact that the entrance slit of CASPEC is rather small and refraction in the earth's atmosphere can differentially affect the throughput of CASPEC it is not possible to obtain an absolute calibration for CASPEC data.

It has to be noted that small errors in the determination of the background are carried through the whole rest of the reduction and are even amplified at the edges of the orders; if no BIA and DRK are available, the background definition migh be sligltly less accurate because the modelling procedure has to take into account these contributions too. For this reason a useful tip to the observers is to gather a set of short, optionally pre-flashed, DRK exposures which can be averaged to produce a BIA frame. Further one needs a set of long DRK exposures which, after smoothing to reduce the noise, can be substracted from the OBJ frames.

As explained above, the contribution to the background by the scattered light is determined by the points located between the orders. The accuracy with which the background can be determinated depends on the exposure level of the frame and on the interorder space. If the interorder space is too small, the background level will be over estimated by an unknown amount. Given sufficient space between the orders, the systematic deviations are estimated to be less than 1%. Fig. 3.7 shows a trace perpendicular to the dispersion direction through an object frame in the blue region of the spectrum and the total estimated background. Fig. 3.8 shows the individual components which contribute to this background.

3.2.1.3 *Flat Field Correction*

As the use of CCD has become more and more common in astronomy, the procedure of flat–fielding a CCD image, namely to correct for offset values in the pixel intensity read–out, due to deviations from linearity and due to chip defects, has become an art in itself. An additional feature which is particularly bothering in échelle spectra taken with the thinned, back illuminated RCA CCD is the fringing effect, due to reflections in the thin silicon layers of the CCD. They produce an interference pattern whose variations depend on the wavelength of the incident light and the CCD thickness. The effect is as high as 50% at $\lambda > 6000\mathring{A}$ (York *et al.* 1981). Some tests have confirmed that this effect is constant for a given setting and it can be effectively corrected by dividing the object image by a flat field exposure taken with the same instrumental configuration. Before the actual division is carried out, the background levels obtained in the way described above, both in the object image and flat field, have to be subtracted.

With CASPEC the FLT images is accomplished by illuminating the entrance slit of the spectrograph with a built-in incandescent lamp. A well–known problem when using the incandescent lamps is that its light path through the optics is slightly different from the one taken by the stellar light. In the most general case this results in a small positional offset of the stellar and flat field orders on the chip. For a proper pixel to pixel division, the flat field orders should be appreciably wider than the stellar signal in order to ensure complete overlap by the flat. This is shown in Fig. 3.9 where we have overlapped a part of a vertical trace of the OBJ image and a same part of vertical trace of the FLT image: here it is possible to put in evidence a slight shift of the order center of the OBJ to respect the order center of the FLT ($\sim$ 1 *pixel*). Note that the FLT order is much larger than the OBJ order; if it were not, the stellar signal pixel would be divided by lower underexposed flat field pixels and give rise to

spurious noise spikes. Therefore it is advisable to use a slit as long as possible for the flat without crowding the orders and to choose the flat field exposure for the order tracing algorithms (see section 3.2.1.1) rather than the stellar signal. Use of the stellar signal to trace the orders can be problematic if there are deep absorption lines in the spectrum. The fact that there is subtle, but not negligible, mechanical flexure in the spectrograph when moving the telescope from a program object to the standard star does not help. All these factor may cause the software slit to miss some fraction of the stellar signal, resulting in subsequent calibration problems. Finally, when the slit height is too small, there can be digital sampling error as the software slit slants across the frame, leading to a few percent ripple in the measured total counts. These problems largely disappear if one is able to use a sufficient slit height which can be done longward of $5000\mathring{A}$ where the interorder spacing is adeguate.

The method of dividing the object image by the flat field in the pixel–pixel space gives better results than the alternative method consisting in the division of the extracted orders of the object and flat field images. This last method has to used when the FLT order are not wider than the OBJ orders. The accuracy achieved when dividing by the flat-field in the pixel-pixel space depends on a number of factors, such as the wavelength range and the intensity of the signal.

The flat field correction procedure will also correct, at least in a first order approximation, for the blaze effect (see sections 3.2.1.6 and 3.2.1.7). If one corrects for the instrumental response using a standard star, it is necessary to take into account differences in the flatfield exposure belonging to the OBJ and the one corresponding to the STD. This is done by normalizing the flatfield: namely it is produced a smoothed versions of the FLT and then they are divided.

3.2.1.4 *Other Extraction*

Individual échelle orders are extracted by averaging the pixel values over a numerical slit running along the orders. Due to the instrument configuration, the slit runs perpendicular to the CCD-columns. The center of the slit is defined by equation [3.1]. The actual extracting methods includes as parameters the length of the numerical slit in pixels, an optional offset to shift the center of the slit and an angle if the slit is not perpendicular to the CCD columns (not relevant in CASPEC). Three methods may be used to performe the actual integration on the numerical slit.

In order to simplify the explanation let us assume a numerical slit consisting of three pixels.

1. *Nearest neighbour method*: the number of counts collected by the numerical slit at a given position is the sum of the pixel values closest at the actual slit elements. No interpolation is performed. The number of counts is simply

$$D = w_1 \cdot D_1 + w_2 \cdot D_2 + w_3 \cdot D_3 \qquad [3.3]$$

   where D_i are pixel values, and $w_i = 1/3$.

2. *Linear interpolation with constant weights method*: the number of counts at a given position is given by:

$$D = w((1 - a) \cdot D_1 + D_2 + D_3 + a \cdot D_4)) \qquad [3.4]$$

   where the value is the offset between the image pixel and the slit pixel, and $w = 1$ or $w = 1/3$. The first case corresponds to simply adding all the flux entering the numerical slit; the second case corresponds to a weighted average with $\sum_{i=1}^{3} w_i = 1$.

3. *Linear interpolation with weights proportional to the order profile method*: this is similar to the previous one, but the weights of the slit elements are proportional to the normalized profile of the order perpendicular to the dispersion direction. The number of counts is computed as:

$$D = w_1 \cdot ((1-a) \cdot D_1 + a \cdot D_2) + w_2 \cdot ((1-a) \cdot D_2 + a \cdot D_3) + w_3 \cdot ((1-a) \cdot D_3 + a \cdot D_4) \quad [3.5]$$

with $\sum_{i=1}^{3} w_i = 1$.

Due to the inclination of the orders in the actual data format, the first method is not suitable for CASPEC. Orders extracted with this method present a periodic variations of about 10% of the signal. This periodic feature is substantially reduced in the second method if the slit consists of 5 to 7 pixels, but in this case the signal/noise ratio is not optimal due to the uniform pixel weight. The orders extracted with the third method have a better signal/noise ratio and, for a slit of 5 to 7 pixels, the actual weights, computed for each order, take into account the variation of the order in the image. The method is still under test.

3.2.1.5 *Wavelength Calibration*

The dispersion relation in one dimension is given by

$$x = f_2(\lambda, m) \quad [3.6]$$

In the reduction procedure the orders of the WLC image (obtained with the same instrumental configuration and the same position of the telescope as the scientific frame) are automatically defined via the flat-field exposure, and extracted using a sampling step of 1 pixel. They are then used to compute the dispersion coefficient for each order in three steps:

1. The calibration lines are identified with a detection criterion which is based on the width of lines and their intensity above the background: an algorithm

consisting of a median filter and a threshold as explained at the end of section 3.2.1.1.

2 The actual position of the lines is defined as the centre of gravity of the two brightest pixels relative to the third brightest. Initial guesses for the wavelength calibration is obtained by entering manually the identification of a few lines in the 2–D WLC frame, and then improved by comparison with the reference catalogue of Thorium line (D'Odorico *et al.* 1987).

3. The dispersion coefficients are computed by means of a regression analysis, by relating the identified lines to the Thorium–Argon line catalogue available in the system. A polynomial of degree 3 is sufficient to obtain, for each order, a good approximation of the wavelength scale in CASPEC. The residuals are computed as:

$$\Delta\lambda = \lambda_{lab} - \lambda_c = \lambda_{lab} - (a_0 + a_1 \cdot x + a_2 \cdot x^2 + a_3 \cdot x^3) \qquad [3.7]$$

The r.m.s of the residuals in a well calibrated image is about $0.03A$, less than $1/4$ of a pixel at $5000A$. In practice, it is very easy to make the wavelength calibration. The program will display the wavelength calibration spectrum and ask you to identify two lines and their orders. This is easy to do using the cursor, the hard copy of the spectrum and the catalogue of Thorium line. It is convenient to identify lines near any two diagonally opposite corners of the display. The program will then try and identify lines it has previously found. In this procedure it uses both the position of the lines and their intensity. If it cannot find a solution it will ask you to help it by identifying additional lines and checking the existing identifications. The wavelength calibration is a very critical step in the procedure so it is a good idea to "vaste" some time at this step to make sure that you get a good wavelength calibration.

It is convenient to obtain r.m.s. scatter of $1 \div 2 \cdot 10^{-2}\mathring{A}$. Fig. 3.10 shows the behaviour of the residuals for the calibration image centred at $6200\mathring{A}$. If

the wavelength correction has to a greater error it can happen that the different orders will have different calibrations. Then when they are merged you will have "ghost" images of spectral features.

The width of the pixels in $\AA$, which is a function of the position, has been computed from the dispersion coefficients in a set of images covering the spectral orders 70 to 140. Table 3.2 summarizes the results for our spectral range. The dispersion coefficients for each order are in eq. [3.7]. These are used to rebin the extracted orders at a constant wavelength step. We have rebined at $0.15\AA$ to be sure that instrumental resolution is not lost. It is not useful to oversample too much the CCD pixels along the dispersion because this process does not introduce any additional informations.

Tests to monitor the precision and stability of the instrument show that small variations of the dispersion coefficients are expected depending on the telescope pointing (Ponz and Brinks, 1986). It is recommended to take flat-field and wavelength comparison frame before or after each OBJ (STD) exposure. The reduction procedures have been optimized in such a way that, for a given instrument configuration, only the first set of dispersion coefficients have to be computed interactively. Subsequent dispersion coefficients are computed using the previous one as guesses, in a completely automatic mode. In those cases where one needs a good overall relative calibration and one wants to ensure a good overlapping of the orders, standard stars should be included in the observations, at least one for each instrument configuration, with the corresponding flat-field and wavelength comparison exposure with the following sequence:

$$\mathrm{DRK}\longmapsto\mathrm{STD}\longmapsto\mathrm{FLT}\longmapsto\mathrm{WLC}\longmapsto\mathrm{OBJ}\longmapsto\mathrm{FLT}\longmapsto\mathrm{WLC}$$

3.2.1.6 *Response Correction Using Standard Stars (Standard Method)*

The extracted orders, resampled using the dispersion relation described in 3.2.1.5 section, give the observed spectrum (in counts) as a function of the wavelength for each order. In these profiles two instrumental effects are present:

i) the blaze effect of the échelle grating;

ii) the fact that the efficiency of the whole instrument is not uniform with respect to the incident wavelength.

For a given configuration the blaze effect is a function of the position in the order, while the instrument response is, essentially, a function of the wavelength. The solution adopted is to use a standard star to correct for both, blaze effect and instrument response, simultaneously. The STD, observed with the same configuration as the OBJ, is reduced using the corresponding normalized flat-field frame. After that, correction factors are calculated by comparing the flux value in a table containing absolute fluxes for the standard stars to the observed counts of the STD which are sampled at the same wavelength intervals as the fluxes in the table. The resulting response is normalized to an exposure time of one second.

The observed flux is computed as

$$F_\lambda = R_\lambda \cdot \frac{D}{T} \qquad [9]$$

where F_λ is the absolute flux (in $erg\ cm^{-2}A^{-1}s^{-1}$), R_λ is the compute response (in $erg\ cm^{-2}A^{-1}DN^{-1}$), D is the extracted Data Number (in DN) and t is the exposure time in seconds.

To illustrate now well this correction works we show in Fig. 3.11 a comparison between the observed standard star Kopff 27 and the corresponding tabulated absolute fluxes taken from Stone (1977). In this figure the standard star observation is treated as if it was a science frame. The response of the instrument, as derived on the basis of the same standard star observation, was applied to it.

The accuracy of the flux calibration, i.e. the correction for the blaze effect and the chromatic response, can be judget from the following figures: Fig. 3.12 shows three adjacent orders extracted from a raw observation, reflecting the influence of the blaze effect; Fig. 3.13 shows the same three orders after subtraction of the background, flat-fielding and flux calibration using a standard star.

3.2.1.7 *Response Correction Using the Blaze Function (IUE-Like Method)*

If no standard star is available with the same instrumental configuration as the object frame under consideration, a different approach is also available at this stage as an alternative to the method described above. It consists of correcting for the blaze effect introduced by the échelle grating by using a suitable model for the blaze function. In this approach, no correction for the chromatic response of the instrument is applied.

The échelle blaze function is an old problem in the reduction of IUE high resolution spectra. In our case the problem is even more complicated given the different possible configurations of the instruments. The blaze function $R(\lambda)$ at wavelength λ is approximated by:

$$R(\lambda) = \frac{\sin^2(\pi\alpha X)}{(\pi\alpha X)^2} \qquad [3.8]$$

where α is a "grating constant" and $X = m(1 - \frac{\lambda_c(m)}{\lambda})$, in which m is the order number, and $\lambda_c(m)$ is the central wavelength of order m. Both parameters m and $\lambda_c(m)$ are related through the "grating constant" k by $\lambda_c(m) = \frac{k}{m}$. The parameter α is not dependent on the order number and can be considered a constant for a given exposure with values between 0.5 and 1 depending on the actual alignment of the instrument; the parameter k is a function of the order number with mean values given in Table 3.3.

This correction can be done by two different methods. We have to compute the parameters k and α:

i) The first method is a modification of the method suggested by Ahmad (1981); his algorithm approximates the blaze function by a *sinc* squared and finds the function parameters by a non–linear least squares fit to the order profile. The method is suitable for objects without strong emission or absorption features and can be used to get a first estimation of the blaze parameters.

ii) The second method was proposed by Barker (1984). He uses the overlapping region at adjacent orders to estimate, in a few iterations the parameter k of the blaze function which is, as before, assumed to be a *sinc* square. The method works well, provided that order are overlapping and that there is a very good estimation of the parameter α, assumed to be a constant.

3.2.2 *IRAF Reduction*

As we have said at the begin of section 2.1 the studies that we have performed using the IRAF package are only preliminary. We had the opportunity to reduce only one star (Sz 17) and the method used does not give an intensity calibrated spectrum. Moreover we did not performed the blaze correction. Thus we are able to compare the IRAF results with those obtained using MIDAS in the IUE-like method before performing the blaze correction. In other words, looking at the scheme of Table 3.1, with IRAF procedure we have only performed the steps written in capital letters.

The main difference between our IRAF and MIDAS reductions is in the background subtraction procedure. In fact, in the MIDAS reduction we did not subtract the BIA and the DRK instead the background estimated from points located in the interorder space. As seen before (section 3.2.1.2) this is non perfectly correct but neither is a bad approximation because the BIA is almost

a constant and the dark current, which is proportional to the exposure time, too. We also add that, to avoid cosmic ray problem, background images should be combined with a median filter routine; in our procedure we did not filter any frame.

In the IRAF reduction we have filtered the 2–D DRK image of 30 minutes to eliminate some cosmic spikes and then we have estrapolated the resulting image to 5 *sec* to define the BIA image which has been subtracted from the flat field and object image. After that, the filtered DRK of 30 minutes has been subtracted from the object image.

§3.3 *Comparison Between Standard and IUE-Like Reduction*

A first reduction of the data has been performed in 1986 using the standard reduction. As we have described in section 3.2.1, in order to have a correct reduction in this way one should follow the scheme indicated at the end of 3.2.1.5 section for each instrument configuration. We did not have the images of the standard star for each T Tauri star of the sample. So, it was not perfectly correct to use a few images of standard stars for all the stars observed during observing run. The instrument response evaluated using the standard star was not perfectly correct for all the stars. And in fact we have observed that not all images, calibrated using the STANDARD reduction, were corrected for the instrumental effect. Fig. 3.14 is a tipical example in which it is possible to put in evidence the ripple effect, i.e. the bad linearization of the orders.

For example we can observe the star Sz 24 has been observed with two different exposure time (60 and 30 minutes): Fig. 3.15 and Fig. 3.16. On the top of each figure we have reported the star reduced with the IUE-like method and on the bottom the star reduced with the standard method. It is curious to

observe that in both procedures the short exposure maintains the order effect and that the long exposure is ok. Probably this is a problem of S/N ratio.

The same effect could also be seen in the star Sz 30 (Fig. 3.17). In the standard method the order effect is evident in the highest orders (near the H_α region). Using the IUE–like method we have an improved spectrum even if the order effect is not completely disappeared.

Another point that we like stress concerns the problem of broad absorption features (one order or more) which can missed during the reduction process. In our sample we have a few spectra which contain a broad molecular band due to TiO (the head of the band is at 6240$\AA$). In Sz 30, for example we clearly seen the depression of the continuum due to the molecular band but we cannot say if the slight emission inside the band is due to superimposed emission or is an order effect (Fig. 3.18). We have indicated the wavelengths of order edges to check if the order effect is responsible.

In the IUE–like method it is more convenient to use the method which uses the overlapping region of adjacent orders than one which is based on Ahmod (1981). In this last case the order effect is evident at the highest order (between 9 and 14). This agrees with the observation that this method works well for objects without strong emission or absorption features. In the high orders we have the strong H_α which characterizes the T Tauri stars. (See for example Fig. 3.19).

§3.4 *Comparison Between MIDAS and IRAF Reduction*

As said in section 2.2, we have reduced only Sz 17 by using IRAF. In this reduction we have used the scheme of Table 3.4. At first glance we did not observe, as of course one should expect, any substantial difference. In Appendix A we have reported all the extracted orders of Sz 17.

In order to make the comparison we have normalized the orders by dividing each order by the number of counts at the same wavelength coordinate for the IRAF and MIDAS spectra. In this way we get the same scale.

The different scale of the procedure were due to the fact that a different width of the numerical slit has been used during the orders extraction. By observing the plots of the extracted orders we can observe immediatly the blaze effect. In fact we did not perform the correction of the blaze function but we have only divided by the normalized flat field. A more accurate analysis of the orders shows a slightly behaviour of this effect at the edges of the orders. This is probably due to the different way used during background correction. Small errors in the determination of the background are carried through the complete reduction process and are amplified at the edges of the orders. The greater differences are at the end of the orders while in the middle the coincidence is very good.

Preliminar measures of equivalent width of several lines show that there are negligible differences between the two extraction softwers.

The reason we have spent time in comparing the two methods is due to the fact that it is very important for very weak object to define accurately the continuum and the shape of spectral features.

Just to give an example let us consider the normalization problem. Let us consider the spectrum of Fig. 3.20 which is a spectral type standards star. It is characterized by a strong TiO molecular band which extendes over about three orders. In this case it is very dangerous to normalize the spectrum order by order because it is very easy to mask the molecular bands and to define a wrong continuum. Not only in this extreme case but in general we believe that the best method to normalize the spectra is to consider the whole spectrum and to take some well defined points of the continuum to interpolate a smooter continuum. If this method is not possible, we can always normalize order by order by taking

into account all the points discussed above.

In our particular case it will be very important to define the exact continuum if we want to find some criteria for the spectral classification of the T Tauri stars.

Table 3.1: CASPEC Reduction scheme

FLT	WLC	STD	OBJ
⇓	⇓	⇓	⇓
FIND ORDER POSITION	EXTRACT ORDERS	*subtract background*	SUBTRACT BACKGROUND
⇓	⇓	⇓	⇓
subtract background	IDENTIFY LINES	*flat field correction*	FLAT FIELD CORRECTION
⇓	⇓	⇓	⇓
define blaze	COMPUTE DISP. COEFFIC.	*extract orders*	EXTRACT ORDERS
		⇓	⇓
		sample in wavelengths	SAMPLE IN WAVELENGTHS
		⇓	⇓
		compute response	*multiply by response or fit blaze*
			⇓
			MERGE ORDERS

Table 3.2

ORDER	CENTRAL WAVELENGTH Å	RESOLUTION Å/Pixel
84	6770.8	0.210
85	6691.1	0.208
86	6613.2	0.205
87	6537.2	0.203
88	6462.9	0.201
89	6390.2	0.199
90	6319.2	0.196
91	6249.8	0.194
92	6181.9	0.192
93	6115.4	0.190
94	6050.4	0.188
95	5986.7	0.186
96	5924.4	0.184
97	5863.3	0.182
98	5803.5	0.180
99	5744.9	0.178

Table 3.3

GRATING lines/mm	K	α
31.6	568746	0.8
51.	344705	0.8

Table 3.4: IRAF Reduction scheme

WLC	FLT	OBJ
⇓	⇓	⇓
EXTRACT ORDERS	FIND ORDER POSITION	SUBTRACT BACKGROUND
⇓	⇓	⇓
IDENTIFY LINES	*subtract background*	FLAT FIELD CORRECTION
⇓		⇓
COMPUTE DISP. COEFFIC.		EXTRACT ORDERS
		⇓
		SAMPLE IN WAVELENGTHS
		⇓
		MERGE ORDERS

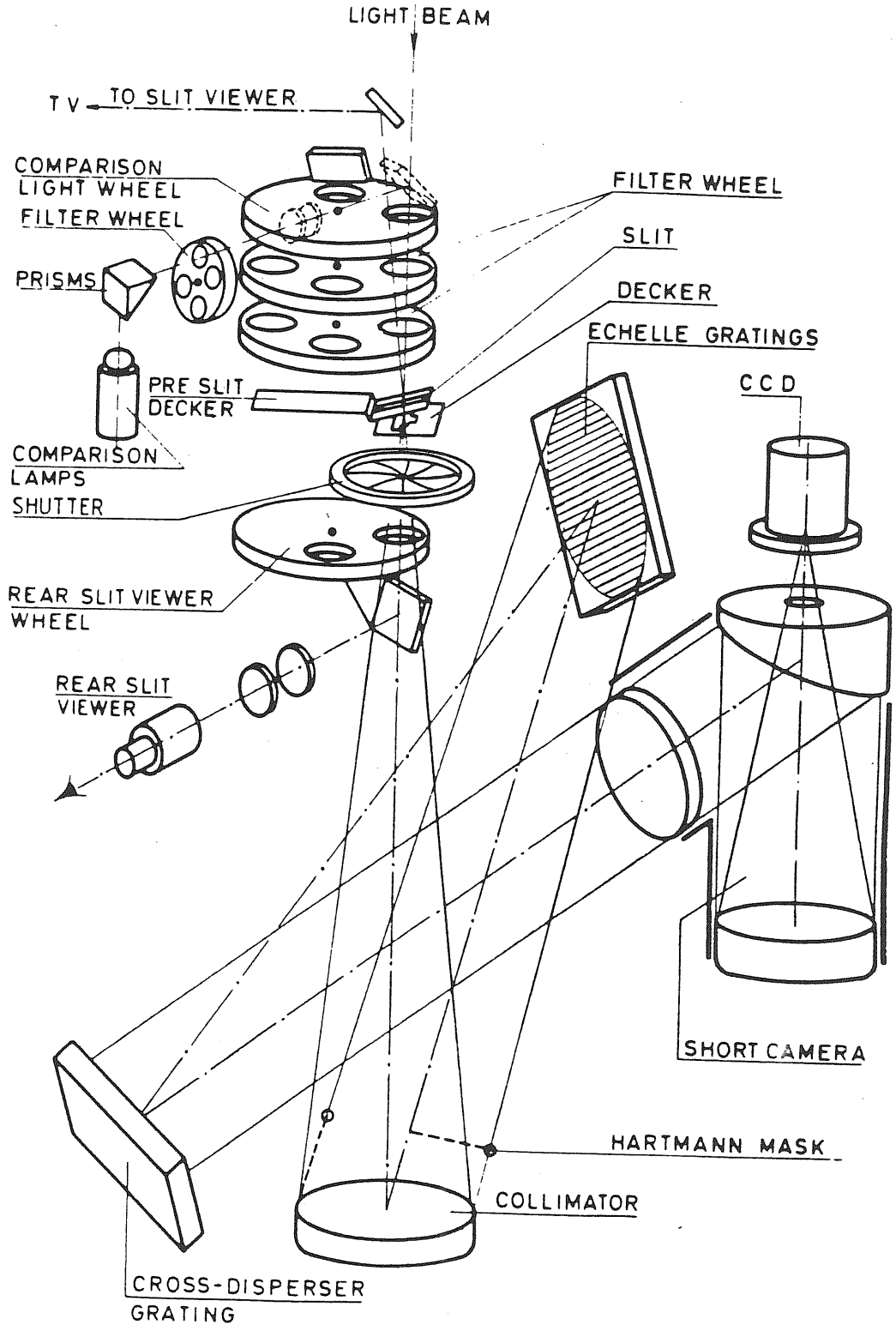

Fig. 3.1: Optical layout of CASPEC.

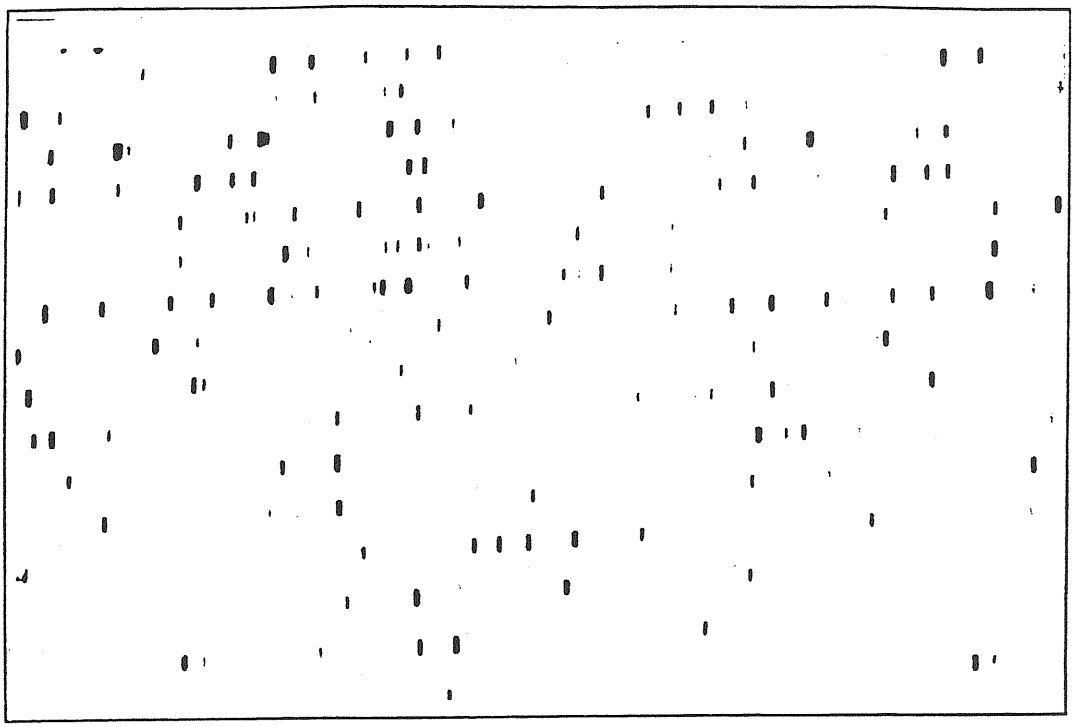

Fig. 3.2: A CASPEC exposure of the thorium lamp.

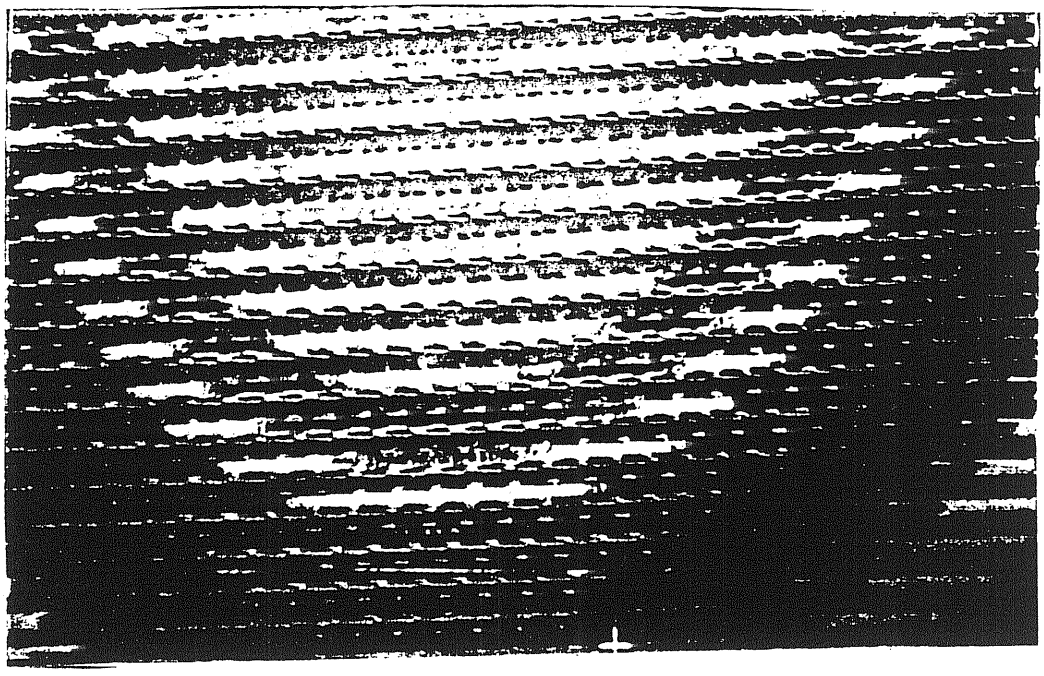

Fig. 3.3: A CASPEC flat field image.

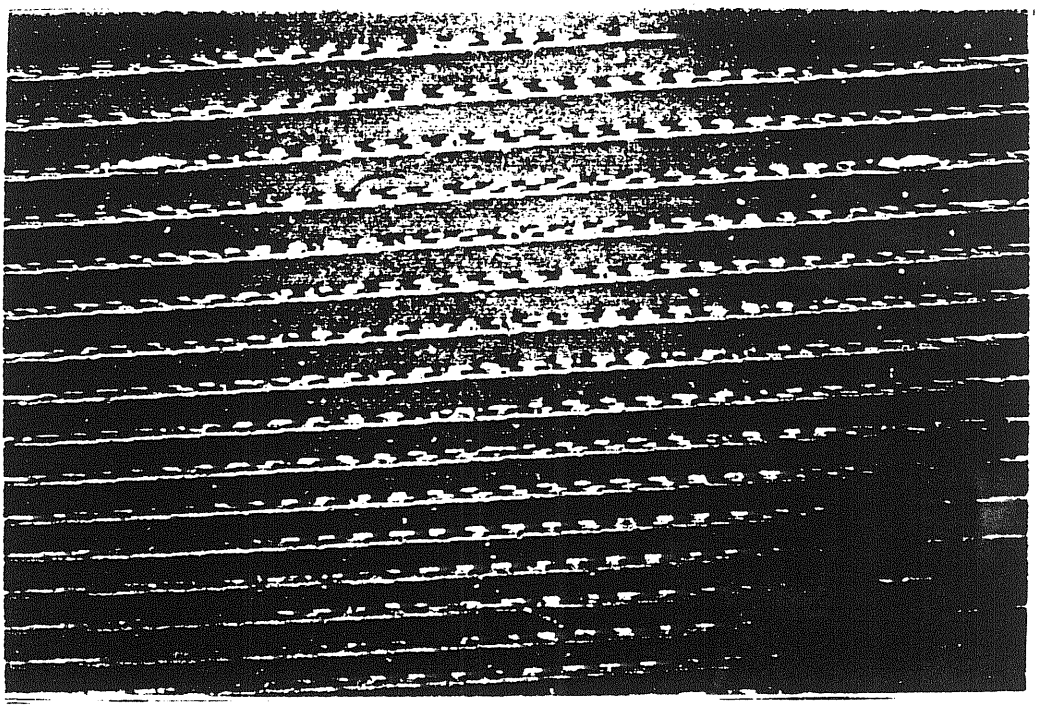

Fig. 3.4: A CASPEC observation obtained of the T Tauri star Sz 3. The exposure time is 60 *min* and the central wavelength is 6200$\AA$. Note the strong emission of H_α.

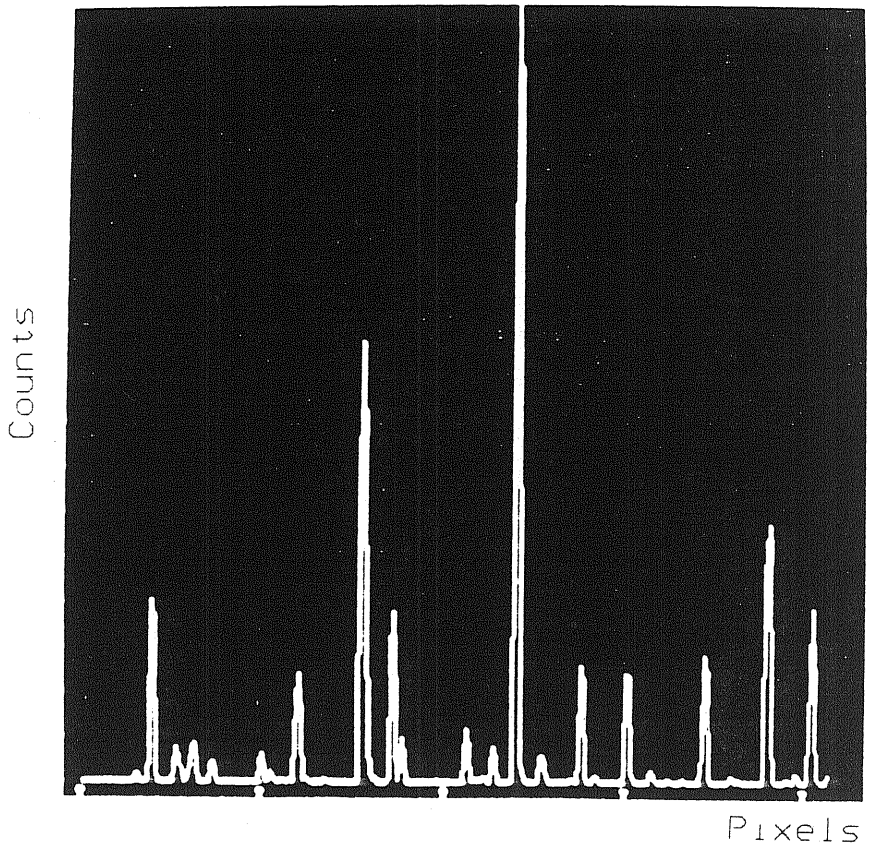

Fig. 3.5: A order extracted from the WLC image.

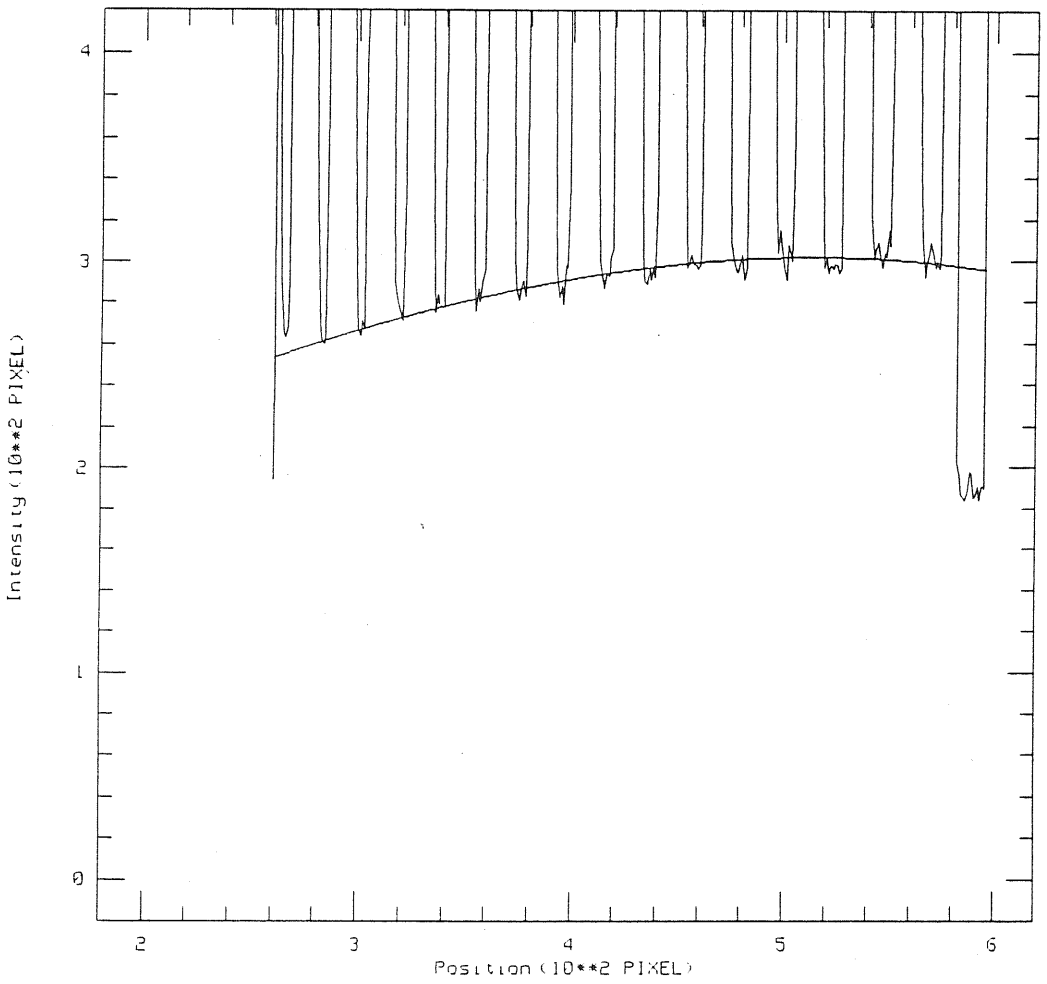

Fig. 3.6: Trace perpendicular to the dispersion direction through a flat field image showing the fitted background (Intensity in Counts).

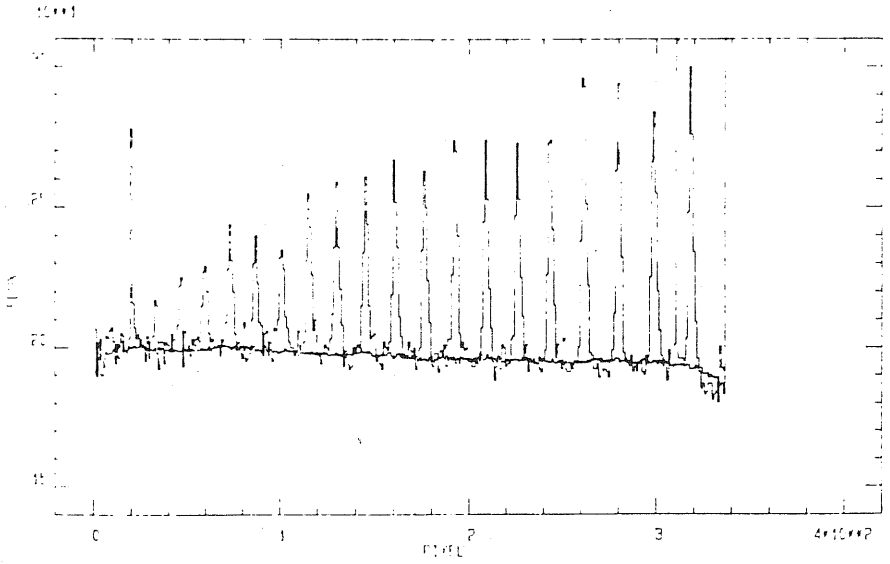

Fig. 3.7: Trace perpendicular to the dispersion direction through an object frame in the blue range accessible to CASPEC showing the estimate background (Flux in Counts).

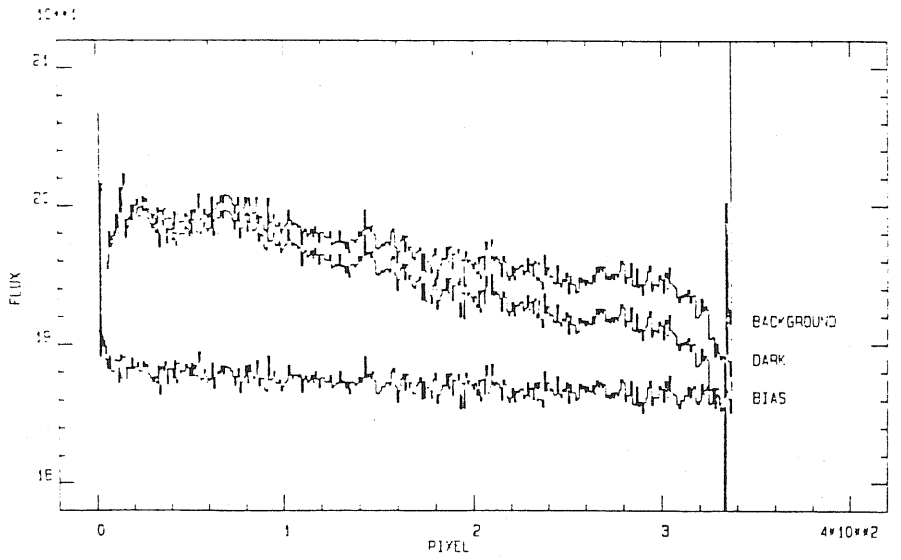

Fig. 3.8: Components contributing to the background displayed in Fig. 3.7. The upper trace labelled "background" is the addition of the bias, bottom curve, dark, middle curve, and the fitted residual background due to scattered light (Flux in Counts).

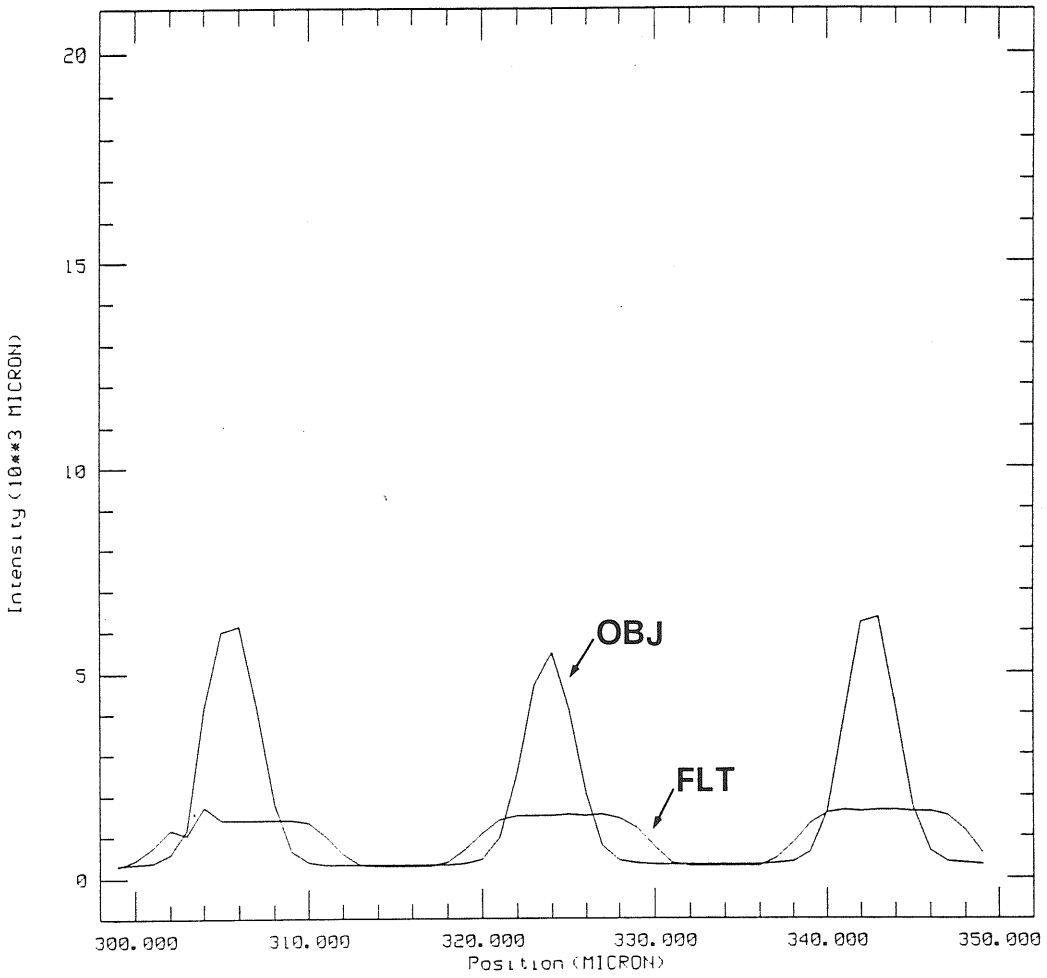

Fig. 3.9: A part of a vertical trace of the OBJ image and a same part of vertical trace of the FLT image overlapped.

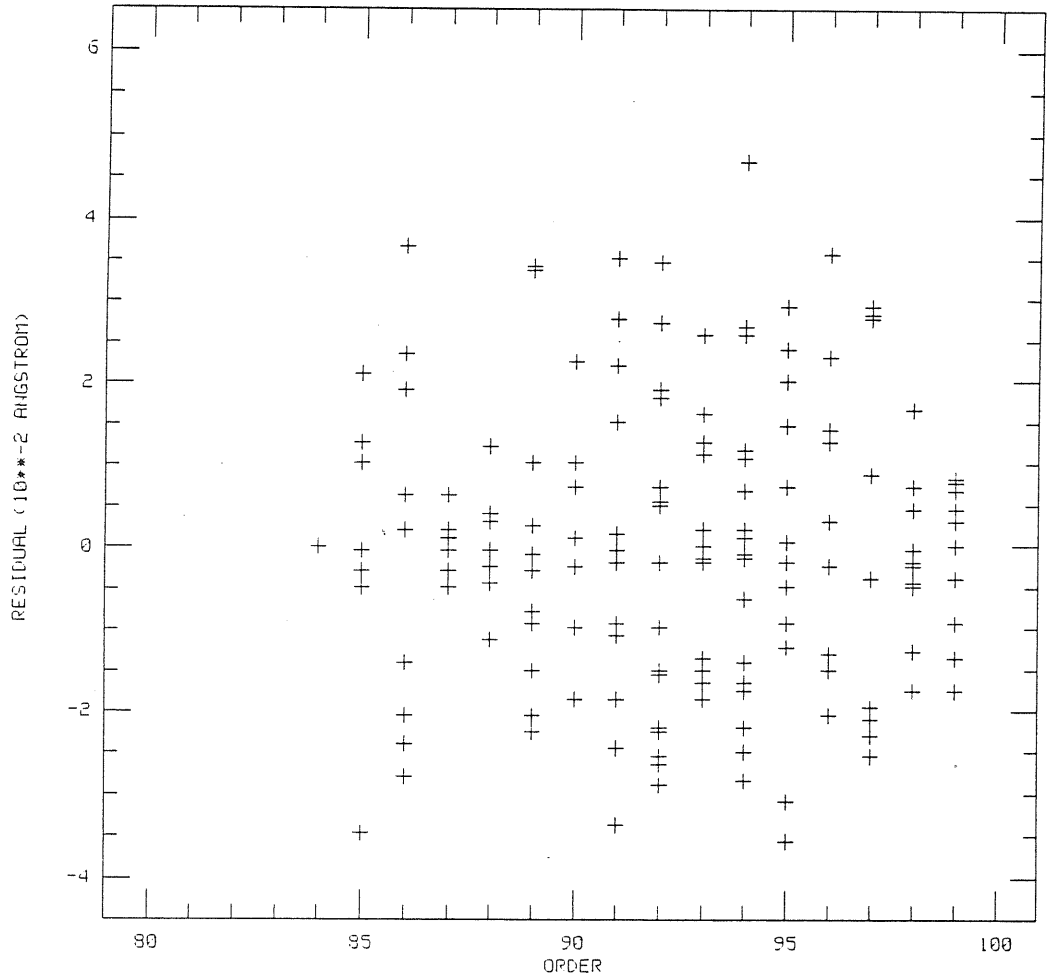

Fig. 3.10: Plots of the residuals $\Delta\lambda = \lambda_{lab} - \lambda_c$ for the central wavelength 6200$\mathring{A}$.

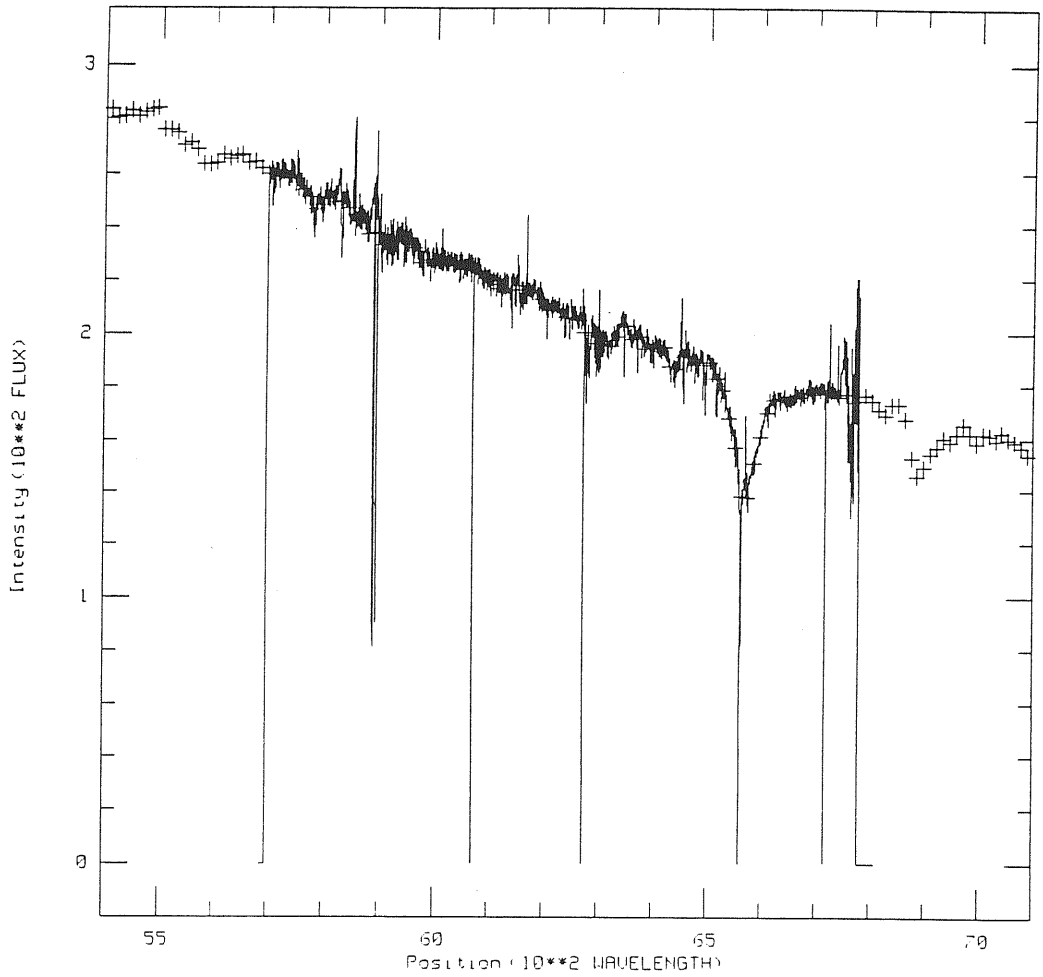

Fig. 3.11: Comparison between the observed standard star Kopff 27 and the tabulated values to lower resolution.

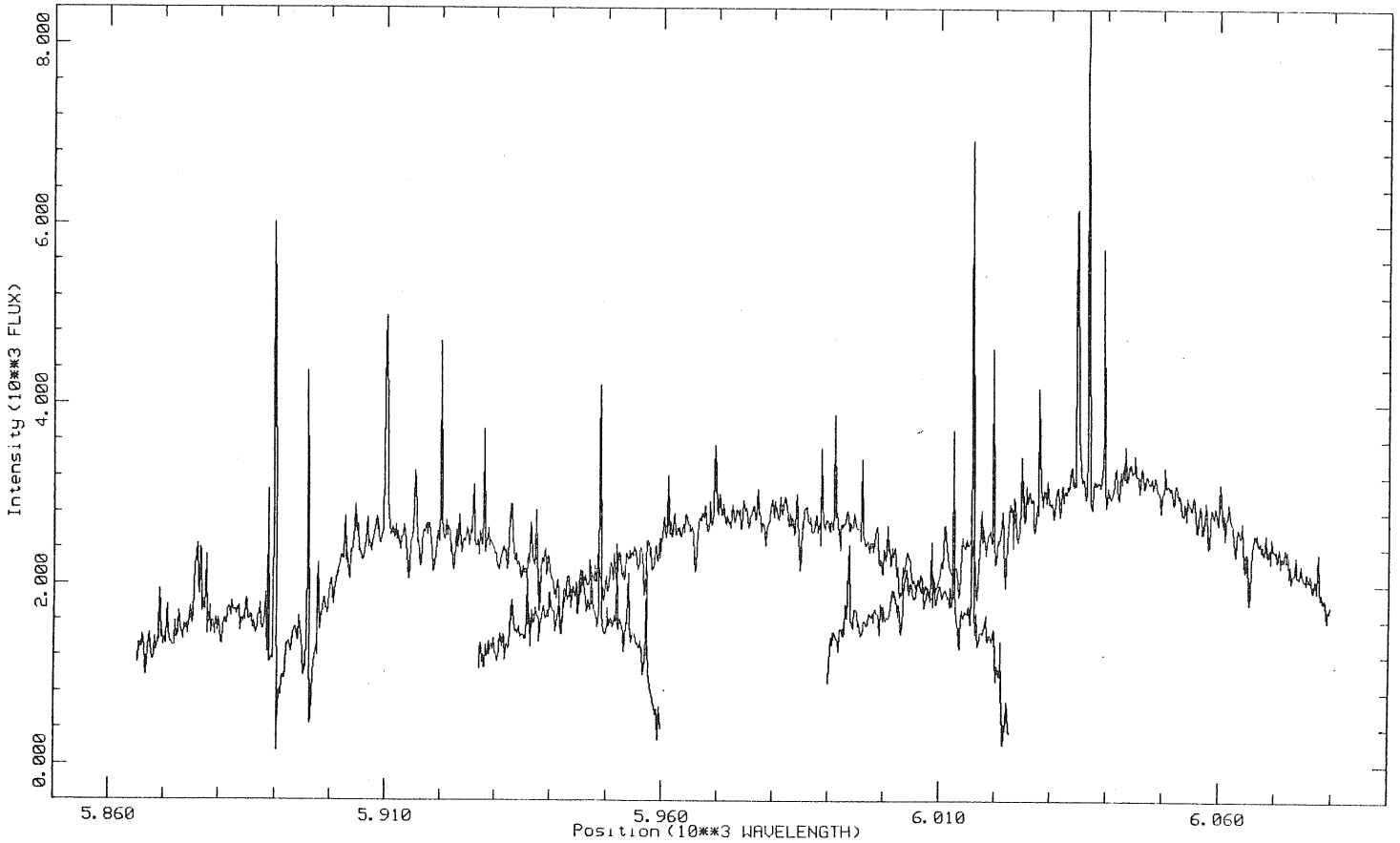

Fig. 3.12: Extracted data numbers from three adjacent orders (stars Sz 17) showing the échelle blaze effect.

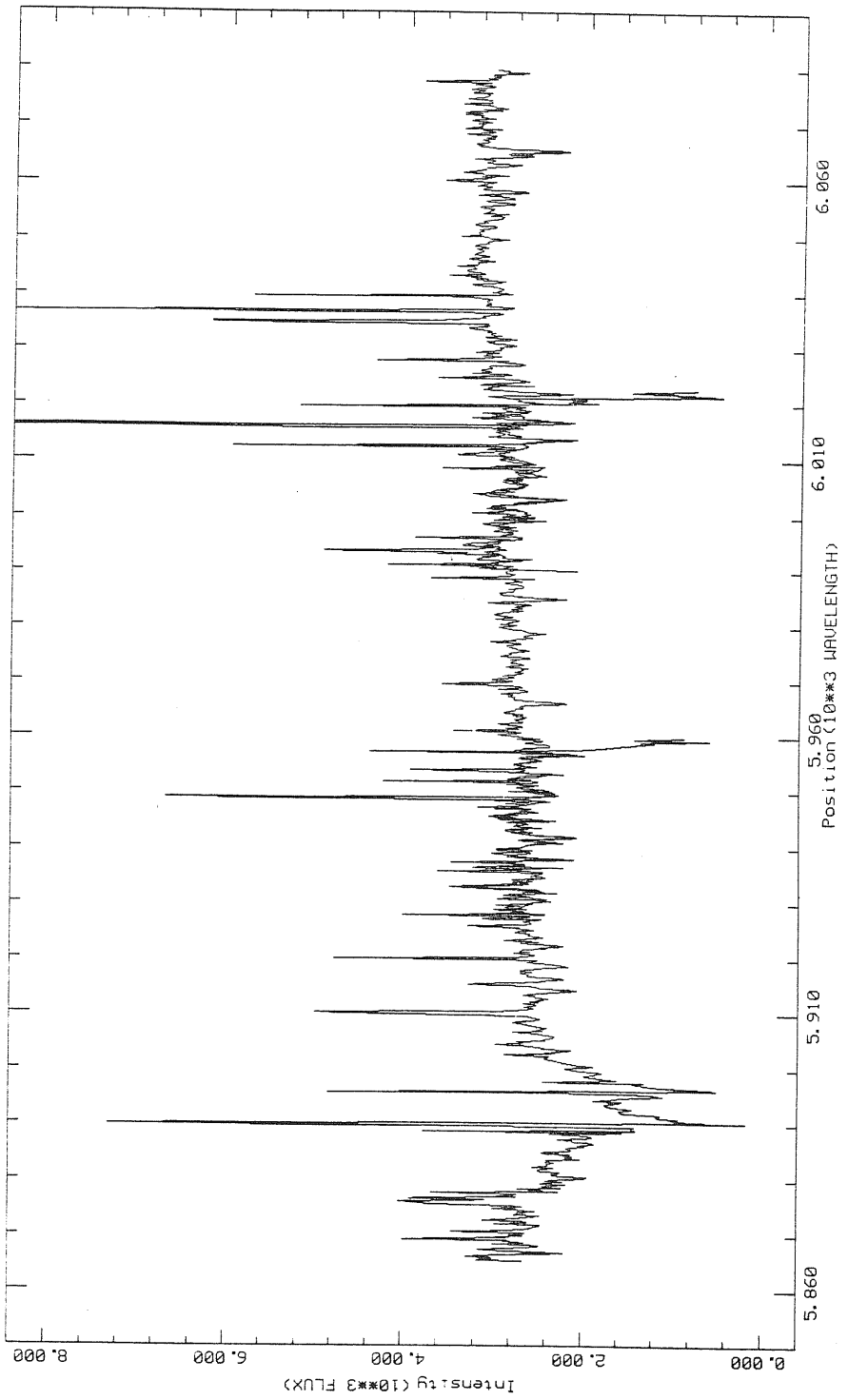

Fig. 3.13: The same three orders as in Fig. 3.12 after correction for the instrument response using a standard star.

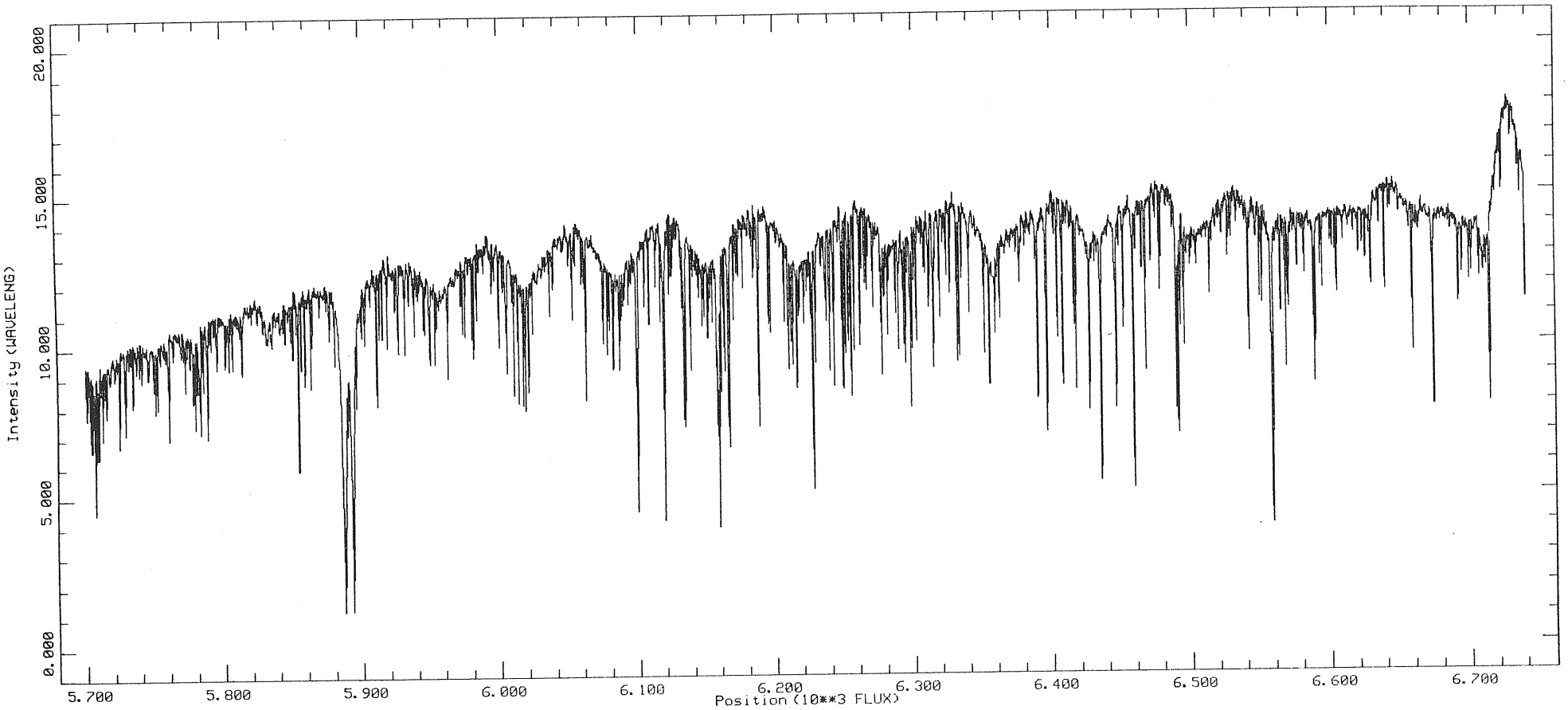

Fig. 3.14: Ripple effect in the spectral type standard star HD 137303. The star has been reduced using the standard method.

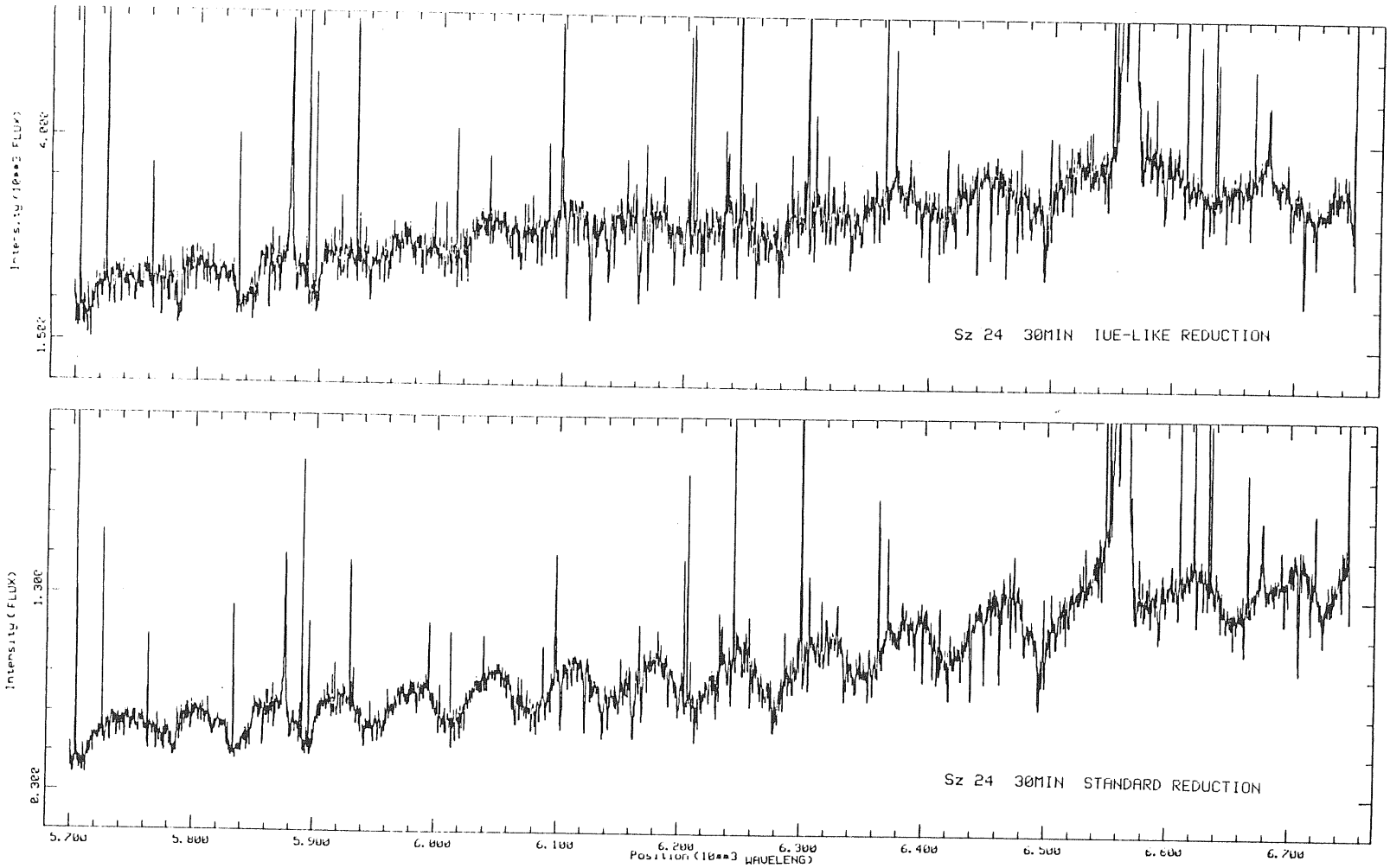

Fig. 3.15: A comparison between the IUE-like reduction and the standard reduction for the star Sz 24 (exposure time is $30min$)

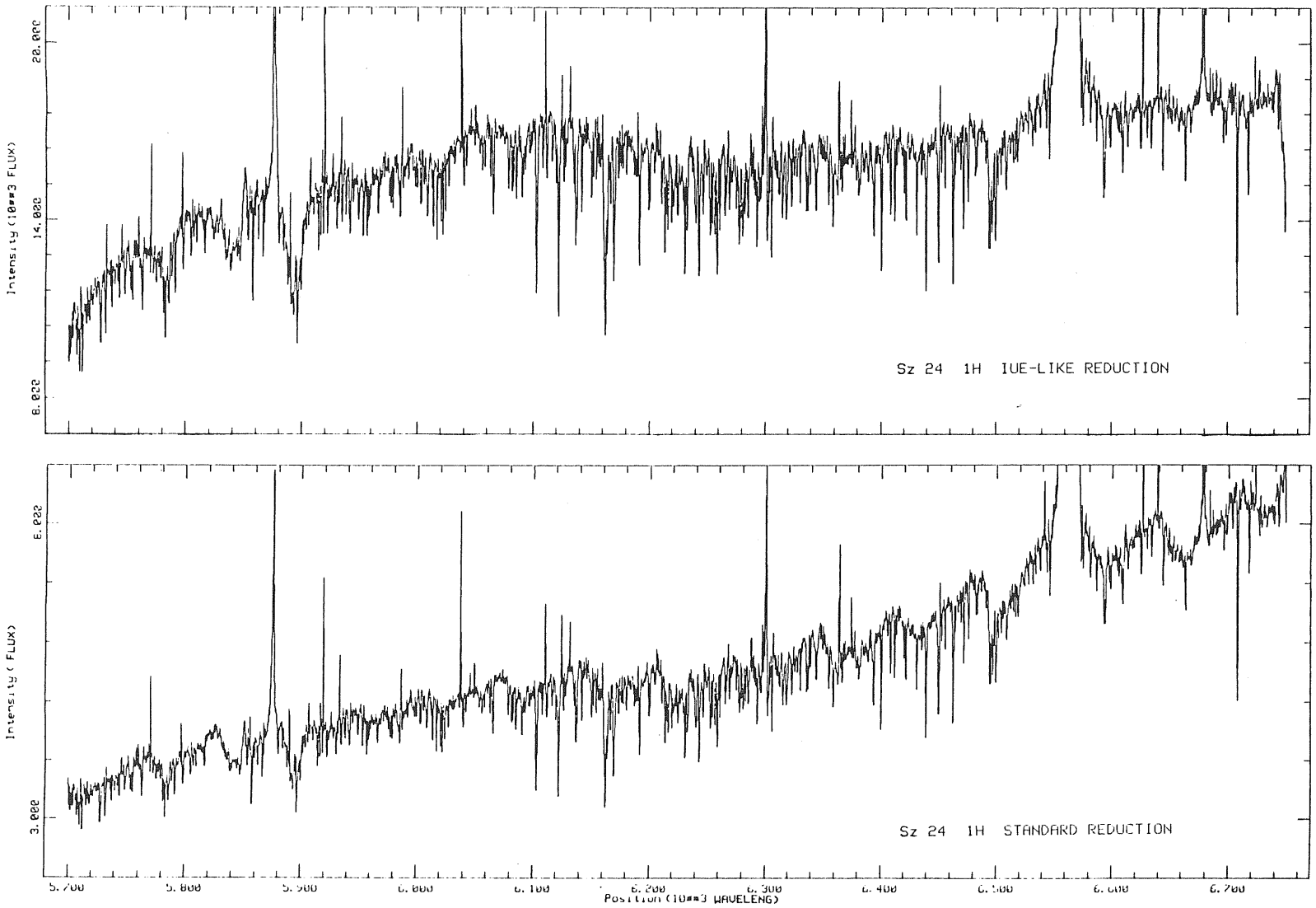

Fig. 3.16: A comparison between the IUE-like reduction and the standard reduction for the star Sz 24 (exposure time is 60 *min*).

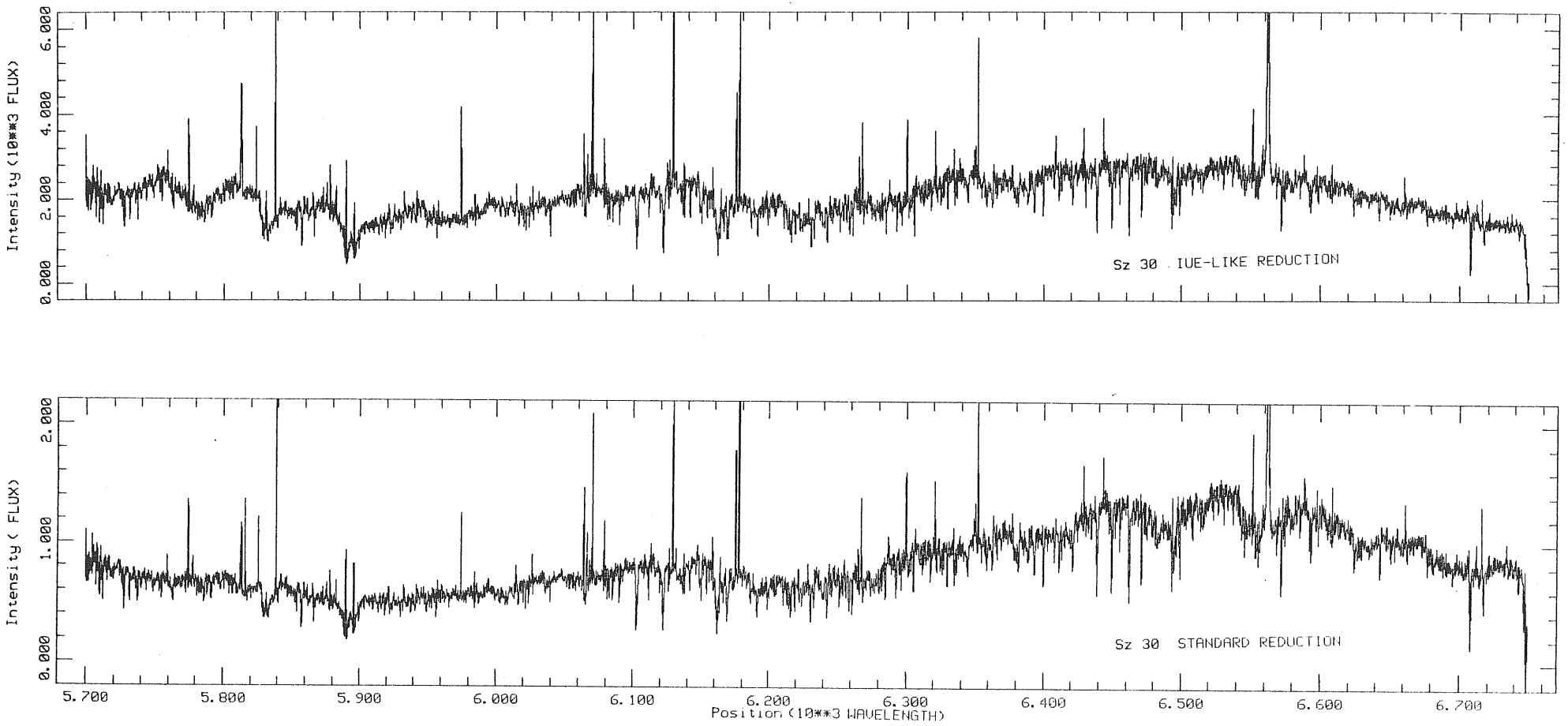

Fig. 3.17: A comparison between the IUE-like reduction and the standard reduction for the star Sz 30.

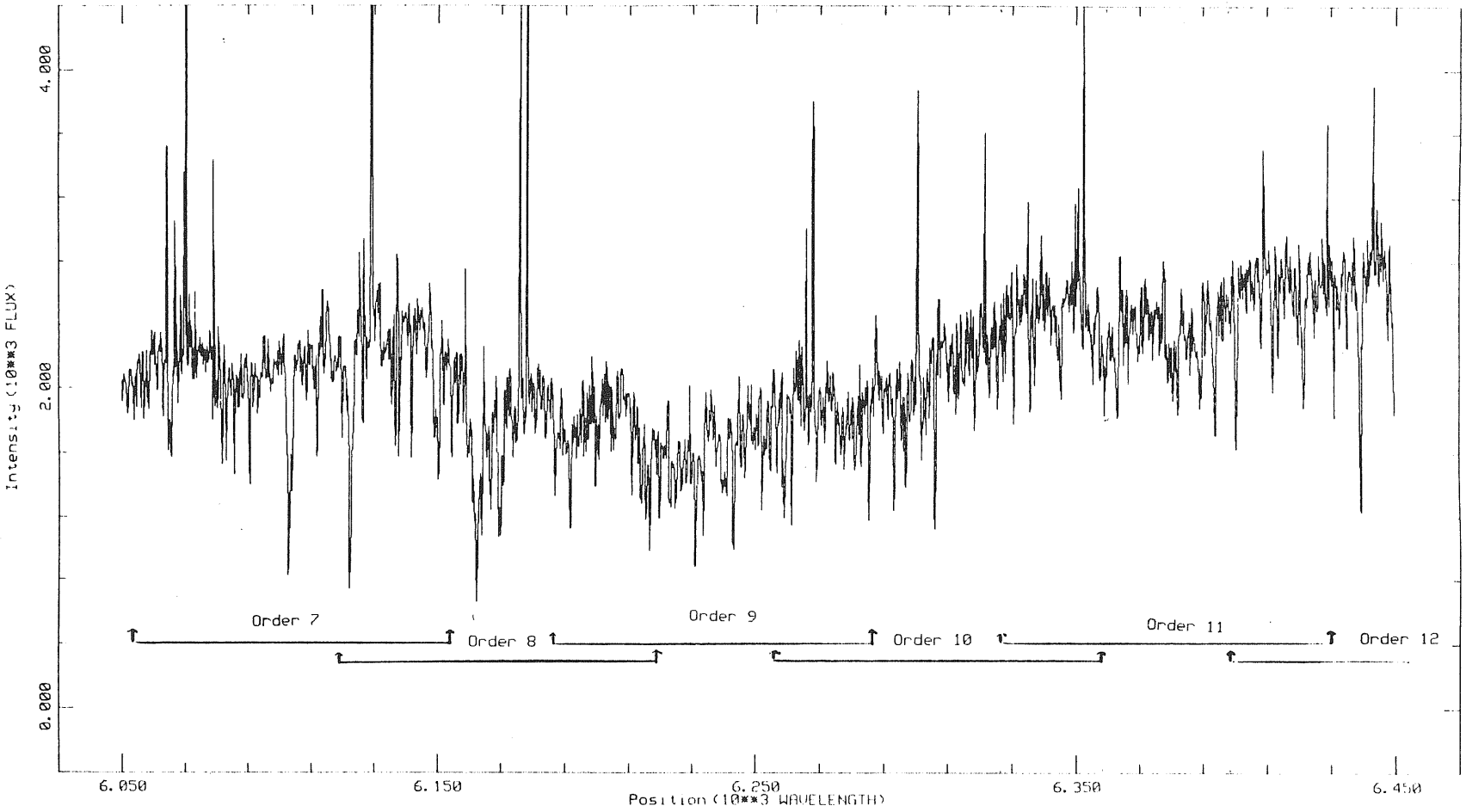

Fig. 3.18: A region of the TiO molecular band. It extends over about three orders.

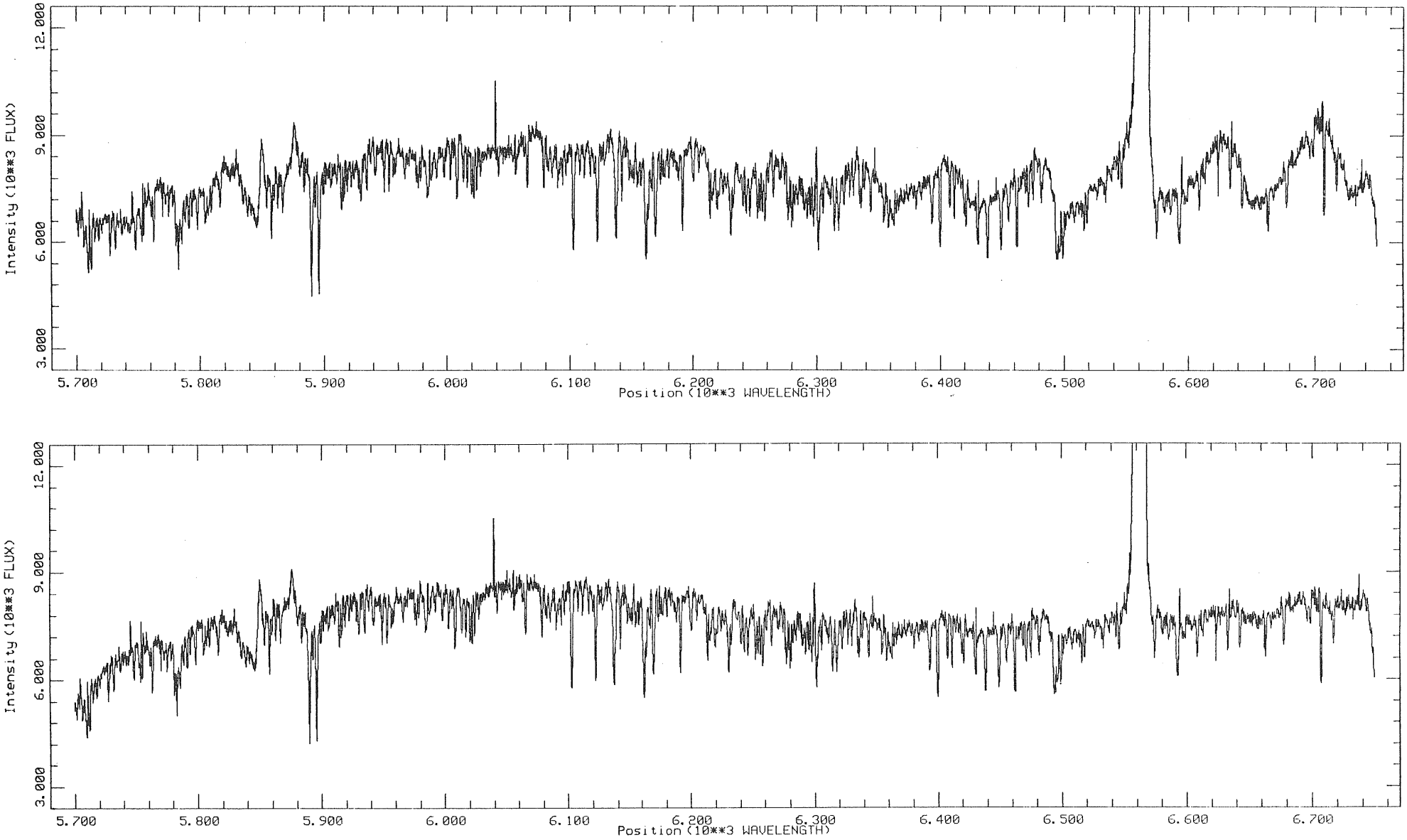

Fig. 3.19: A comparison between the two methods used for the blaze effect correction: the first method is a modification of the method suggested by Ahmad (1981); the second one is a modification of the method proposed by Barker (1984) (on the bottom).

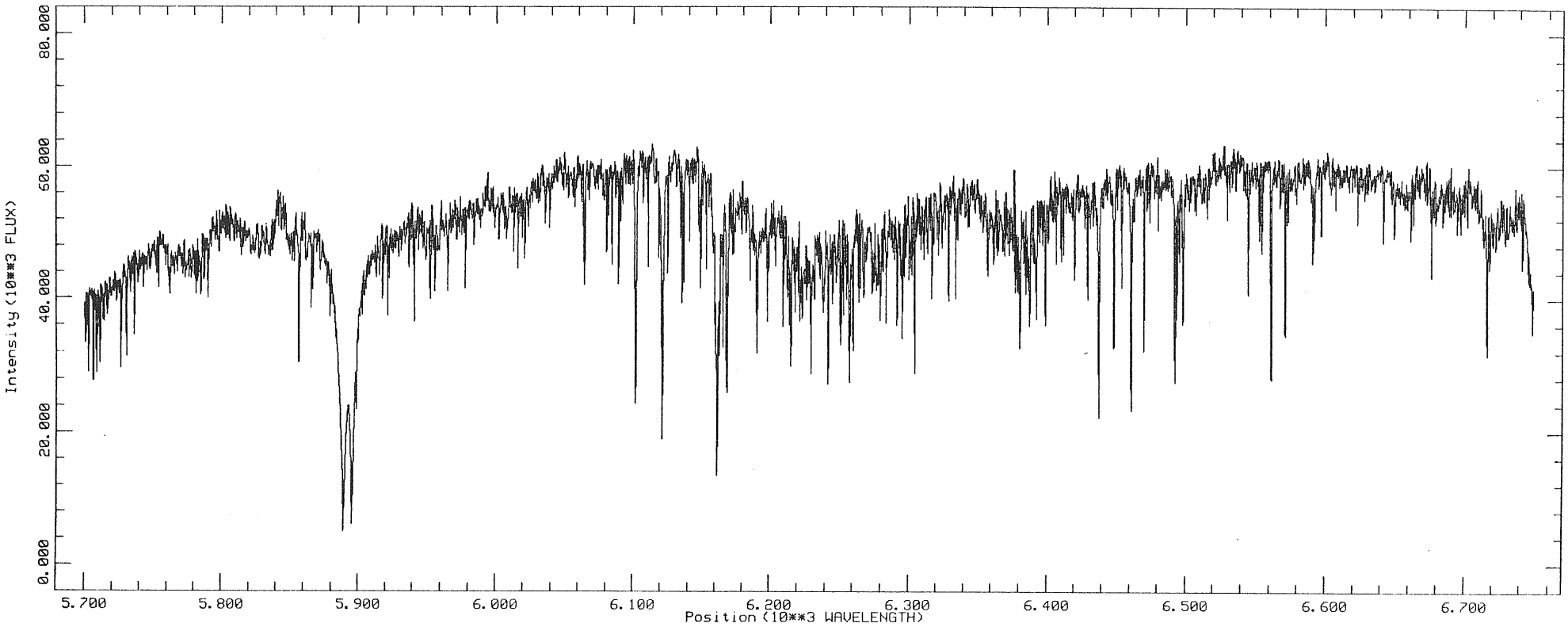

Fig. 3.20: A spectrum of the spectral type standard star HD 260655. His spectral type is M0 and the TiO molecular band is strong. The star has been reduced with the second method of the IUE-like procedure.

CHAPTER IV

Spectral Classification Criteria

§4.1 *Introduction*

In a previous work (Franchini *et al.*, 1988) we have determined the projected rotational velocities of the same sample of T Tauri stars that we are studying in this work. In order to understand the location of T Tauri stars in the Hertzsprung-Russel diagram in terms of theory of stellar evolution of pre-main sequence objects, one has to know the physical parameters that characterizes them; in particular the effective temperature and the luminosity. In this work we discuss the determination of the spectral types which are effective temperature indicators.

In this Chapter we will comment, on the basis of spectral characteristics of T Tauri stars previously described (Chapter II), the different criteria which are usually used in literature to determine the spectral type. In fact, we have seen that sometimes spectral classification of T Tauri stars could be very difficult due to the very strong activity which characterizes them. Then we will present the preliminary results obtained for our sample and the different criteria that we have used.

§ 4.2 *Spectra Types Classification*

Spectroscopically T Tauri stars have been classified as dwarfs G-M stars (e.g. Joy 1945 and 1949, Herbig 1962 and 1977, Herbig and Rao 1972, Cohen and Kuhi 1979 and references therein). Their surface temperatures are normally determinated by a quantitative analysis of the photospheric absorption spectra

or by a detailed comparison of the spectra with those of "stantard stars" of known photospheric temperature. We have discussed before how the comparison to a standard star could be misleading due to the "veiling" problem. The photospheric lines of the T Tauri stars can be weaker than those of the standard stars. We have also seen that the reasons of this behaviour is probably the presence of *deep photosphere* which produce a *weakenig* or desappearance of a absorption line if the line absorption coefficient *increases* with the temperature.

Consequently, for strong-emission T Tauri stars reliable effective temperatures can only be determinated from a model–atmosphere analysis which includes the chromospheric layers. A comparison with standard absorption spectra may be misleading.

In weak–emission T Tauri stars and PTTs the photospheric absorption spectra usually appear more normal. But, as has been known for many years, even in these cases a comparison with standard star spectra often results in contradicting effective temperature values when different criteria are used (Herbig, 1977; Walker, 1978, 1980). We have seen, for example, in the case of ROX 3 - a PMS star which show little chromospheric emission - the T_{eff} value results higher in the blue spectral range than in the red range. In the blue range Appenzeller (1985) uses the ground-state line of CaI and CrI and the FeI lines and some others criteria. In the red range he uses the TiO molecular bands. The presence of a very deep chromosphere produces the emission of CaI and CrI groundstate lines in the very extreme T Tauri stars; then in ROX 3 the same lines are in absorption but they are probably contaminated by chromospheric emission. Moreover, since these lines have high line coefficient absorption they are probably formed relatively high in the photosphere near the temperature minimum where the flat temperature gradient, weakens the absorption strength. For the weaker FeI lines we look deeper into the photosphere so that these effect are less pronounced.

The chromospheric effects mimic a higher effective temperature. In the red

range usually it is possible to use the TiO band (chromospheric TiO emission is very unlikely), so that the effective temperatures derived from this criterion are probably less affected by the dense chromosphere. However, higher optical depth of the temperature minimum will certainly influence the molecular bands as well. Therefore, a T Tauri star and a standard star of equal TiO band strength need not to have the same effective temperature, and neither the criteria used in the blue spectral range nor the TiO bands can be expected to provide a reliable effective temperature of T Tauri stars.

So we can point out that in "veiled" spectra the spectral type estimation can only be of approximate nature. But in spite of these difficulties the quoted spectral type should at least give a rough idea of the temperature of the photospheres of the observed stars. Moreover, their uncertainties and systematic errors may be less than available values computed by models and evolutionary tracks of PMS stars.

4.2.1 *First Rough Spectral Classification*

Some dwarf stars, spectral types ranging from G2 to M0 has been observed with the same equipment as that used for the Chamaeleon 1 and Chameaeleon 2 stars as spectral type standards. In Table 4.1 all the observed stars are reported: identification of the stars are given in columns 1 and 2; red magnitudes (m_r), taken from Schwartz (1977), are in column 3; columns 4 and 5 report respectively the published values of the luminosities and rotational velocities (Franchini *et al.*, 1988).

In Fig. 4.1(*a-d*) we have reported all the observed spectra of the Cha1 and Cha2 dark clouds and the standard stars in a relative scale: we have normalized all the the spectra to the continuum at the same wavelength ($\lambda \approx 5974\AA$) and then we have shifted the spectra in order to overplot them. All the spectra

have been reduced with the IUE–like method described in Chapter II. Only the star Sz 3 has been reduced with the standard method and in fact it is possible to observe the slope due to the normalization relative to the calibration standard star F 56. In Fig. 4.2 we have reported the spectra having spectral type ranging from G2 to M5 and luminosity class V (Jacoby *et al.*, 1984) to make a comparison.

We have used these spectra to determine some criteria for spectral classification on the basis of metallic lines ratio and/or molecular bands. In this choice we have taken into account all the considerations we have discussed in section 2.2.

From the spectra in Fig. 4.1*d* and Fig. 4.2 we can observe the effects of the different photospheric temperatures over the Na I D lines and the TiO molecular band ($\lambda = 6240\mathring{A}$) for instance.

Care is exercited in the use of the D Na I since some strong lines stars exibit sodium emission (Fig. 4.3). Stars in which TiO bands are seen offer the most secure classification.

A first rough estimation of the spectral type has been performed by eye by comparing the spectra of the T Tauri stars Fig. 4.2(*a*-*c*). In this way we have been able to put some lower or upper limit to the spectral type. These first results have been reported in column 2 of Table 4.2.

In this kind of estimation of spectral type we have essentially considered the presence and the strength of the TiO band and the strength emission lines as indicator of veiling.

Taking into account our standard star spectra and those of Jacoby *et al.*'s (1984) library we can see that only for stars cooler than K4 it is possible to observe and then to use the TiO band. For the stars hotter than K4 this band disappear and we have to consider other criteria . Maybe, the Na I D lines could

be a good criteria for the K stars if no emission are present.

In our opinion, the standard star HDE 260655 (M0) seems hotter then the standard star HD 121271 (K7). This appears at first glance by comparing the two spectra. The TiO band and the NaI D lines are stronger and wider in HD 121271 (K7) star than in HDE 260655 (M0). This is confirmed also by all other quantitative criteria used for the spectral classification (see below). We would like remember that the standard star HDE 260655 has been classified as M0 V by Jacoby *et al.* (1984) while the star HD 121217 is reported to be K7 V by Buscombe's (1981) and has been classified as K5/M0 V by Houk (1978,1982). In this preliminary study we have considered as M0 V the star HD 121217 and we have neglected, for the moment the star HDE 260655. We intend to check the spectral type of the two stars with more accuracy.

By comparing columns 2 of Table 4.2 with Table 4.3, we see that, even if we cannot give a precise estimation of the spectral types, our results are not in contrast with those available from literature. The only consistent difference is the star Sz 9 which is classified M0 by Appenzeller *et al.* (1983) while it should not be cooler than K4. In fact we do not observe a strong TiO molecular band as for M0 stars and the star does not seem to be characterized by intense activity (see Fig. 4.1*a*). Moreover, even if the TiO is affected by veiling, this one generally is not so strong to produce a difference of about five spectral classes.

It is evident that this kind of identification is only qualitative and that it is necessary to calibrate the bands heads against spectral types using monochromatic ratios of flux at the band head to adjacent continuum.

4.2.2 *Spectral Type Criteria*

At the moment we have performed only preliminary studies and we have used the following criteria to identify the spectral type:

i) NaI D strength: only for the stars where the photospheric spectrum is well defined and no emission are present. Usually this method could be usuful for the G–K stars. We have measured the equivalent width for the two lines D_1 and D_2 for all the standard stars available . Then we have fitted these point and used this relationship to obtain for the T Tauri stars the spectral type given the equivalent width of the NaI D lines (Fig 4.4). In Table 4.4 we have reported the equivalent width of the NaI D lines ($EW(D_1)$ and $EW(D_2)$) for the standard stars. It is possible to observe that for the star HD 121271 the equivalent widths are greater than for the star HD 260655. This conferm our suspicion about the spectral classification of these two stars.

ii) FeI(5778.5Å)/VI(5776.7Å): By using the "Photometric Atlas of the Solar Spectrum" (Minnaert *et al.*, 1940), the "Photometric Atlas of the Spectrum of Arcturus" (Griffin,1968) and the tables of the "Solar Spectrum 2935Å to 9770Å" (Moore *et al.*, 1966) we have looked for a number of absorption lines, which are particularly sensitive to the effective temperature and are free from blend and not affected by near emission.

We have observed the behaviour of the FeI(5778Å) and VI(5777Å) for the Sun G2 V and Arcturus K2 5: from Fig. 4.5 we can observe the ratio of these lines decreases by decreasing the effective temperature. So we have measured the equivalent widths for the two lines (where both where measurable: Table 4.5) and we have constructed the plot of Fig. 4.6. Since we have only five standard stars and for two of them it was not possible to measure the equivalent width of VI, we have used the equivalent width of Sun and Arctur.

It is correct remember that this criterion should not be used for the stars affected by strong activity: due to veiling, different lines could show differential chromospheric filling-up of their absorption cores. This is confirmed with the fact that the spectral type obtained using this criterion is essentially in agreement with the spectral type obtained using the previous criteria if the stars are not

affected by veiling (see Table 4.2). The worst agreement is obtained when the star is strongly veiled: in Table 4.2 we have reported all our results even when the star is characterized by strong activity.

iii) CaI 6162*Å:* This criterion is generally good to identify the G2–K0 stars but not cooler stars because of the blend due to the fact the TiO molecular band becomes stronger as one goes to cooler spectral types. Anyway we have measured the equivalent width by integrating the profile of the line between the same profile extremes in order to take into account equally blend effects.

Concerning the agreement of the results with the previuos one, we note that the worst is for Sz 30, due both to the fact that it is not suitable for cool stars and to the presence of strong "veiling".

4.2.3 *Effective Temperature by the Curve of Growth*

As last method to estimate the spectral type we have used the curve of growth analysis of the FeI lines. This methods, allows to derive the effective temperature (needed to locate the star in H–R diagram and discuss the star energy distribution) and then to convert effective temperature to spectral classification by using appropriate temperature scales for luminosity class V (Cohen and Kuhi 1979) (See Table 4.6). In this way it is implicitily assumed that this conversion from spectral type to effective temperature (or viceversa) can be made even though it is likely that a T Tauri star is not a normal star.

However, this procedure should result in a temperature scale that should be the most accurate system available until better model atmospheres are calculated. We note that it is not clear what T_{eff} should mean in a star with different emitting regions, each carrying significant amounts of flux, e.g, photosphere, chromosphere, extended atmosphere, circumstellar dust (see section 2.2.3). The formal definition of T_{eff} requires the bolometric definition and the

radius. Even with an estimate of L_{bol} it is uncertain which value of radius R to use in the calculation of T_{eff}. The answer requires a physically consistent model for the emitting regions.

The equivalent widths of a number of FeI lines were used to derive a curve of growth for each program star. We divided the iron lines into groups, according to their excitation potential, and searched for the excitation temperature capable of bringing all the groups to the same curve of growth (see Gray 1976, p339). The effective temperature was then obtained by assuming the same ratio between excitation and effective temperature that holds for the Sun. Column 6 in Table 4.2 report the spectral types obtained in such a method after a conversion of the derived effective temperature into spectral type according to Table 4.6 (Cohen and Kuhi, 1979).

As we have commented for the FeI/VI criterion, this criterion could not be suitable for T Tauri stars affected by "veiling". In fact we can observe that the best agreement is obtained for the stars Sz 6, Sz 9, Sz 19 and Sz 41 which do not show veiling effect and strong activity.

Table 4.1: The stars in study

Sz No.	Other designations (1)	m_r	Log($L/L_\odot$)(2)	vsini km/s
Chamaeleon 1				
3	HM 2, SY Cha	12.5	-0.14 b	17
5	HM 3, TW Cha	12.5	-0.16 b	15
6	HM 4, LH$_\alpha$ 332-20	10.9	0.58 b	37
9	HM 7	11.2	0.10 a	16
17		13.6		16
19	HM 13, CD-76 486	10.0	1.14 b	32
24	HM 17, VW Cha	11.8	0.40 a	26
30		12.6		<15
34	HM 24, WW Cha	12.1	0.71 a	56
36	HM 26, WY Cha	13.0	-0.13 a	16
41		11.2		31
Chamaeleon 2				
51	BC Cha, Ho S6428	13.7		<15
54	BF Cha, Ho S6437	12.5		47
59	BK Cha, Ho S6443	14.3		23
61	BM Cha, Ho S6445	14.4		23

(1) HM = Henize and Mendoza (1973); Ho = Hoffmeister (1962); LH$_\alpha$ = Henize (1954)
(2) Luminosities are from (a) Appenzeller et al. (1983) and (b) Bouvier et al. (1986)

Table 4.2 Spectral Type Classification

Sz	First class.	Na	FeI/VI	CaI(TiO)	Curve of growth	Activity
3	M0		K7	K6-K7	K3	very strong
5	K7		K3	K7	K1	weak
6	K0-K4	K2		K1	K0	
9	K4	K3	K3	K4-K5	K3	
17	M0		K4-K5	K2-K9	K0	weak
19	G2-G6			G2-G4	G0	
24	K2-K4		K2	K2	G9	strong
30	$\geq$M0			K3	K6-K7	very strong
34	~K4			G4-G5	G0	strong
36	K4-K6		K8	K7	G6	weak
41	K2-K4	K2	K0	K3	K0	
51	K7		K7	K8	K3	weak
54	~K0	K0-K1		K1-K2	G6	weak
59	K7-M0			K1	K1-G9	strong
61	<K4 ?			G5 ??	K1-K2	very strong

Table 4.3 Spectral Type Classification

Sz	Appenzeller (1977)	Appenzeller (1979)	Appenzeller et al. (1983)
3	K2 V	K2 V	M0:
5	K0:	K0:	M0:
6	K0		K2
9	K2 V		M0
17			
19	G2 V		G2
24	G1 V	G1 V	K2
30			
34	GK		K5:
36	K2		M0
41			
51			
54			
59			
61			

Table 4.4

Standard Stars	$EW(D_1)$ Amstrong	$EW(D_2)$ Amstrong
HD 70854 G2 V	0.7	0.55
HD 97841 G6 V	1.3	0.96
HD 130042 K0 V	1.7	1.19
HD 137303 K4 V	4.0	2.7
HD 260655 K5/M0 V	8.6	5.4
HD 121271 M0 V	6.2	4.9

Table 4.5

Star	EW(VI)	EW(FeI)	log(FeI/VI)
Sun	0.0015	0.016	1.03
HD 70854		0.016	
HD 97841		0.96	
HD 130042	0.013	0.028	0.33
Arcturus	0.05	0.07	0.15
HD 137303	0.022	0.026	0.07
HD 260655	0.054	0.047	-0.06

Table 4.6

EFFECTIVE TEMPERATURE SCALE ADOPTED FOR YOUNG STARS

Spectral Type	log T	Spectral Type	log T
O9.5	4.519	G5	3.753
B0	4.490	G8	3.736
B0.5	4.418	K0	3.719
B1	4.354	K1	3.708
B2	4.312	K2	3.695
B3	4.253	K3	3.679
B5	4.140	K4	3.661
B6	4.111	K5	3.643
B7	4.086	K6	3.623
B8	4.053	K7	3.602
B9	4.025	K7–M0	3.598
A0	3.993	M0	3.593
A2	3.960	M0.5	3.580
A3	3.938	M1	3.566
A5	3.917	M1.5	3.555
A6	3.907	M2	3.544
A7	3.897	M2.5	3.535
F0	3.847	M3	3.526
F2	3.826	M3.5	3.518
F5	3.806	M4	3.509
F8	3.778	M5	3.494
G0	3.771	M5.5	3.483
G1	3.766	M6	3.471
G2	3.761		

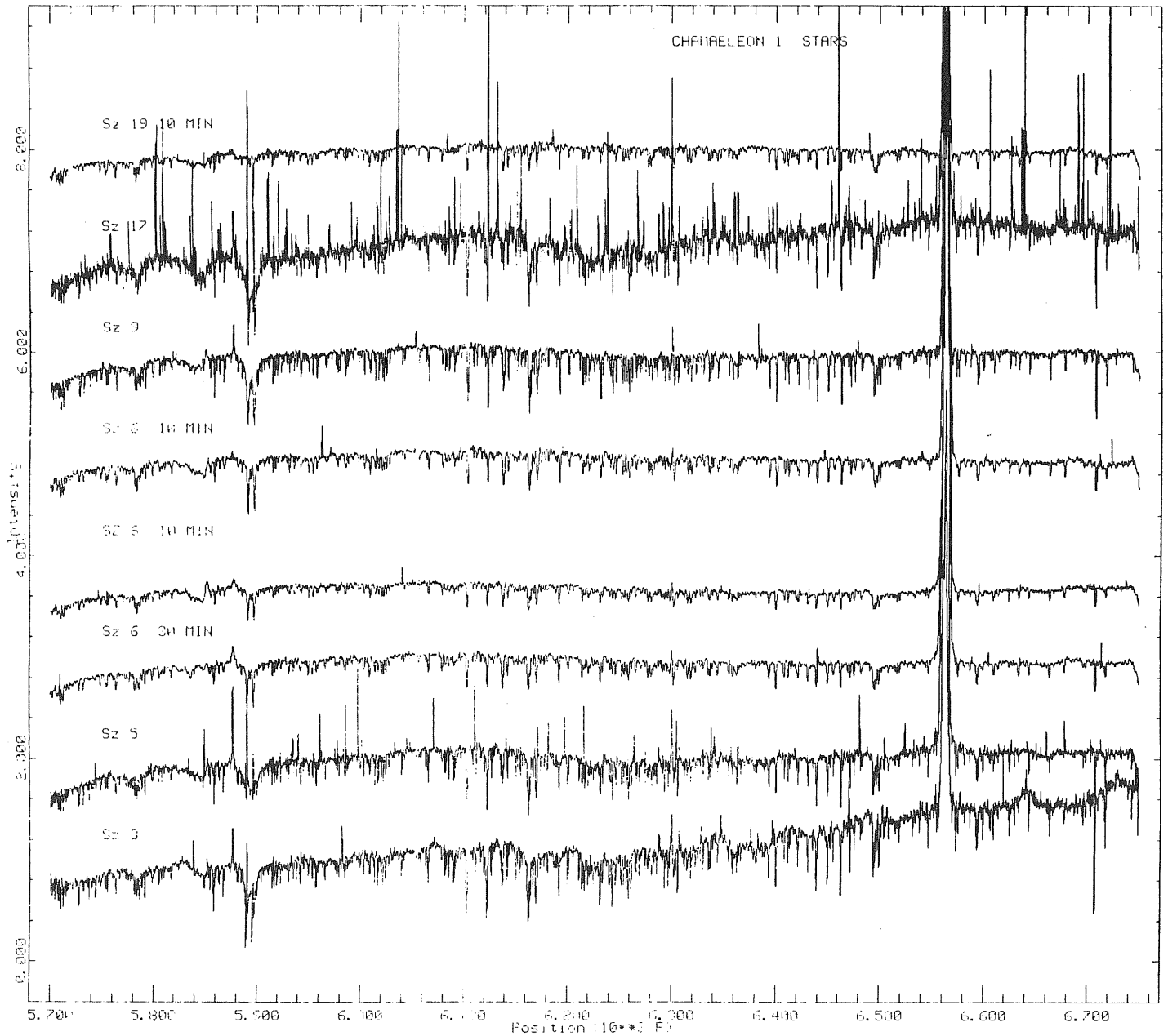
CHAMAELEON 1 STARS
Sz 19 10 MIN
Sz 17
Sz 9
Sz 8 10 MIN
Sz 6 10 MIN
Sz 6 30 MIN
Sz 5
Sz 3
8.200
6.800
4.000
3.300
0.200
Intens.+c
5.700
5.800
5.900
6.000
6.100
6.200
6.300
6.400
6.500
6.600
6.700
Position (10**3 A)

Fig. 4.1*a*

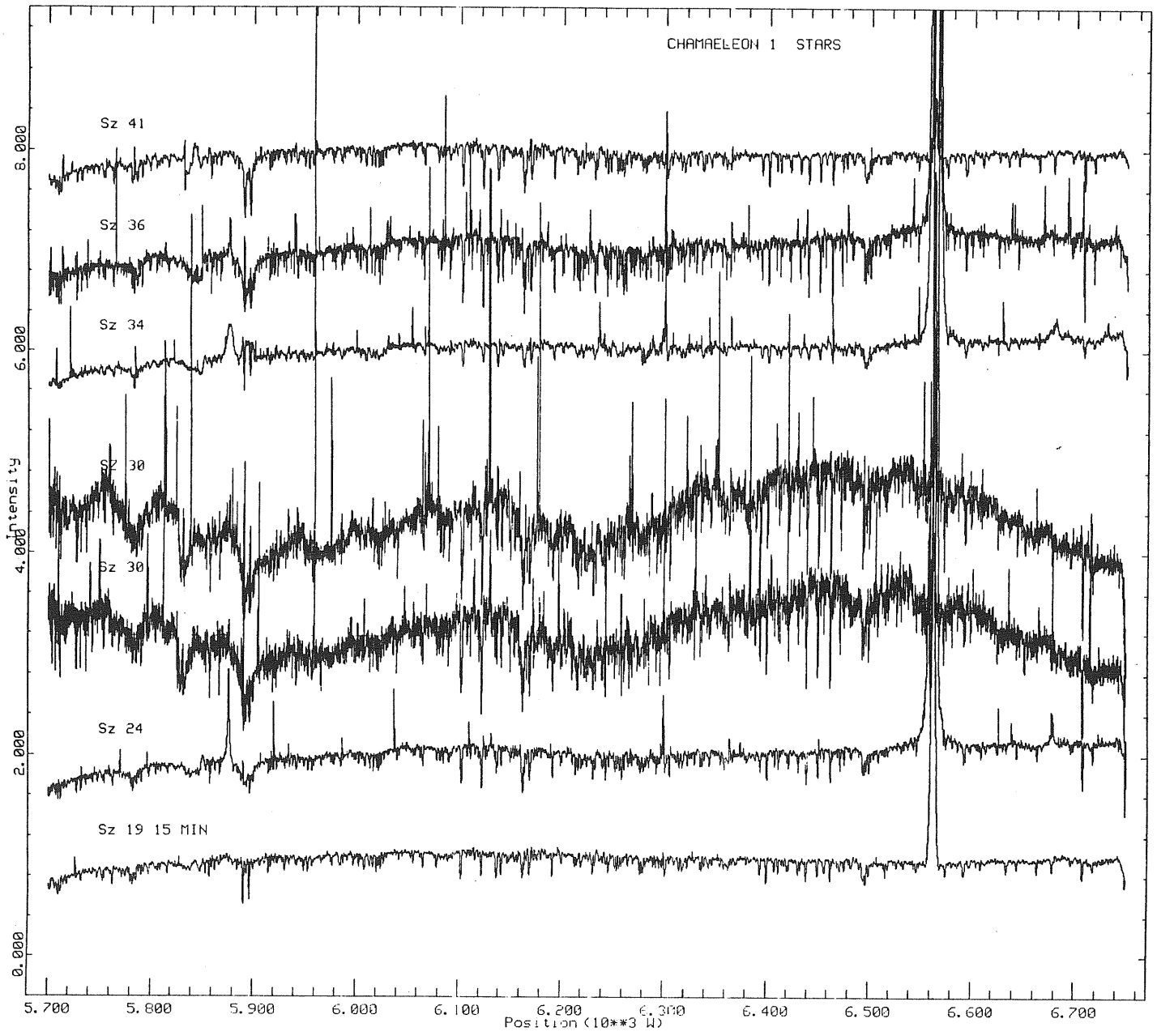
CHAMAELEON 1 STARS
Sz 41
Sz 36
Sz 34
Sz 30
Sz 30
Sz 24
Sz 19 15 MIN
Intensity
8.000
6.000
4.000
2.000
0.000
5.700
5.800
5.900
6.000
6.100
6.200
6.300
6.400
6.500
6.600
6.700
Position (10**3 W)

Fig. 4.1*b*

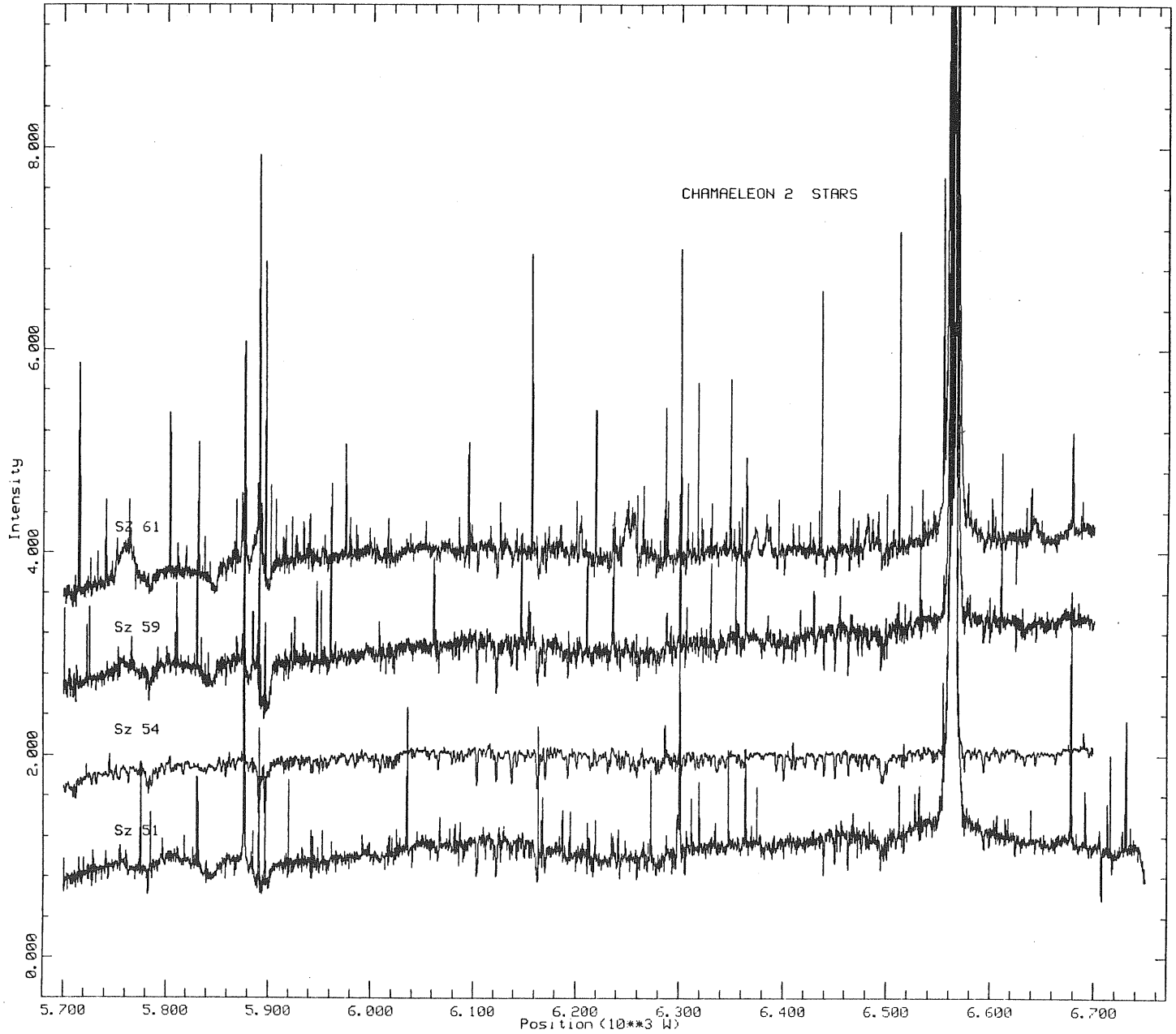
CHAMAELEON 2 STARS
Sz 61
Sz 59
Sz 54
Sz 51
Intensity
0.000
2.000
4.000
6.000
8.000
5.700
5.800
5.900
6.000
6.100
6.200
6.300
6.400
6.500
6.600
6.700
Position (10**3 W)

Fig. 4.1c

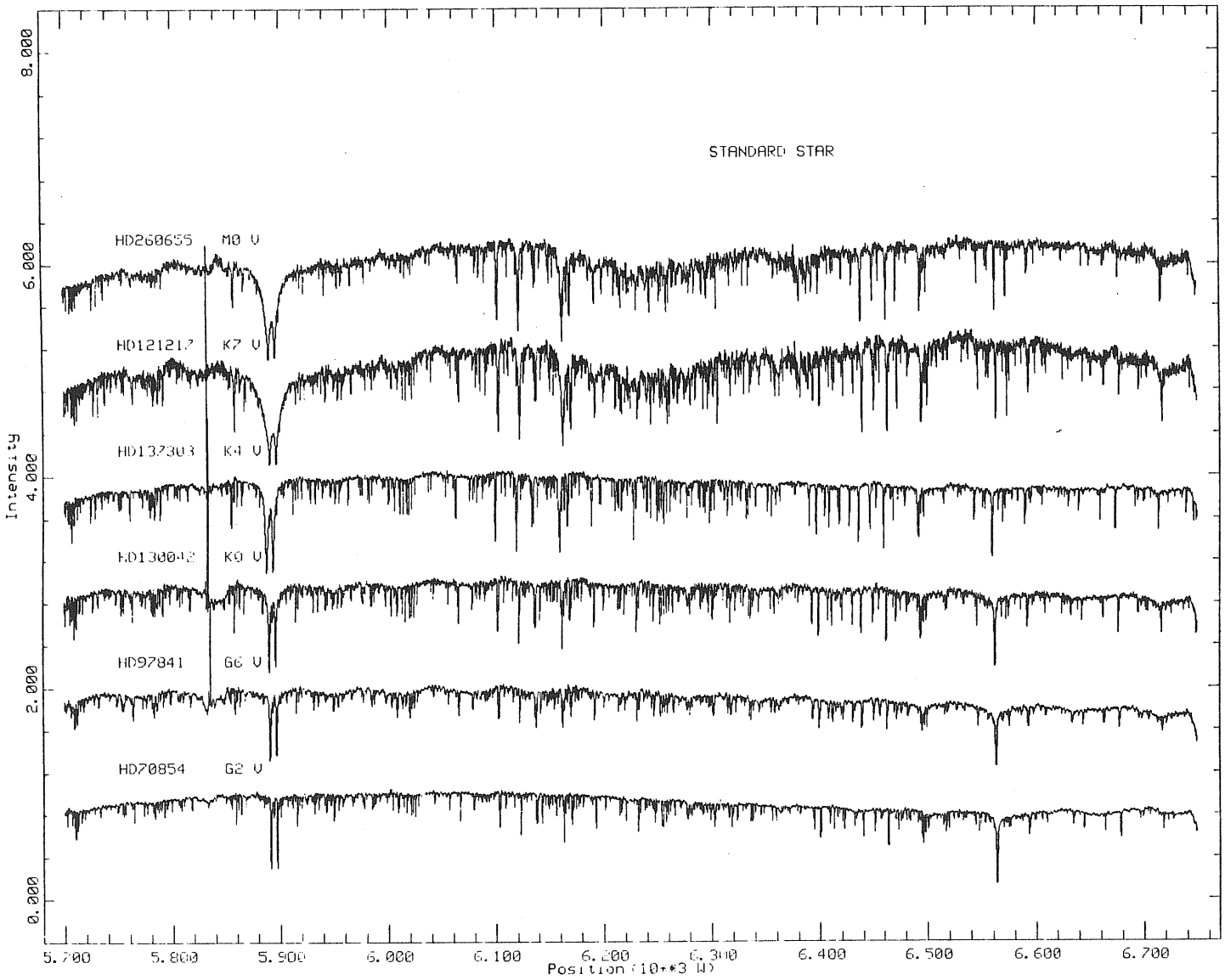
STANDARD STAR
HD260655 M0 V
HD121217 K7 V
HD137303 K4 V
HD130948 K0 V
HD97841 G6 V
HD70854 G2 V
Intensity
8.000
6.000
4.000
2.000
0.000
5.700
5.800
5.900
6.000
6.100
6.200
6.300
6.400
6.500
6.600
6.700
Position (10**3 A)

Fig. 4.1*d*

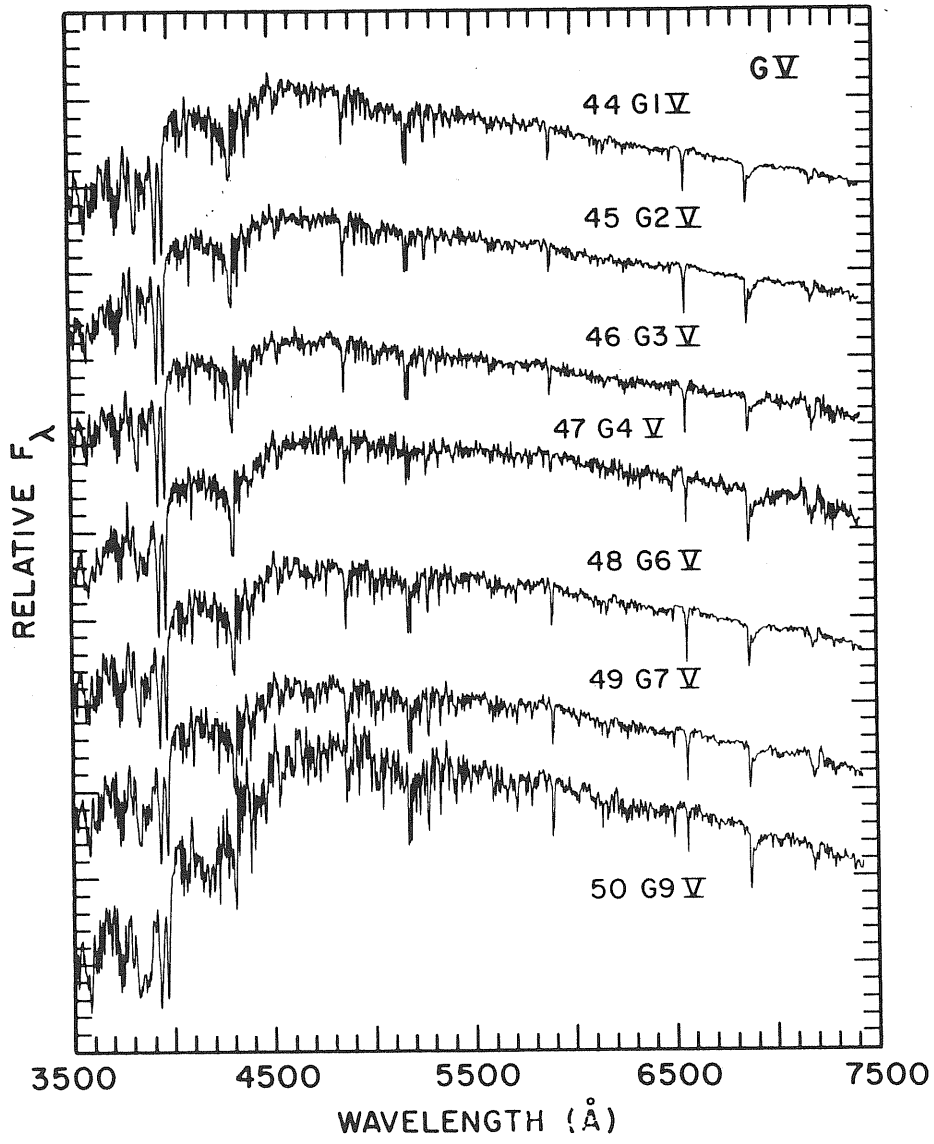

Fig. 4.2*a*: Jacoby *et al.*, (1984).

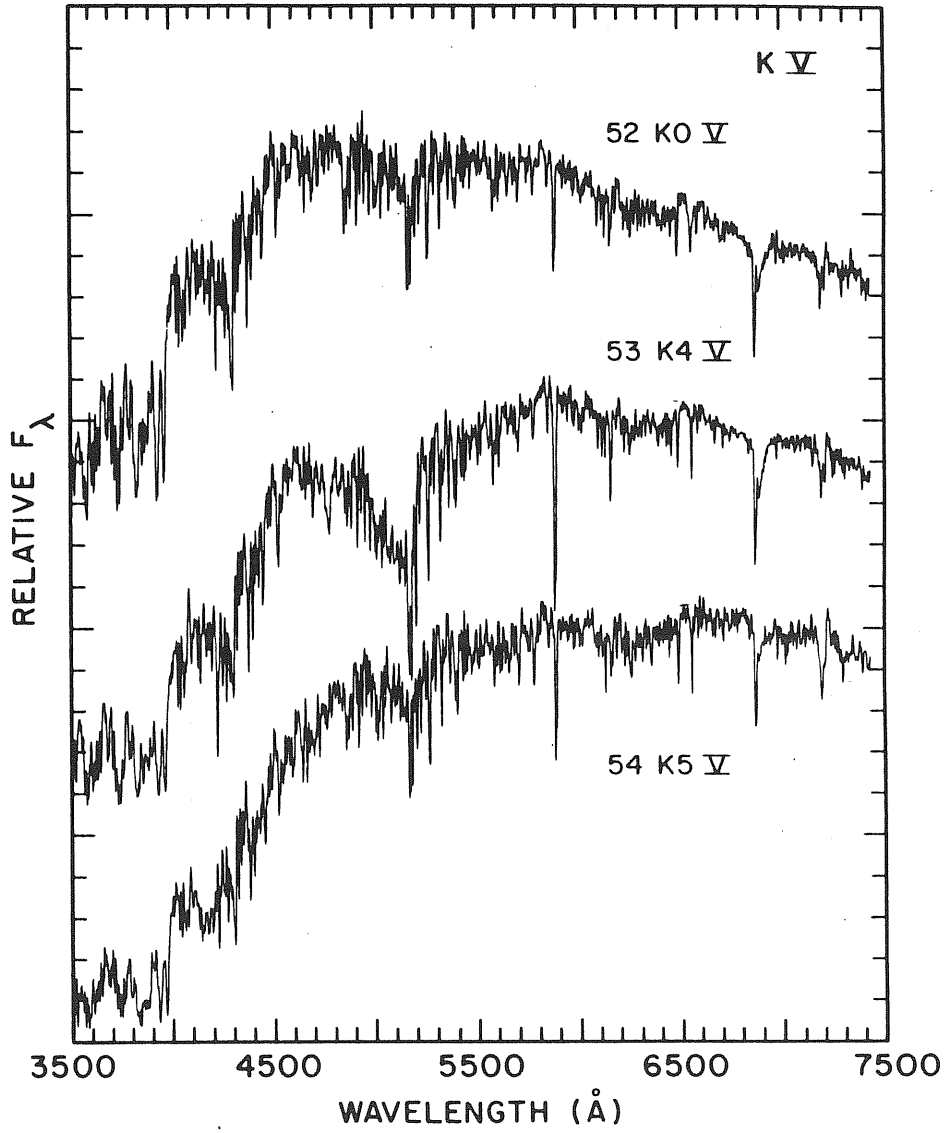

Fig. 4.2*b*: Jacoby *et al.*, (1984).

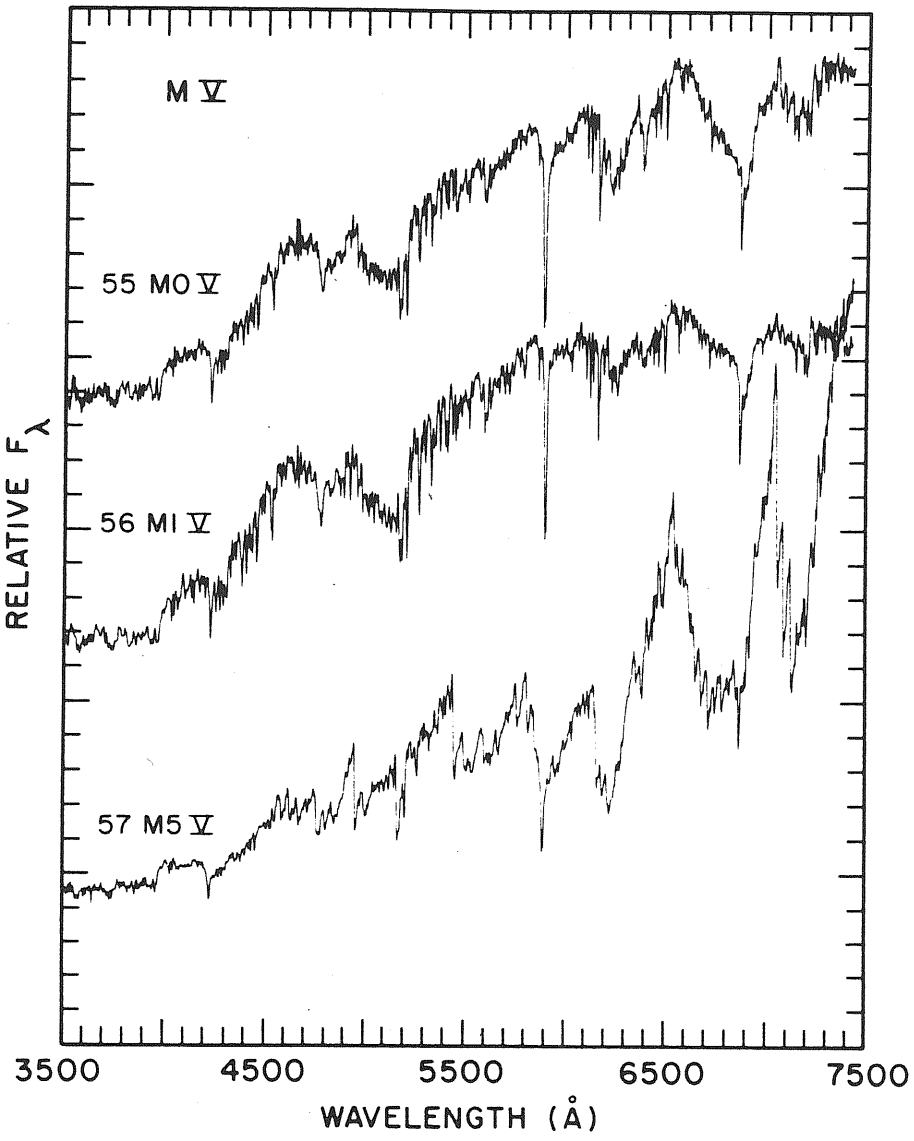

Fig. 4.2*c*: Jacoby *et al.*, (1984).

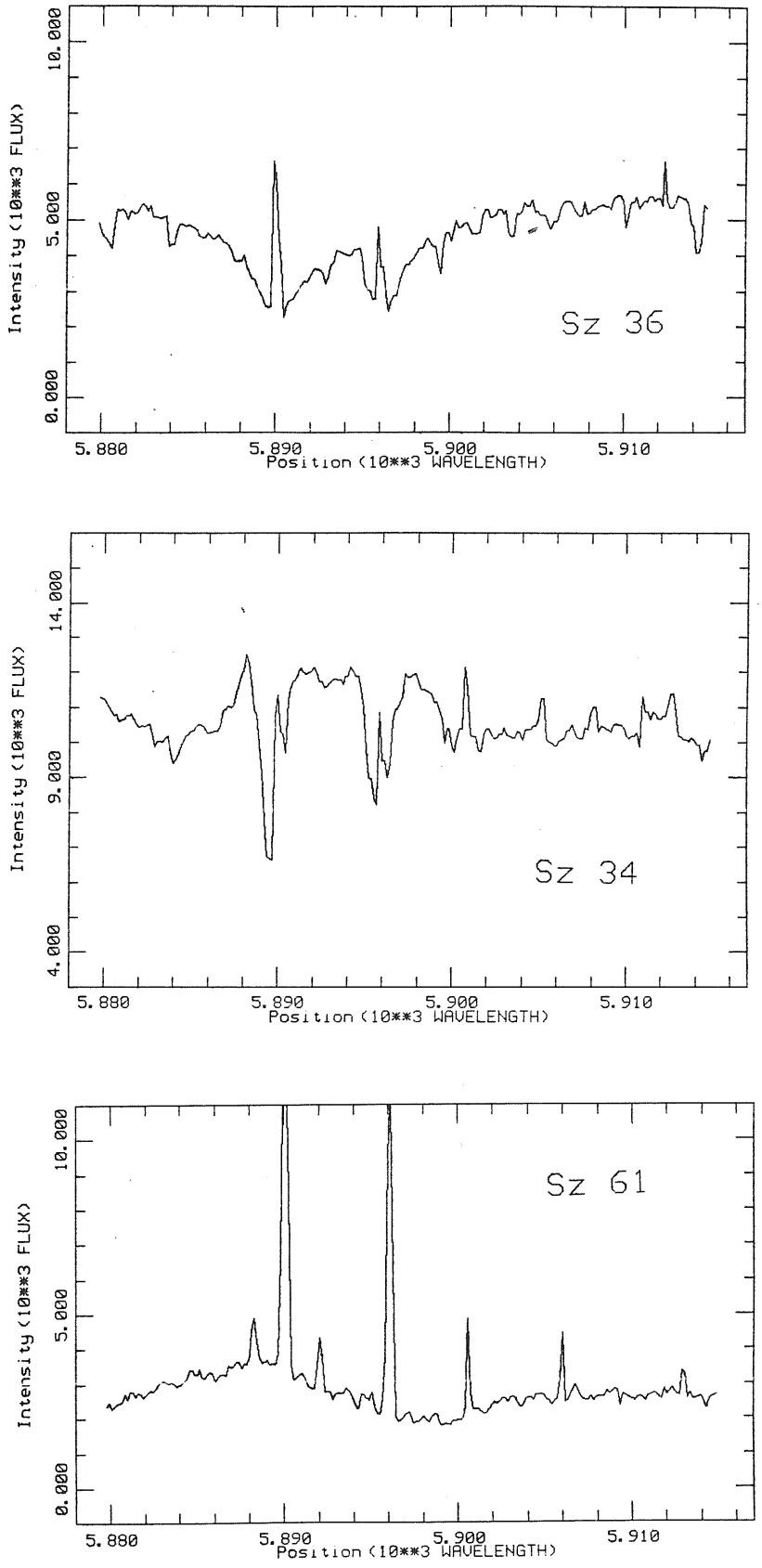

Fig. 4.3: NaI D line profiles.

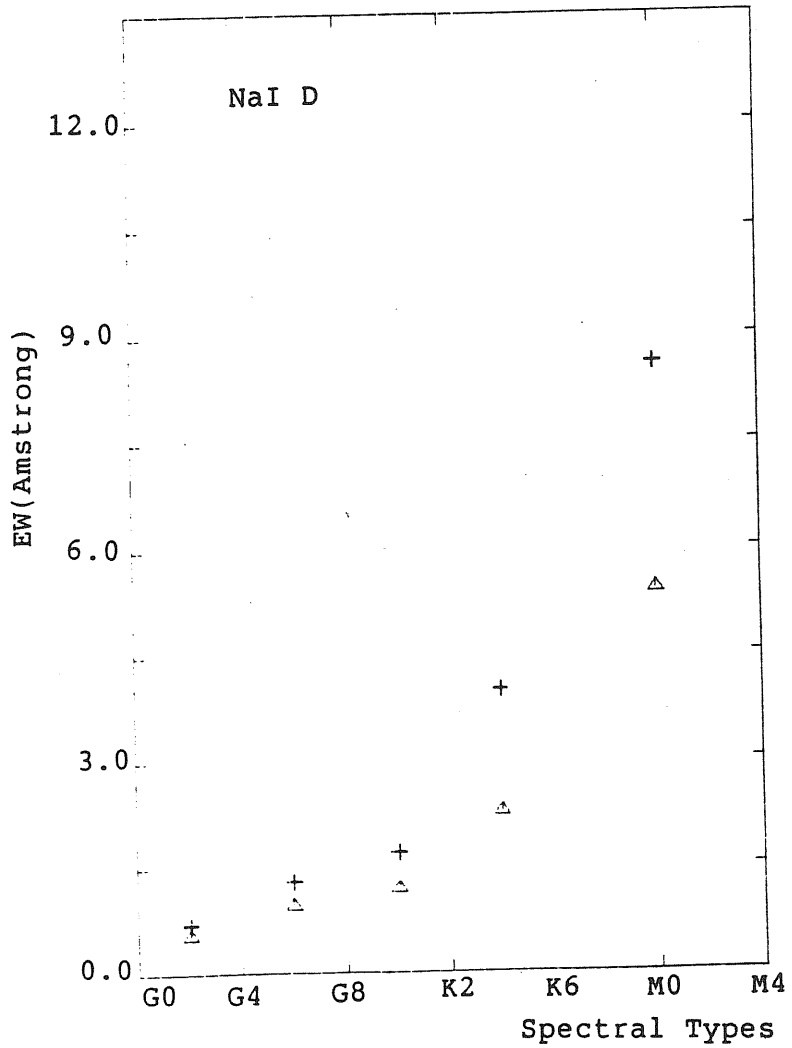

Fig. 4.4: Equivalent widths for the two lines D_1 and D_2 for all the standard stars available vs. spectral types. The equivalent widths $EW(D_1)$ are indicated by crosses $(+)$ while the equivalent widths $EW(D_2)$ are indicated by triangles $(\triangle)$.

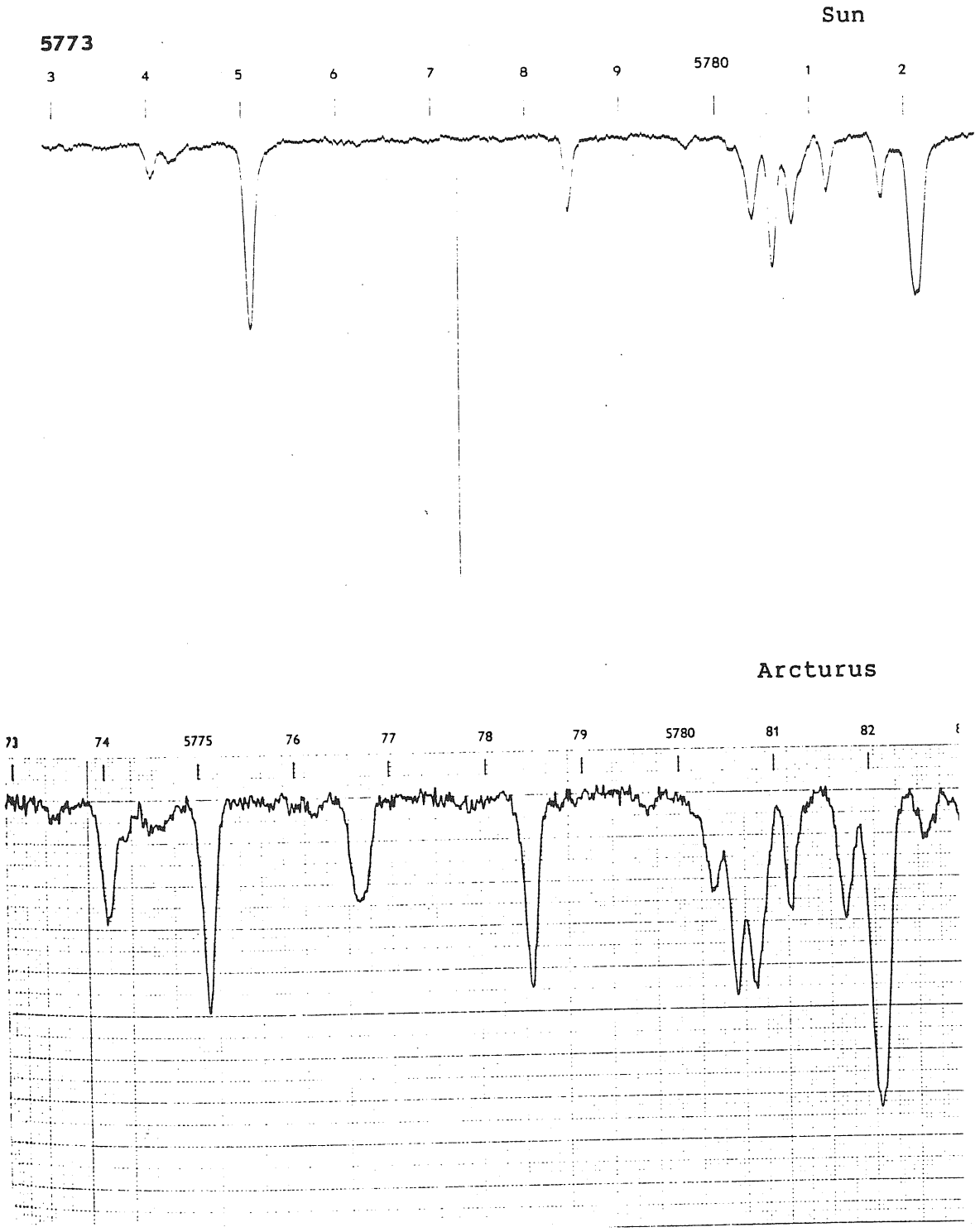

Fig. 4.5: FeI(5778) and VI(5778) for the Sun and Arcturus. We can observe that the ratio of these lines decreases by decreasing the effective temperature.

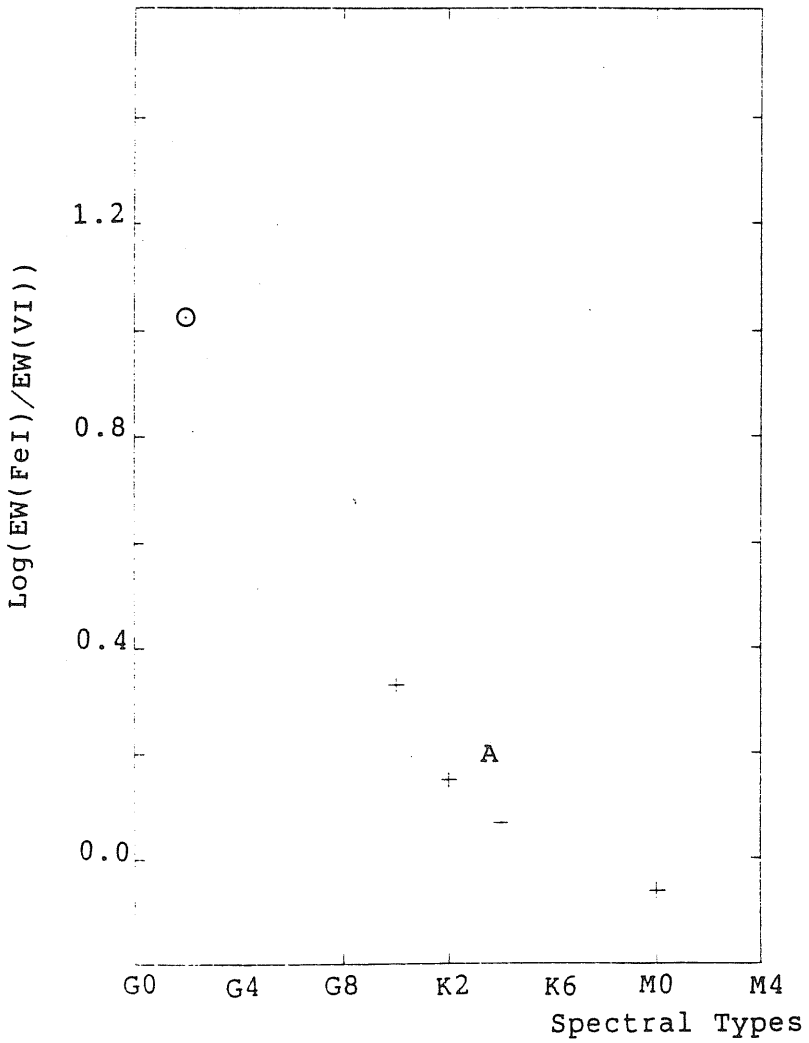

Fig. 4.6: $\log FeI/VI$ vs. spectral types for the standard stars. We have included the Sun and Arcturus indicated by A.

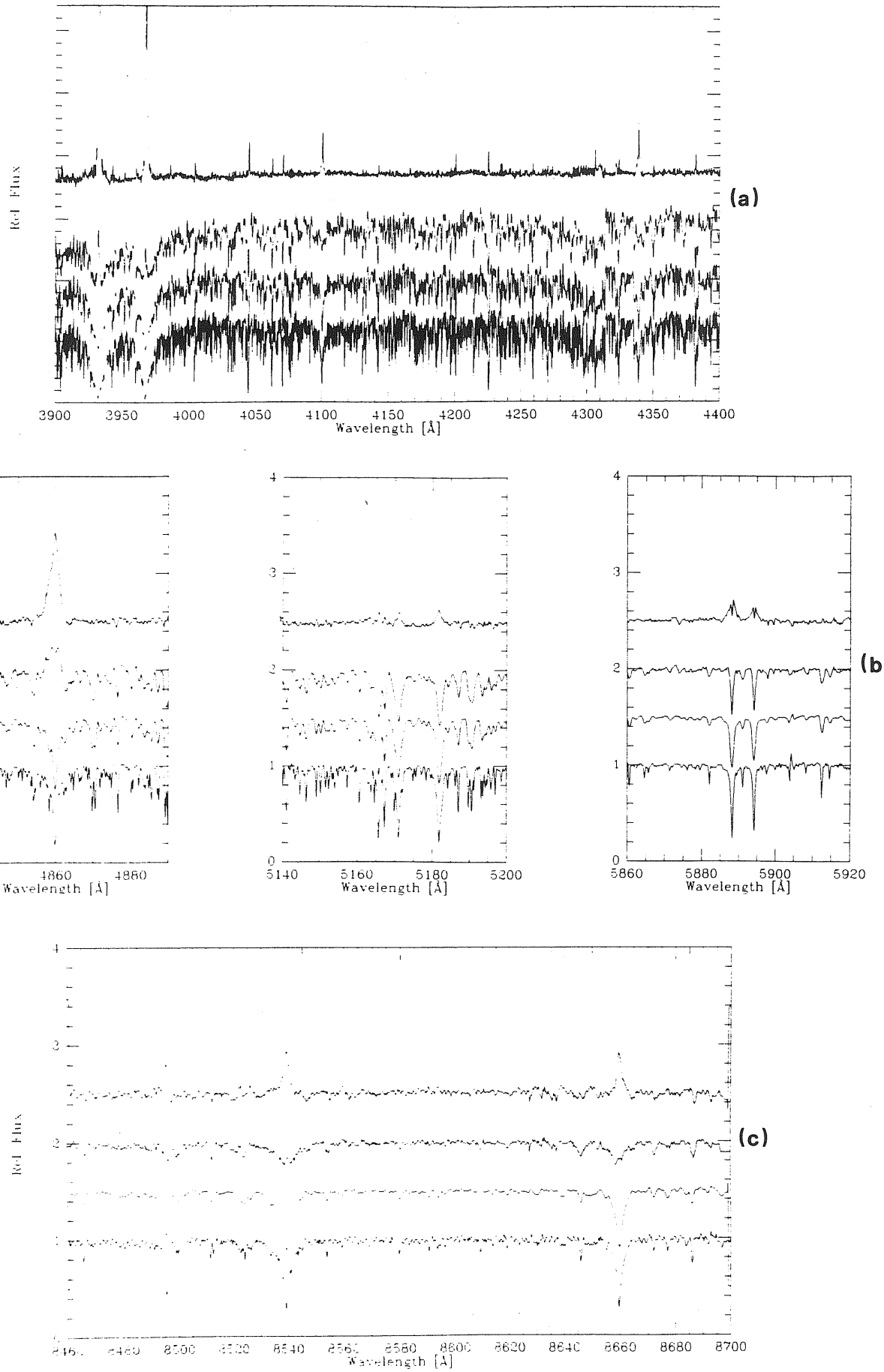

Fig. 4.7: Illustration of excessive emission of Sz 19 in the UV (a); at H_β, MgI B, and NaI D (b); and at the IR triplet (c). The figures give (from bottom to top) a spectroscopic standard (1); the standard convolved with a rotational finction of $v \star \sin i = 30 km/s$ (2); Sz 19 (3); and the ratio (3):(2). Note that the two residual components of the NaI D obey a flux ratio of 2.0, and indicate the presence of an interstellar absorption feature, too (Finkenzeller and Basri, 1985).

Conclusions and Future Work

The results of this preliminary work have been reported in Table 4.2. We have seen how spectral lines are unreliable indicators of spectral type for PMS stars with T Tauri emission characteristics. Strong absorption lines, which tend to have cores that form high in the stellar atmosphere, are sometime weak or "filled in", while neighboring lines of photospheric origin are normal in strenght. This is generally interpreted as evidence for the presence of a chromospheric temperature rising in T Tauri stars. The net effect is too weaken the stronger lines, making G and K stars appear of earlier in spectral type than would be indicated by the continuum. The lines remain narrow as their equivalent width are reducted by the superposed continuum emission. M stars, on the other hand, would still be recognizible as such because of the presence of molecular bands, although perhaps the bands would be weak. There are sometimes systematic differences among spectral types determined by various authors.

The moderate strength features selected for classification in our region $5800\mathring{A} - 6800\mathring{A}$ are apparently less affected by the T Tauri phenomena than the features in the blue usually used in the classification (Cohen and Kuhi 1979).

The classification presented here is only preliminary. Most of the time has been spent for the data reduction, which is the first important point to start for the quantitative measurements.

All the criteria and methods used will be checked with more accuracy. First of all we would underline that all the equivalent width of the lines used to obtain the relationship used for the spectral classification have been measured using the order by order normalized spectra. As we have described in section 3.2 we believe

that it is easier to make some mistake to identify the continuum points needed for the interpolation of the continuum than if you use the complete spectrum. Especially for the cooler stars the possibility of this obstacle is greater. Then what we propose is:

1. To normalize again the newly calibrated spectra processing the whole spectra at least for those stars where the order effects are not visible and the calibrations are the best. For the other stars, namely for the stars where the orders corrections are not good, we are forced to repeat the normalization order by order taking care the presence of bands in our spectral range.
2. After this delicate step we will repeat all the measurements of the equivalent width to obtain new curves of growth. In particular we hope to be able to construct the curves of growth using only the weakest absorption lines which are less affected by veiling. This means to use the linear branch of the curve of growth.
3. To check, using Jacoby *et al.*'s (1984) library, the spectral type of the two standard stars (HD 121217 and HD 260655) in order to construct a complete sequence of standard stars.
4. To measure with the new data reduction and with the greatest accuracy possible the strength of the TiO molecular bands for the stars cooler than K4.
5. To look for other criteria for the classification, like FeI/VI, using metallic lines ratios. Especially for lines with same excitation potential, which are presumibly formed in the same region and are similarly veiled, this could be a powerful criterion.
6. At the end to double-check the obtained results we would like to make the difference between the TTSs spectra and the standard stars spectra and minimize the residuals. This technique has been used by Finkenzeller and Barsi (1985). They use both difference and plots to make a comparison between

the spectra. The underlying assumption for this technique is always that the solar atmosphere of the program star and the standard resemble each other sufficiently that a direct comparison is meaningful. This is often taken to mean that they resemble each other at large optical depths, while the surface or extended parts of the atmosphere might be different. One can easly get a spurious ratio signal if the broadening mechanisms are sufficiently different, the temperature structures are never homologous, or the line formation physics is sufficiently different due to a variety of factors like gravity, abundances, atmospheric inhomogeneities, and so on. With this technique the standard star has to be convolved with a rotational function to match the $v * \sin i$ of the target star. After this, both objects, T Tauri and standard have to be moved to the same reference wavelength frame; namely that of the stellar photosphere. Unfortunately, the resulting wavelength shift also affects the ever-present telluric-lines. Ideally, those lines should be removed *ab initio*, but this is rather hard to accomplish. As results, virtual features can appear in the ratio plots. In this way any chromosphere activity will then show up as excessive emission, related to particular lines. This approach has been already performed by Finkenzeller and Barsi (1985) to study the activity and veiling of T Tauri stars. In Fig. 4.7 it is reported a their example where a nonrotating standard star, the same star convolved with a rotational function, a T Tauri star, and the direct ratio of these are plotted. The first striking point to be seen, in looking at the ratio plots, is the high degree to which the weak and and medium strength photospheric lines divide out. Only the stronger absorption features in the standard star appear to fill up in the T Tauri stars. This phenomenon is easily seen in the UV and infrared lines of neutral and ionized calcium, in the Balmer lines, in the sodium doublet, and in a number of iron lines. The stronger features are observed by Finkenzeller and Barsi (1985) in the IOS spectra at lower resolution. They note also

that the ratio spectra bear a close resemblance to solar chromospheric limb spectra. The lines which show up are those expected to be formed above the deep photosphere in the stellar atmosphere. The qualitative explanation is given in section 2.2.

References

Adams, F., Lada, C.J., Shu, F.: 1987, *Ap.J.*, **312**, 788.

Ahmad, I.A.: 1981, NASA IUE Newsletter, **14**, 129.

Appenzeller, I.: 1980, "Star Formation" Satuverny, Geneva Observatory Publ. A. Maederi and L. Martinet (eds).

Appenzeller, I.: 1983 *Rev. Mexicana Astron. Astroph.*, **7**, 151.

Appenzeller, I.: 1985, "Physica Scripta" T 11, 76.

Appenzeller, I., and Tscharnuter, W.: 1974, *Astr. Ap.*, **30**, 423.

Appenzeller, I., and Tscharnuter, W.: 1975, *Astr. Ap.*, **40**, 397.

Appenzeller, I., and Wolf, B.: 1977, *Astr. Ap.*, **54**, 73.

Appenzeller, I., Jankovics, I, and Krautter, J.: 1983, *Astr. Ap. Suppl.*, **53**, 291.

Appenzeller, I., Jankovics, I., Östreicher, R.: 1984, *Ap. J.*, **141**, 108.

Barker, P.K.: 1984, *Astron. J.*, **89**, 899.

Basri, G.: 1987, "The Fifth Cambridge Workshop on Cool Stars, Stellar System, and the Sun", Boulder, Colorado.

Basri, G.: 1987, Proc IAU Symp., **132**, 99 , Spite and Coyrel (eds).

Bastien, P. A.: 1982, *Astr. Ap. Suppl.*, **48**, 153.

Bastien, P. A., and Landstreet, I.D.: 1979, *Ap. J. (Letters)*, **229**, L 137.

Beckwith, S., Zuckerman, B., Skrutskie, M.F., Dyck, H.M.: 1984, *Ap. J.*, **287**, 793.

Bertout, C.: 1980, Proceed. of the 5th Europ. Reg. Meeting Liège, p. E 1.1.

Bertout, C.: 1984, *Rep. Prog. Phys.*, **47**, 111.

Bertout, C., Bsri, G., and Bouvier, J.: 1988, *Ap. J.*, preprint.

Bouvier, J. and Bertout, C.: 1985, *The Messenger*, **39**, 33.

Bouvier, J., Bertout, C., Benz, W., Mayor, M.: 1986, *Astr. Ap.* **165**, 110.

Calvet, N., Basri, G., Kuhi, L.V.: 1984, *Ap. J.*, **277**, 725.

Carbon, B.F., and Gingerich, O.: 1969, in "Theory and Observations of Normal Stellar Atmospheres", ed. Gingerich (Cambridge: MIT press).

Catherine, L.I., and Appenzeller, I.: 1986, "Exploring the Universe with the IUE Satellite", Y. Kondo Ed.

Cohen, M.: 1984, *Phys. Rep.*, **116**, 173.

Cohen, M.: 1988, "Pulsation and Mass Loss in Stars", Stalio and Willson (eds.), Kluwer Academic Publisher.

Cohen, M. and Kuhi L.V.: 1979, *Ap. J. Suppl. Series*, **41**, 743.

Cohen, M. and Schwartz, R.D.:1976, M.N.R.A.S., **174**, 137.

Cram, L.E.: 1979, *Ap. J.*, **234**, 949.

Cram, L.E., Giampapa, M. S. and Imhoff, C.L.: 1980, *Ap. J.*, **238**, 905.

D'Odorico, S., and Ponz, D.: 1984, *The Messenger*, **37**, 24.

D'Odorico, S., Ghigo, M. and Ponz, D.: 1987, "Atlas of the Thorium-Argon Spectrum for the ESO Echelle Spectrograph in the $\lambda\lambda 3400 - 9000 \AA$ Region" ESO Scientific Report No. 6.

Dumont, S., Heidmann, N., Kuhi, L.V., Thomas, R.N.: 1973, *Astr. Ap.*, **29**, 199.

Feigelson, E.D. and DeCampli, W.M.: 1981, *Ap. J.(Letters)*, **243**, L89.

Finkenzeller, U. and Mund, R.: 1984, *Astr. Ap. Suppl.*, **55**, 109.

Finkenzeller, U. and Jankovics, I.: 1984 *Astr. Ap. Suppl.*, **57**, 285.

Finkenzeller, U., Basri, G.: 1985, *The ESO Messenger*, **42**, 20.

Ford, W.K.Jr.: 1979, *Ann. Rev. Astr. and Ap.*, **17**, 189.

Franchini, M., Magazzu', A., Stalio, R.: 1988, *Astr. Ap.*, **189**, 132.

Gahm, G.F.: 1980, *Ap. J. (Letters)*, **242**, L163.

Giampapa, M.S.: 1984, in "Cool Stars, Stellar System and the Sun" eds. S.L.Baliunas and L. Hartmann, (Berlin: Springer - Verlag), p. 27.

Giampapa, M.S. and Imhoff, C.L.: 1985, "Protostars and Planets II (Black and Matthews, eds.)", Univ. of Arizona Press, 386.

Grasdalen, G.: 1972, *Ap. J.*, **173**, 353.

Gray, D.F.: 1976, "The Observational Analysis of Stellar Photosphres", (Wiley and Sons, New York).

Griffin, R.F.: 1968, "A Photometric Atlas of the Spectrum of Arcturus", Univ. Printing House, Cambridge.

Hartman, L., Edwards, S., and Avrett, E.: 1982, *Ap. J.*, **261**, 279.

Hartmann, L., Hewett, R., Stahler, S., Mathiew, R.: 1986, *Ap. J.*, **309**, 275.

Heidmann. N. and Thomas, R.N.: 1980, *Astr. Ap.*, **87**, 36.

Henize, K.G.: 1954, *Ap. J.*, **119**, 459.

Henize, K.G.,and Mendoza, E.E.: 1973, **Ap. J.**, **180**, 115.

Herbig, G.H.: 1962, *Adv. Astr. Ap.*, **1**, 47.

Herbig, G.: 1970, *Mem. Soc. R. Sci. Liège*, **19**, 13.

Herbig, G.H.: 1973, *Ap. J. Suppl.* **4**, 337.

Herbig, G.H.: 1977, *Ap. J.*, **214**, 747.

Herbig, G.H., and Raho N.K.: 1972,*Ap. J.*, **174**, 401.

Herbig, G.H., and Goodrich, R.W.: 1986,*Ap. J.*, **309**, 294.

Hoffmeister, C.: 1962, Zs. f. Astrophys., 55.

Houk, N.: 1978, "University of Michigan catalogue of two-dimensional spectral types for the HD stars", Vol. 2, Ann Arbor, Michigan.

Houk, N.: 1982, "University of Michigan catalogue of two-dimensional spectral types for the HD stars", Vol. 3, Ann Arbor, Michigan.

IRAF, user Handbook: 1987, Version June 23 - National Optical Astronomy Observatories, Tucson.

Jacoby, G.H. and Hunter D.A.: 1984, *Ap. J. Suppl. Ser.*, **56**, 257.

Joy, A.H.: 1945, *Ap. J.*, **102**, 168.

Joy, A.H.: 1949 *Ap. J.*, **110**, 424.

Kitchin, C.R.: 1984 "Astrophysical Techniques" Adam Hilger Ltd, Bristol.

Kuan, P.: 1975, *Ap. J.*, **202**, 425.

Kuhi, L.V.: 1964, *Ap. J.*, **140**, 1409.

Kuhi, L.V.: 1970, *Mem. Soc. Roy. Sci. Liège*, **19**, 295.

Kuhi, L.V.: 1974, *Astr. Ap. Suppl.*, **15**, 47.

Kuhi, L.V.: 1983, *Rev. Mexicana Astron. Astroph.*, **7**, 127.

Larson, R.B. and Starrfield, S.: 1971 *Astr. Ap.*, **13**, 190.

Linden-Bell, D. and Pringle, J.E.: 1974, M.N.R.A.S., **168**, 603.

MacKay C.D.: 1986, *Ann. Rev. Astr. and Ap.*, **24**, 255.

Mendoza V., E.E.: 1966, *Ap. J.*, **143**, 1010.

Mendoza V., E.E.: 1968, *Ap. J.*, **151**, 977.

MIDAS, Munich Image Data Analysis System: 1988, ESO Operating Manual.

Minnaert, M.G.J., Mulders, G.F.W., Houtgast, J.: 1940, "Photometric Atlas of the Solar Spectrum", Sterrewacht Sonnenberg, Utrecht.

Montmerle, T., Koch-Miramond, L., Falgarone, E. and Grindley, J.E.: 1983, *Ap. J.*, **269**, 182.

Moore, C.E., Minnourt, M.G.J., Houtgast, J.: 1966, *Nat. Bureau of Standars Monographs.*, No. 61.

Mundt, R.: 1979, *Ap. J.*, **151**, 977.

Mundt, R.: 1984, *Ap. J.*, **280**, 749.

Mundt, R., and Giampapa, M.S.: 1982, *Ap. J.*, **256**, 156.

Ponz, D., and Brinks, E.: 1986, *The Messenger*, **43**, 31.

Rydgren, A.E., Strom, S.E., and Strom, K.M.: 1976, *Ap. J. Suppl. Ser.*, **30**, 307.

Rydgren, A.E., and Vrba, F.J.: 1981, *Ap. J.*, **86**, 1069.

Schwartz, R.D.: 1977, *Ap., J. Suppl. Ser.*, **35**, 161.

Shu, F.H., Lizano, S., Adams, F.C., Ruden, S.P.: 1988, "Pulsation and Mass Loss in Stars", Stalio and Willson (eds.), Kluwer Academic Publishers.

Spitzer, L.: 1968, "Diffuse Matter in Space", New York.

Stahler, S.W.: 1983, *Ap. J.*, **274**, 222.

Stahler, S.W., Shu, F.N. and Taam, R.E.: 1980, *Ap. J.*, **241**, 637.

Stone, R.P.S.: 1977, *Ap. J.*, **218**, 767.

Strom, S.E., Strom, K.M., Yast, J., Carrasco, L. and Grasdalen, G.: 1972, *Ap. J.*, **173**, 353.

Strom, S.E., Strom, K.M., Grasdalen, G.L.: 1975, *Ann. Rev. Astron. Ap.*, **13**, 187.

Timothy, J.G.: 1983, P.A.S.P., **95**, 810.

Ulrich, R.K.: 1976, *Ap. J.*, **210**, 377.

Ulrich, R.K.: 1983, *Ap. J.*, **267**, 199.

York, D.G., Jenkins, E.B., Zucchino, P., Lawrance, J.L., Long, D., Songaila, A.: 1981, Proceedings of the SPIE, **290**, 202.

Vernazza, J.E., Avrett, E.H., and Loeser, R.: 1981, *Ap. J. Suppl.*, **45**, 635.

Vogel, S.N., and Kuhi, L.Y.: 1981, *Ap. J.*, **245**, 960.

Walker M.F.: 1972, *Ap. J.*, **175**, 546.

Walker, M.F.: 1978, *Ap. J.*, **224**, 546.

Walker, M.F.: 1980, P.A.S.P. **92**, 66.

Walter, F.M. and Kuhi, L.V.: 1981, *Ap. J.*, **250**, 254.

Winkler, K. H., and Newman, M.N.,: 1980, *Ap. J.*, **236**, 201.

Wolf, B., Appenzeller, I., and Bertout, C.: 1977, *Astron. Ap.*, **58**, 163.

Acknowledgements

I am specially thankful to my supervisor, prof. R. Stalio, for his guidance and encouragement.

I would like also to thank Dr.s M. Cohen, S. D'Odorico, T. Lago, A. Magazzù, J. Miller and A. Richichi for usuful discussions in the course of this work.

The computations were carried out on the VAX 11/780 at ESO (Garching) and on the VAX 11/750 of the ASTRONET POLE of Trieste, and at the SUN workstation of the IRAF center at KPNO.

Appendix A

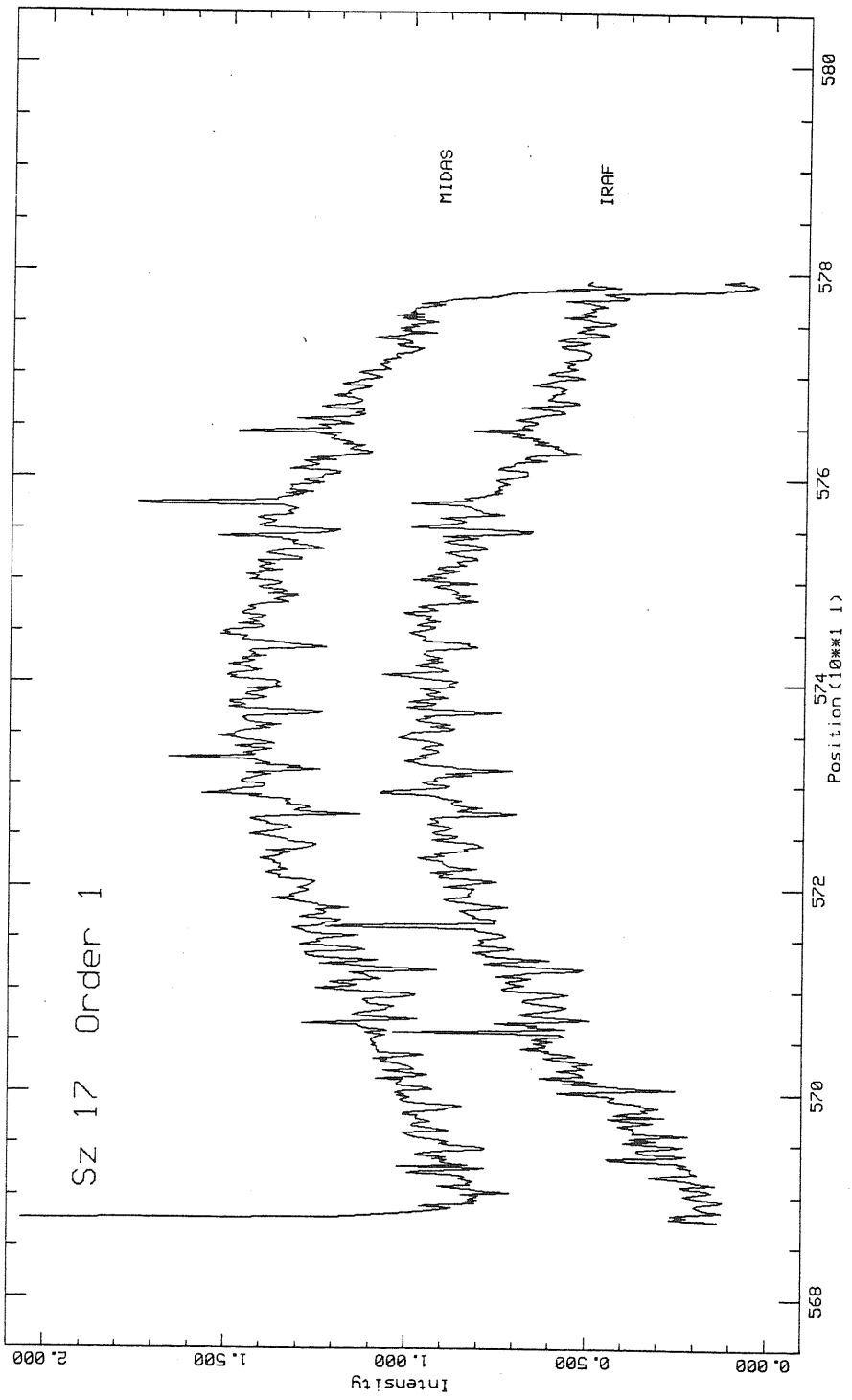
MIDAS
IRAF
Sz 17 Order 1
Intensity
0.000
0.500
1.000
1.500
2.000
568
570
572
574
576
578
580
Position (10**1 1)

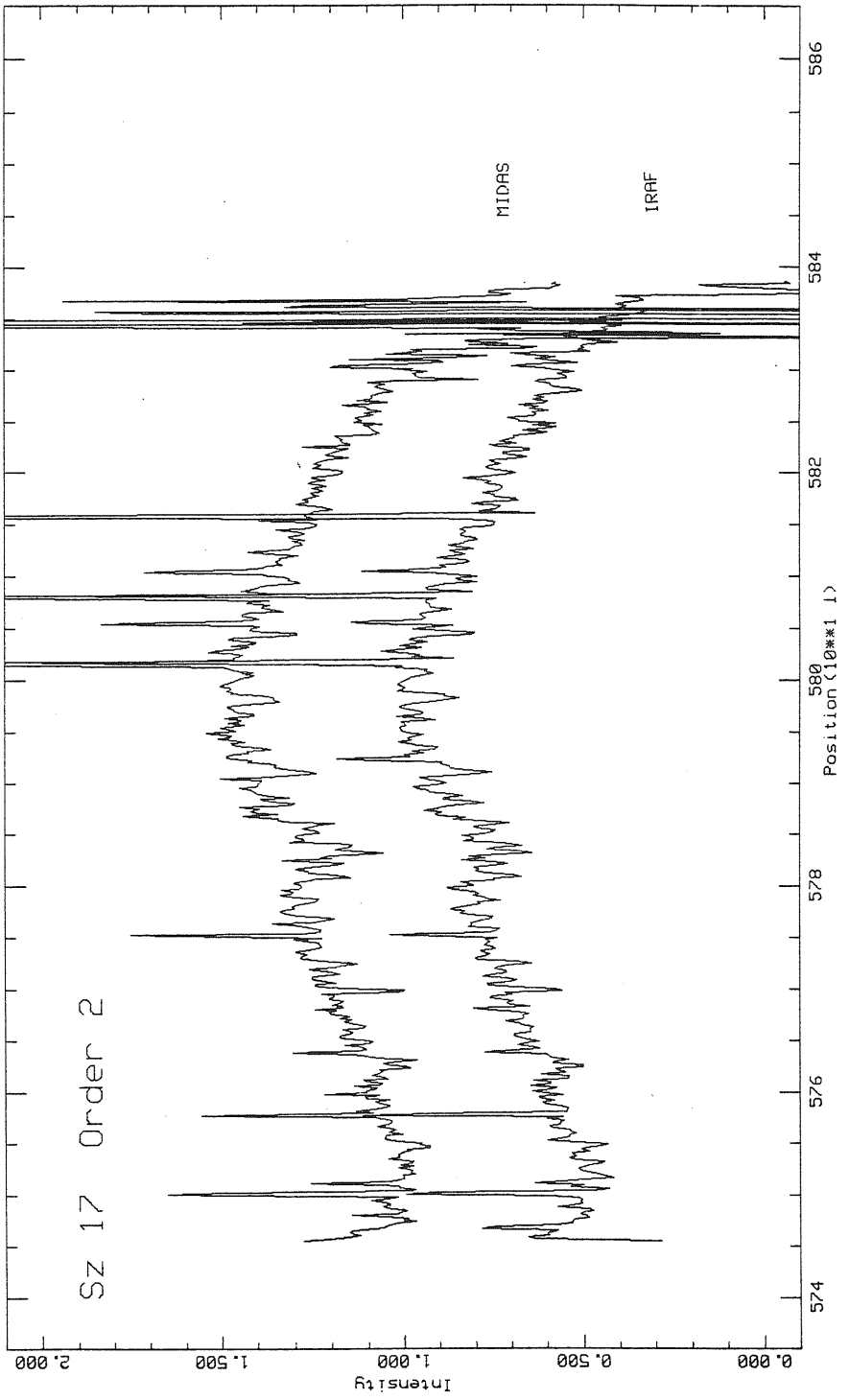
Sz 17 Order 2
MIDAS
IRAF
Intensity
0.000
0.500
1.000
1.500
2.000
574
576
578
580
582
584
586
Position (10**1 1)

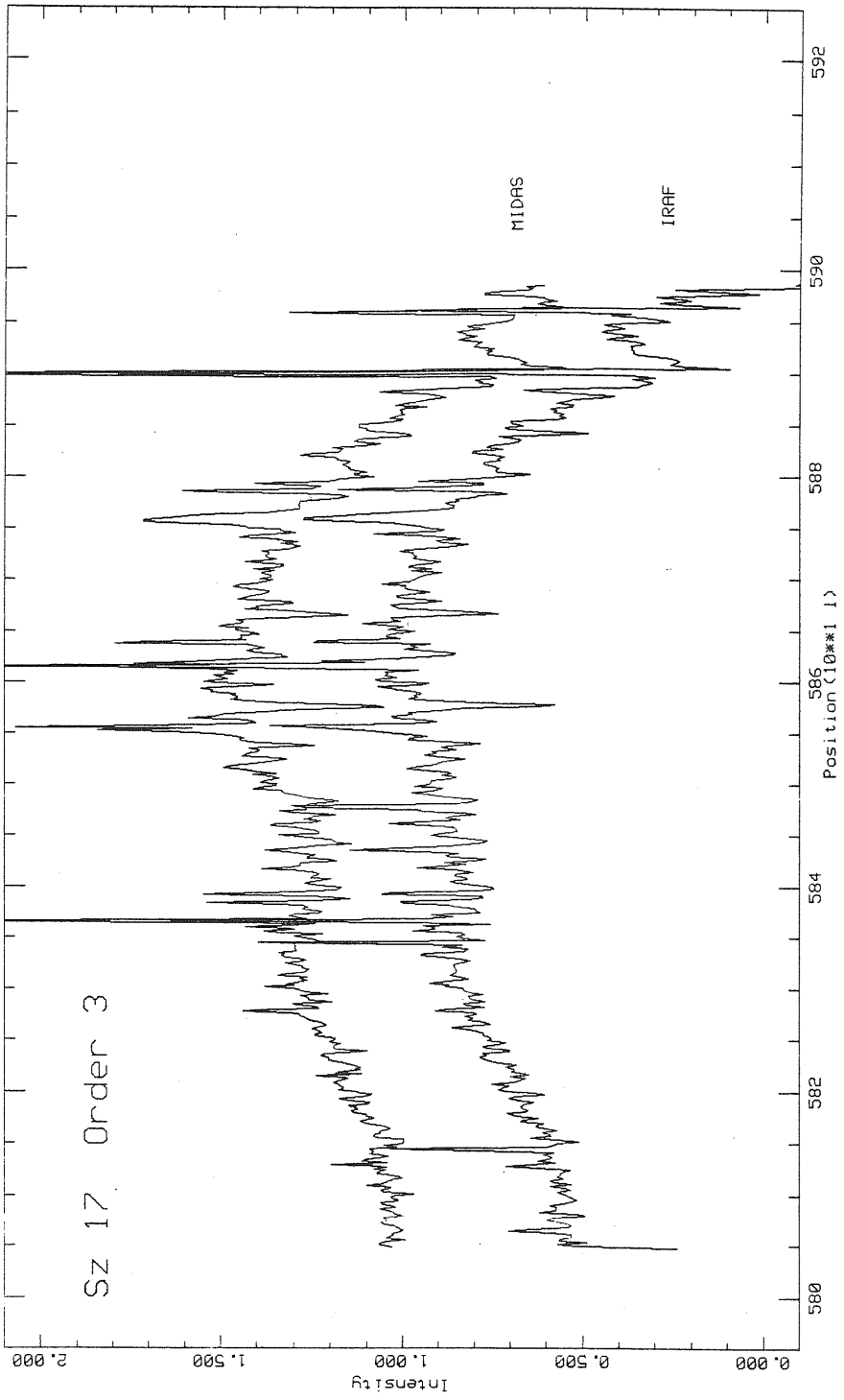
Sz 17 Order 3
MIDAS
IRAF
Intensity
0.000
0.500
1.000
1.500
2.000
Position(10**1 1)
580
582
584
586
588
590
592

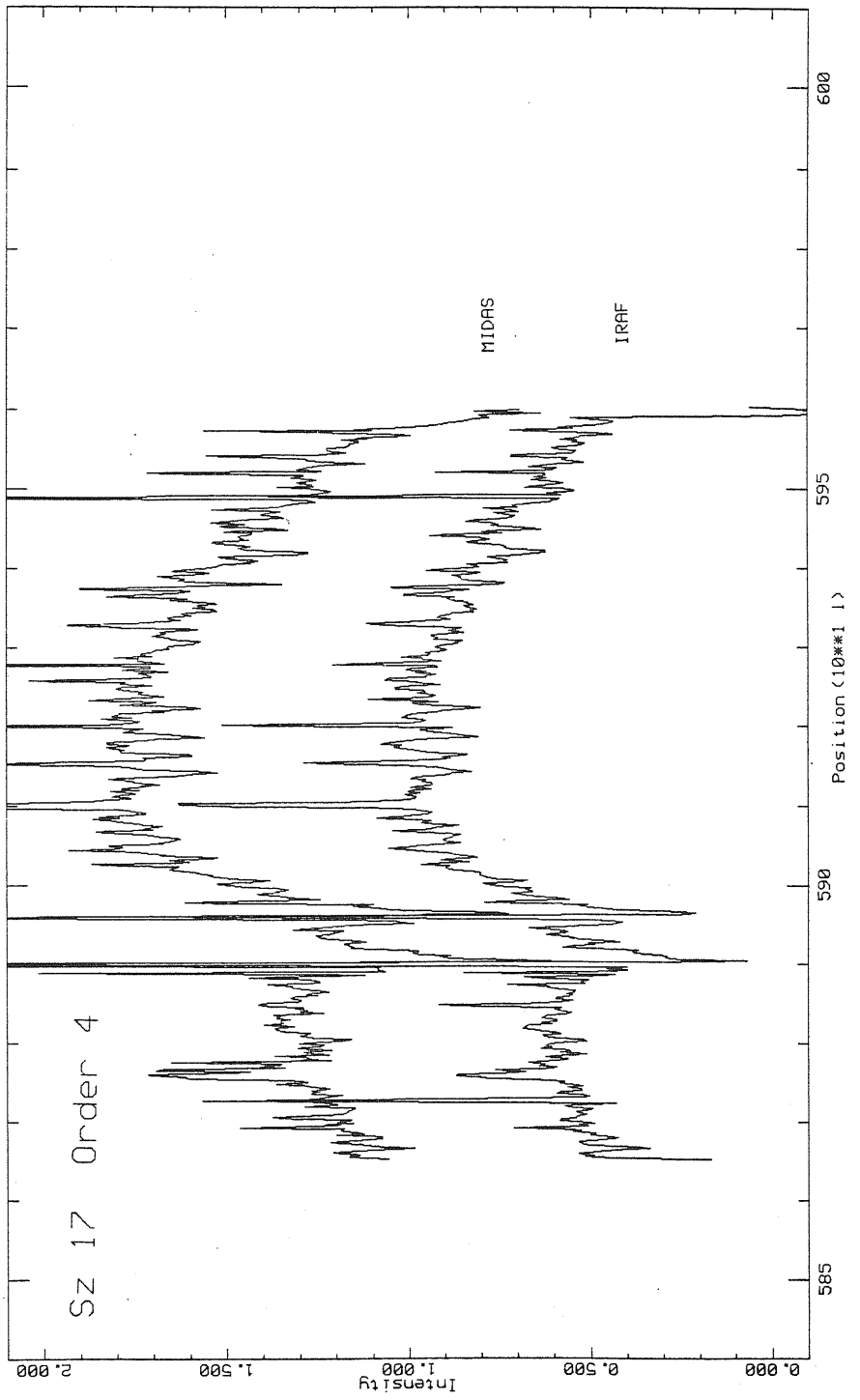
Sz 17 Order 4
MIDAS
IRAF
Intensity
0.000
0.500
1.000
1.500
2.000
585
590
595
600
Position (10**1 1)

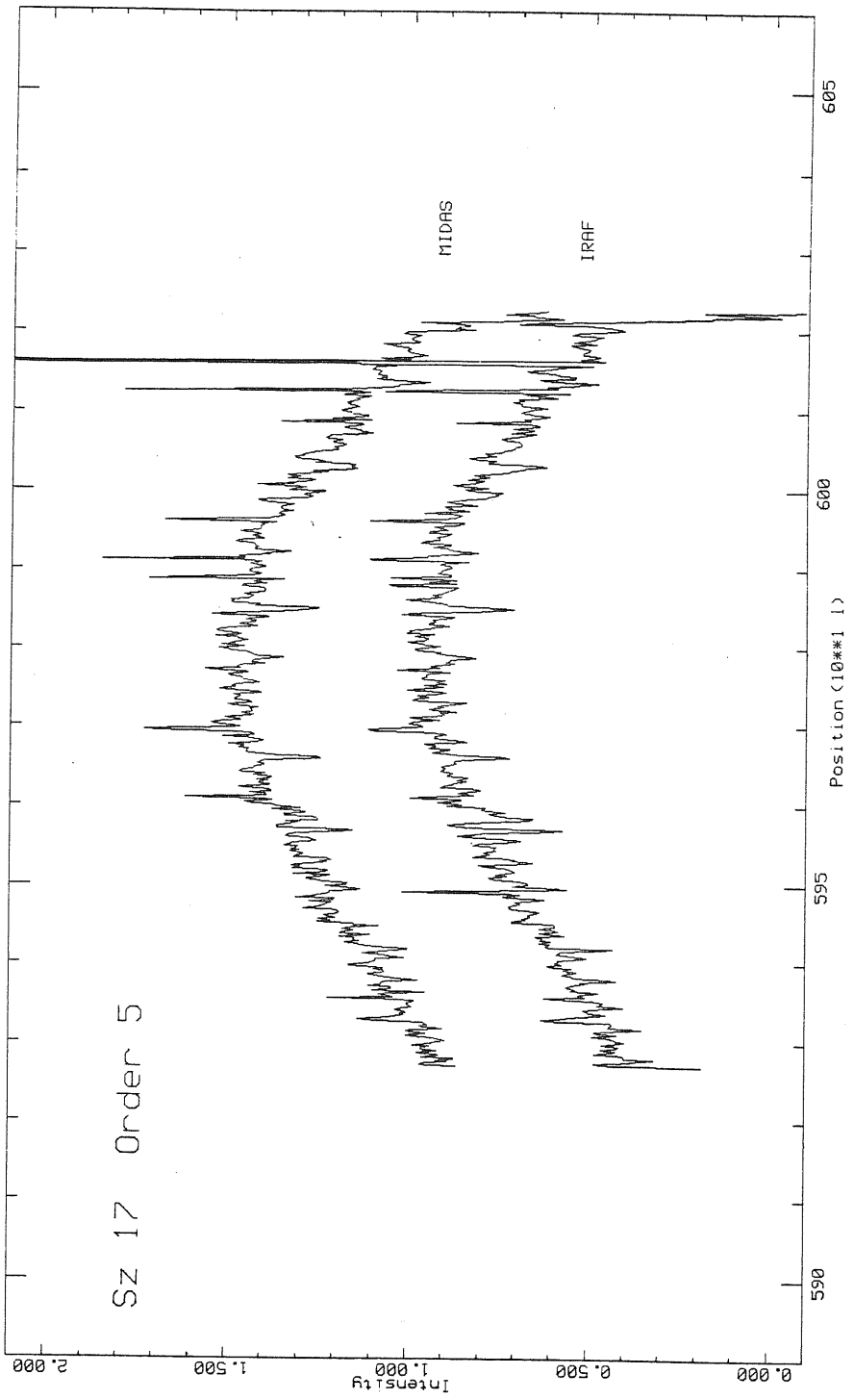
Sz 17 Order 5
MIDAS
IRAF
Intensity
0.000
0.500
1.000
1.500
2.000
590
595
600
605
Position(10**1 1)

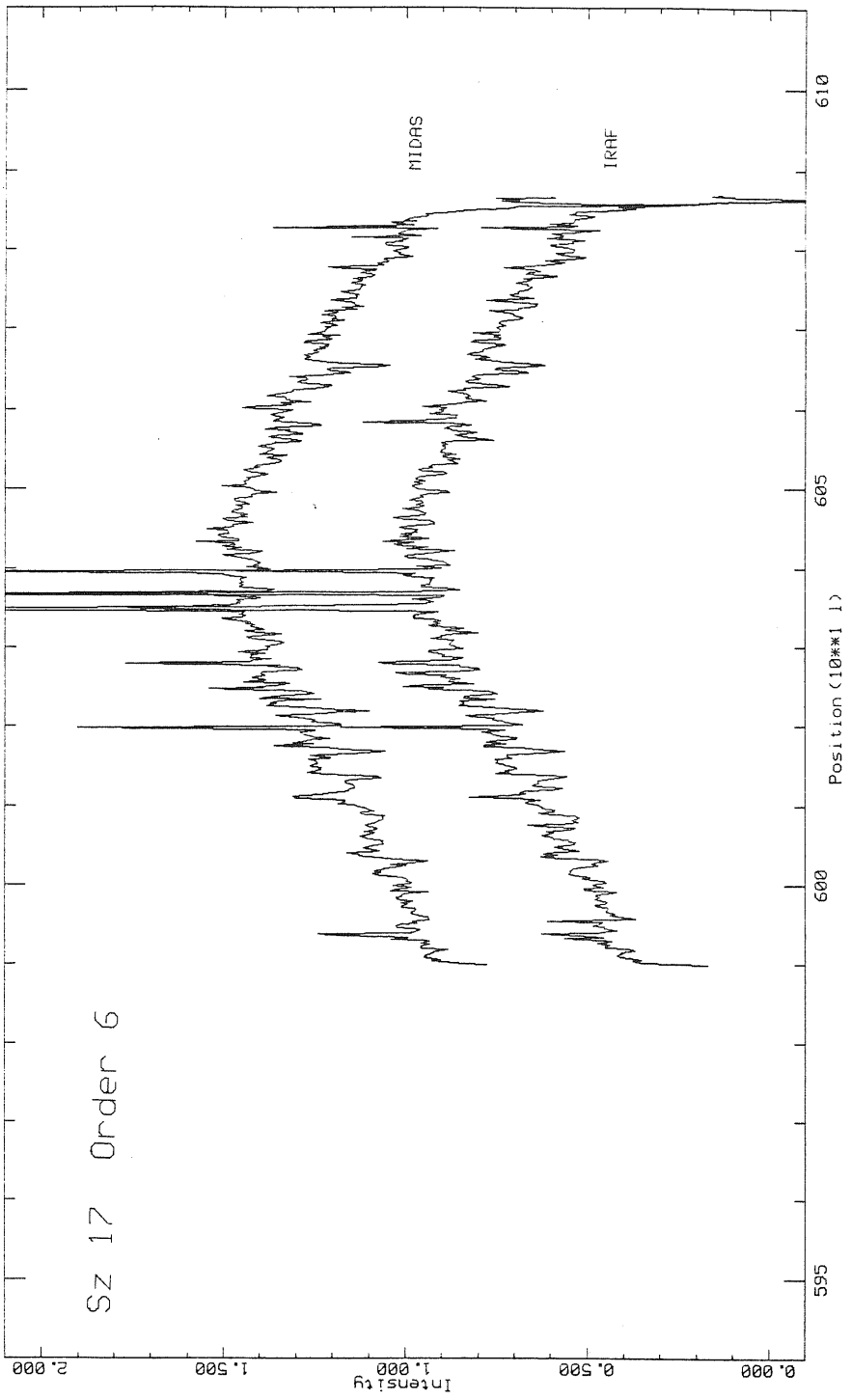
MIDAS
IRAF
Sz 17 Order 6
Intensity
0.000
0.500
1.000
1.500
2.000
595
600
605
610
Position (10**1 1)

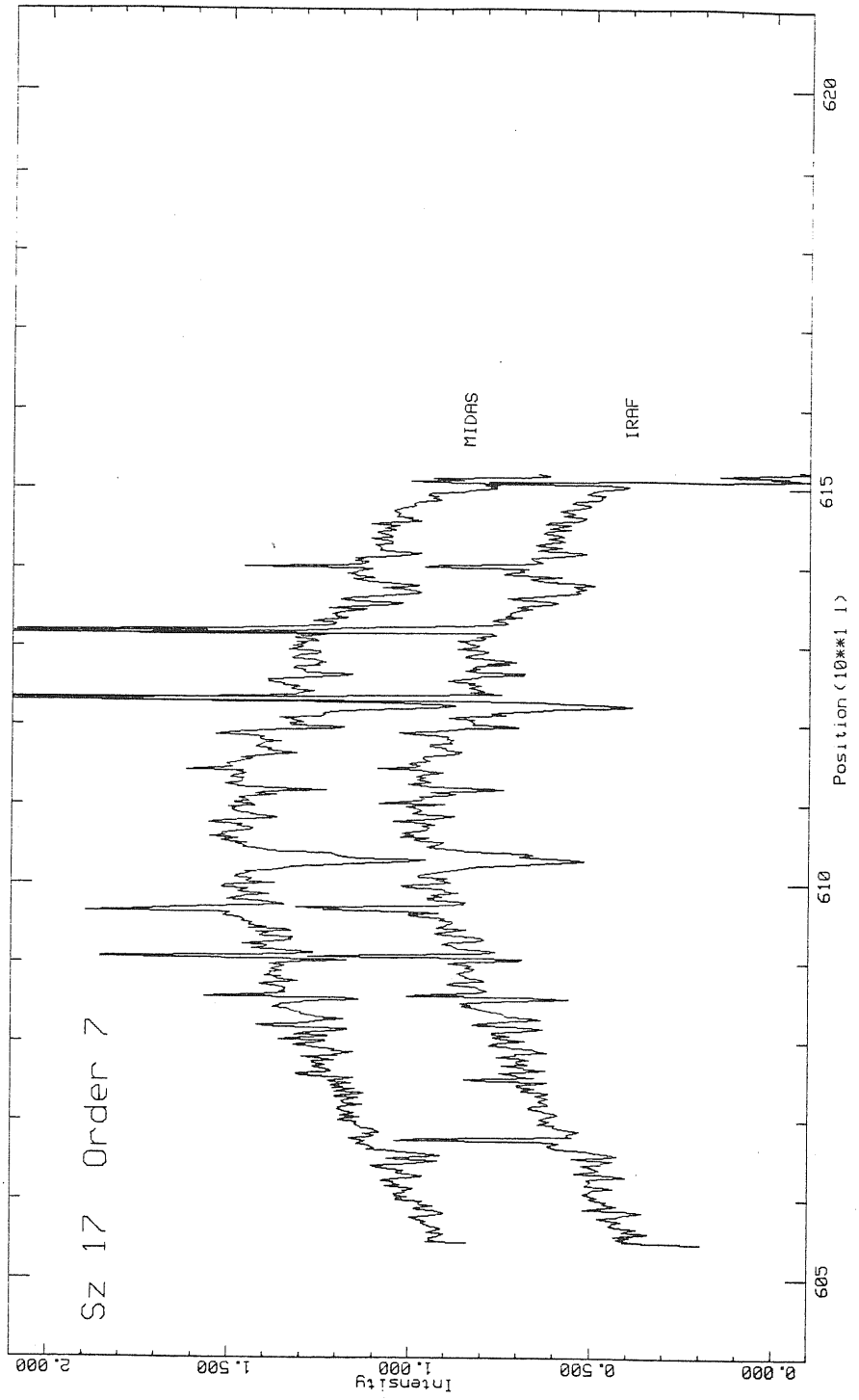
Sz 17 Order 7
MIDAS
IRAF
Intensity
0.000
0.500
1.000
1.500
2.000
605
610
615
620
Position (10**1)

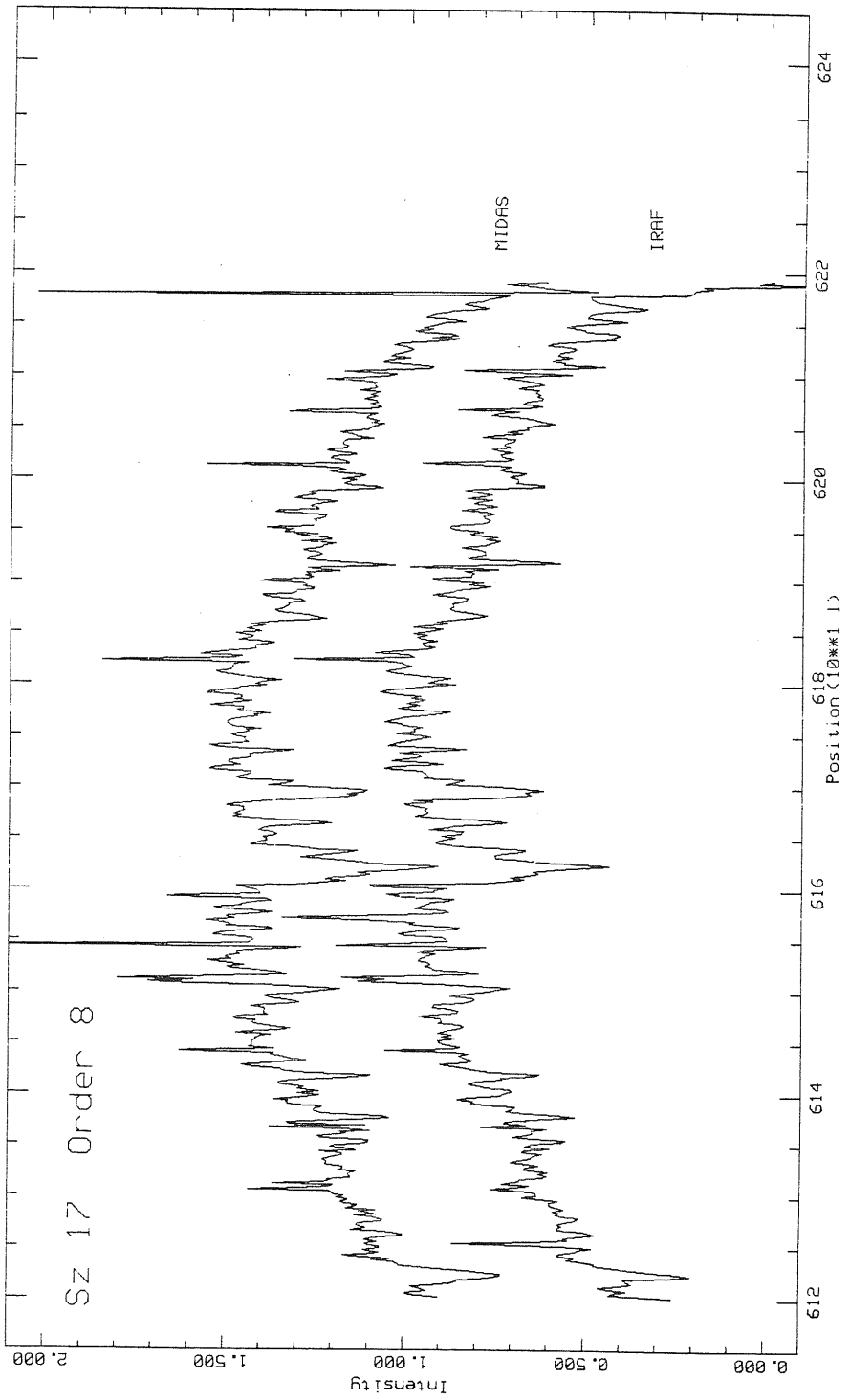
Sz 17 Order 8
MIDAS
IRAF
Intensity
0.000
0.500
1.000
1.500
2.000
612
614
616
618
620
622
624
Position(10**1)

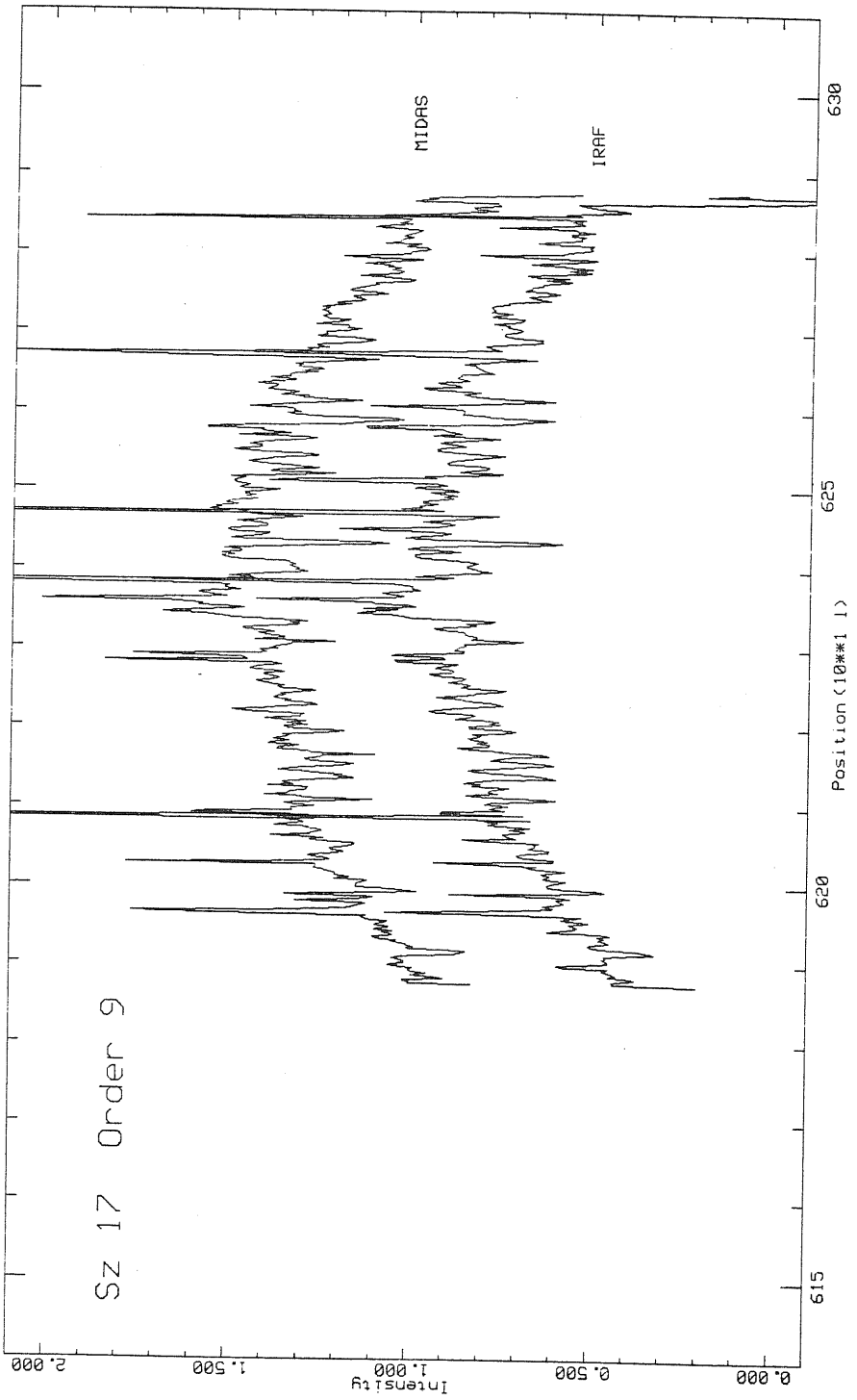
MIDAS
IRAF
Sz 17 Order 9
Intensity
0.000
0.500
1.000
1.500
2.000
615
620
625
630
Position(10**1 1)

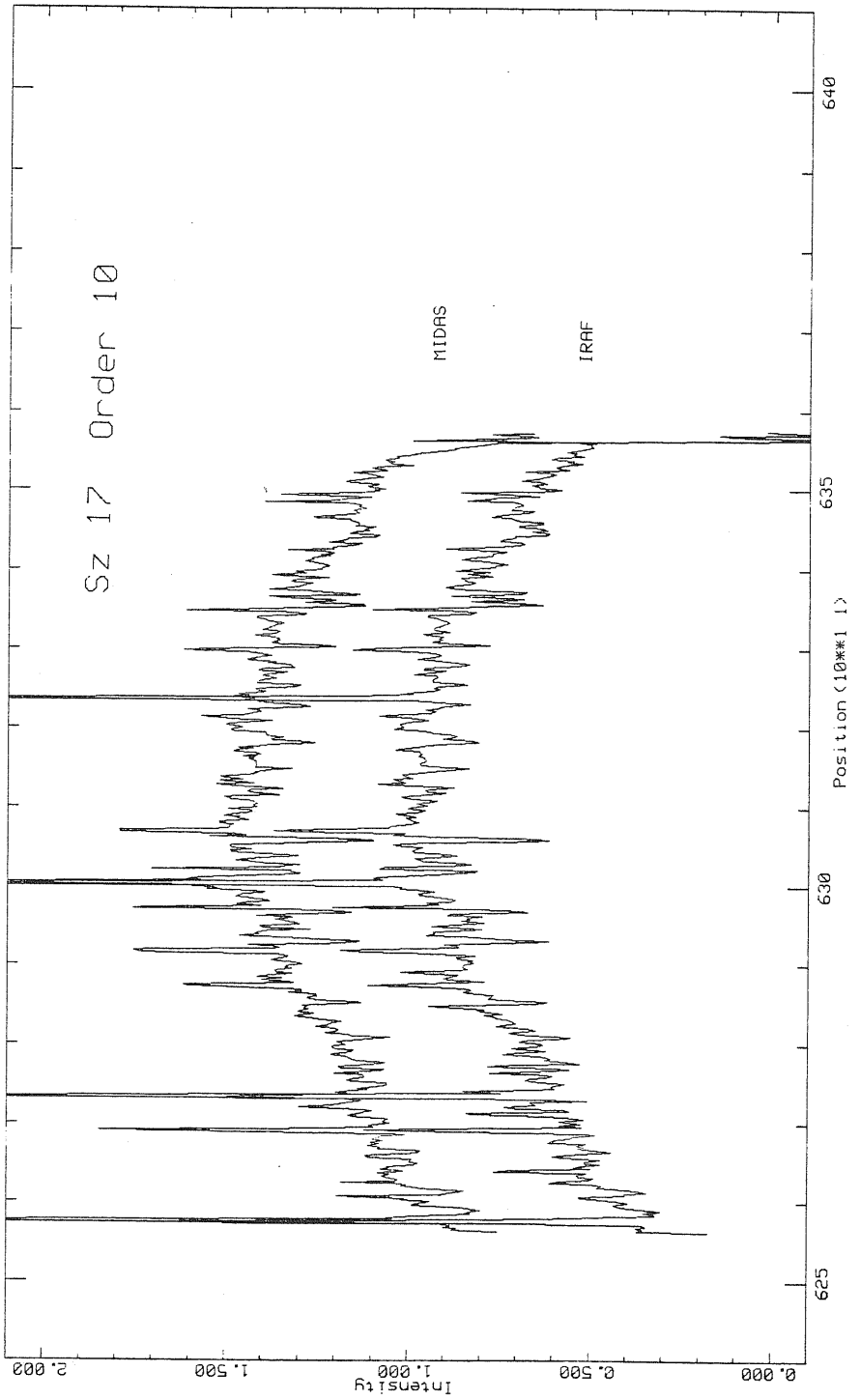
Sz 17 Order 10
MIDAS
IRAF
Intensity
0.000
0.500
1.000
1.500
2.000
625
630
635
640
Position (10**1)

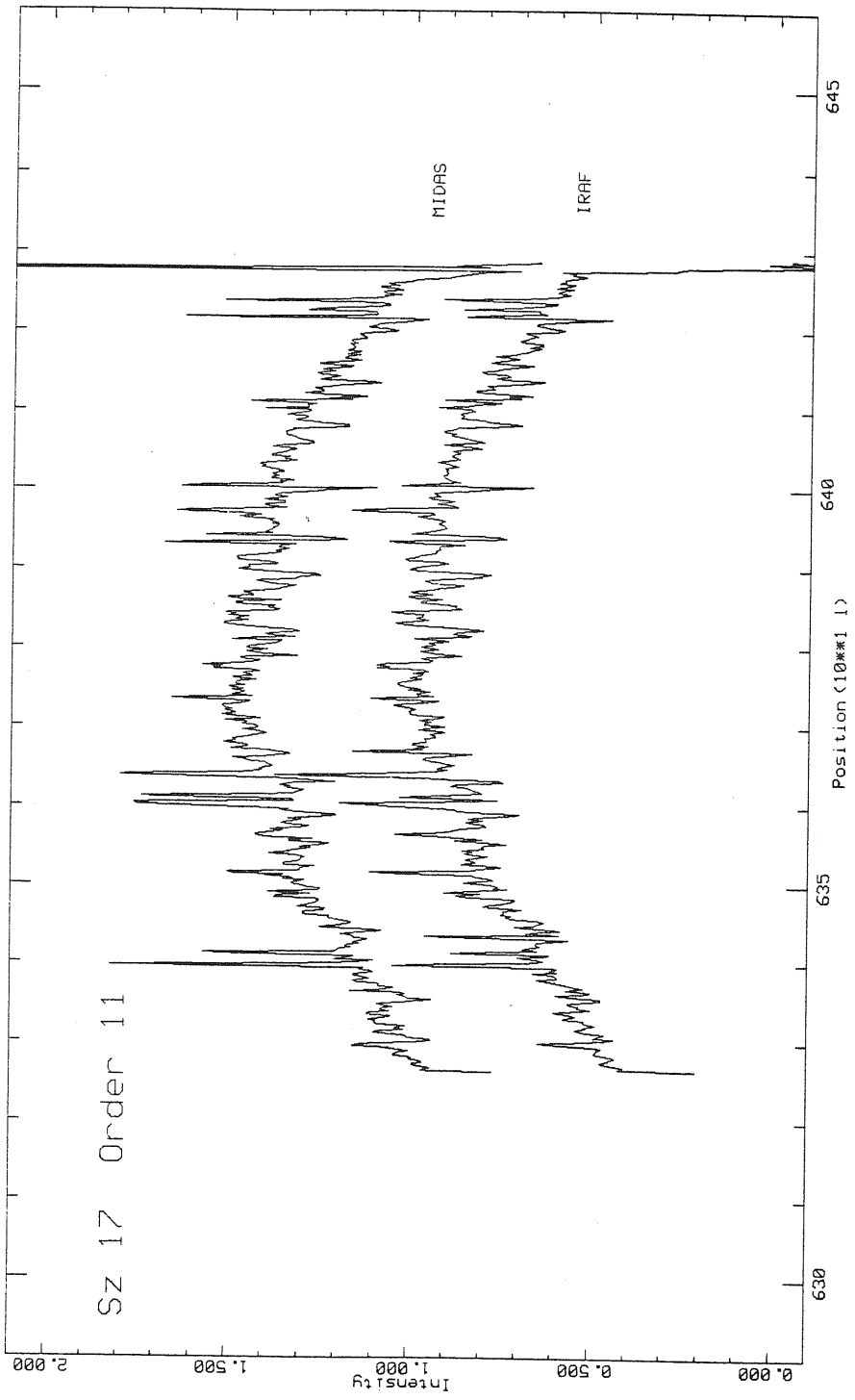
MIDAS
IRAF
Sz 17 Order 11
Intensity
0.000
0.500
1.000
1.500
2.000
630
635
640
645
Position (10**1 1)

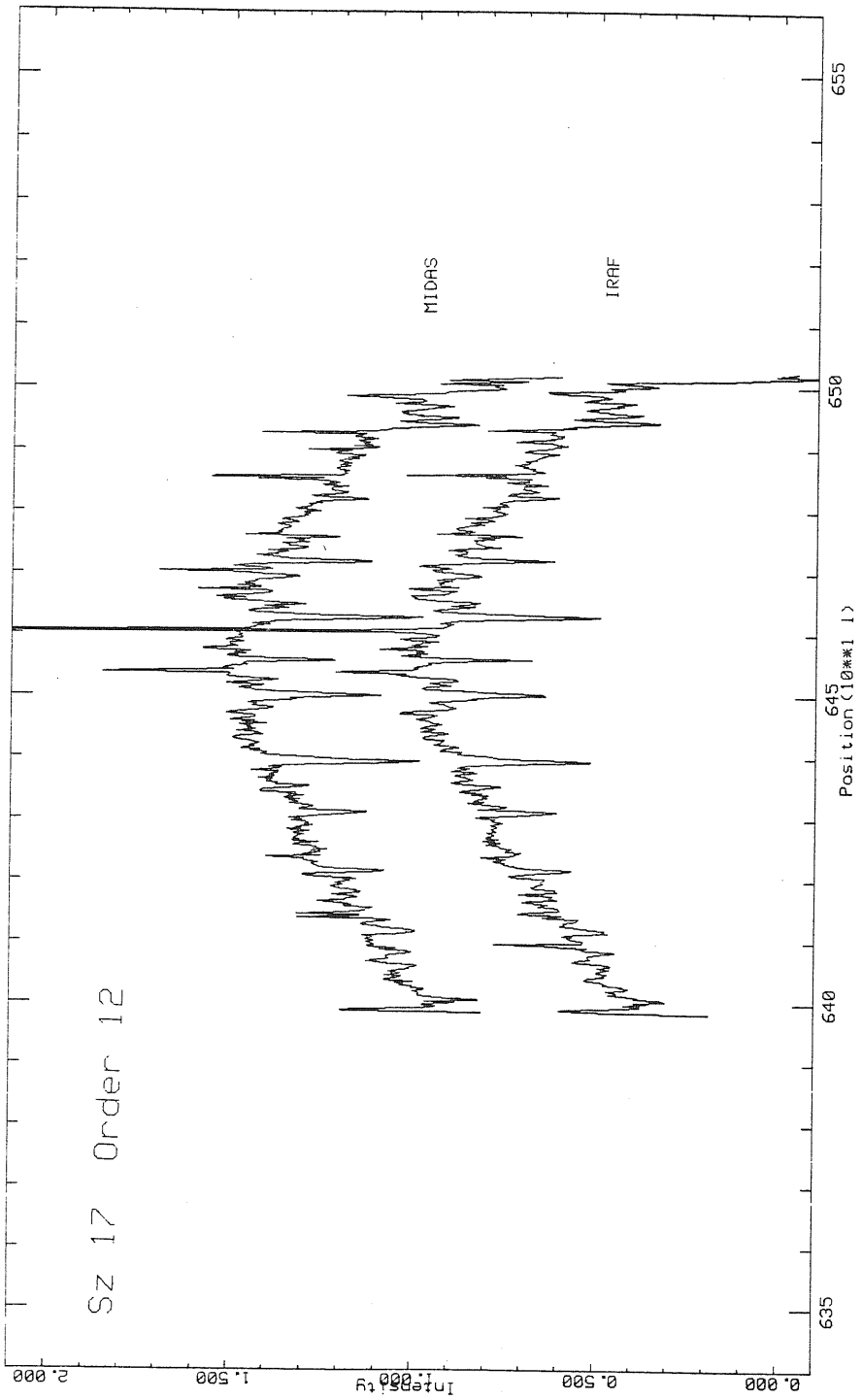
Sz 17 Order 12
MIDAS
IRAF
Intensity
0.000
0.500
1.000
1.500
2.000
635
640
645
650
655
Position (10**1)

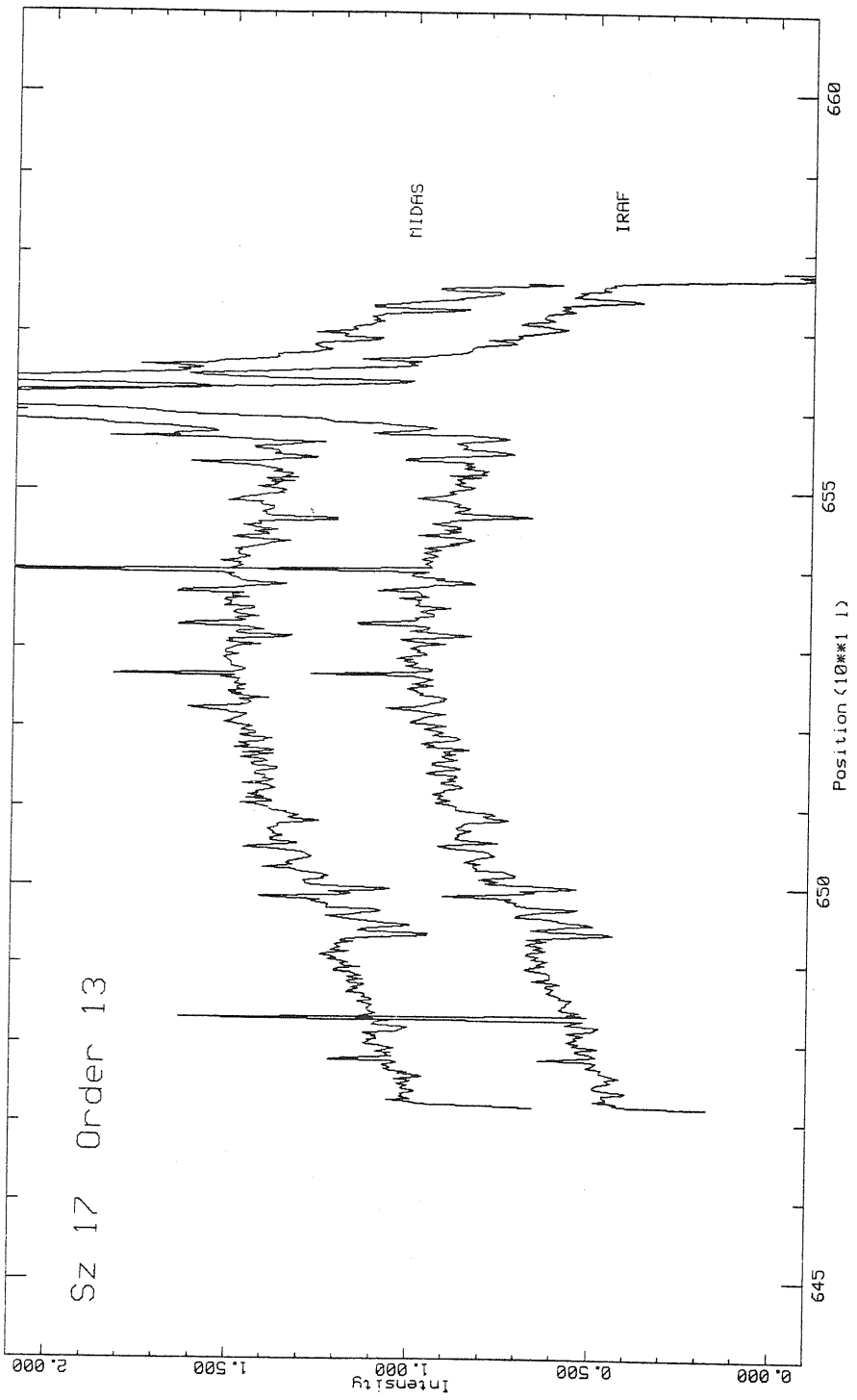
Sz 17 Order 13
MIDAS
IRAF
Intensity
0.000
0.500
1.000
1.500
2.000
645
650
655
660
Position (10**1 1)

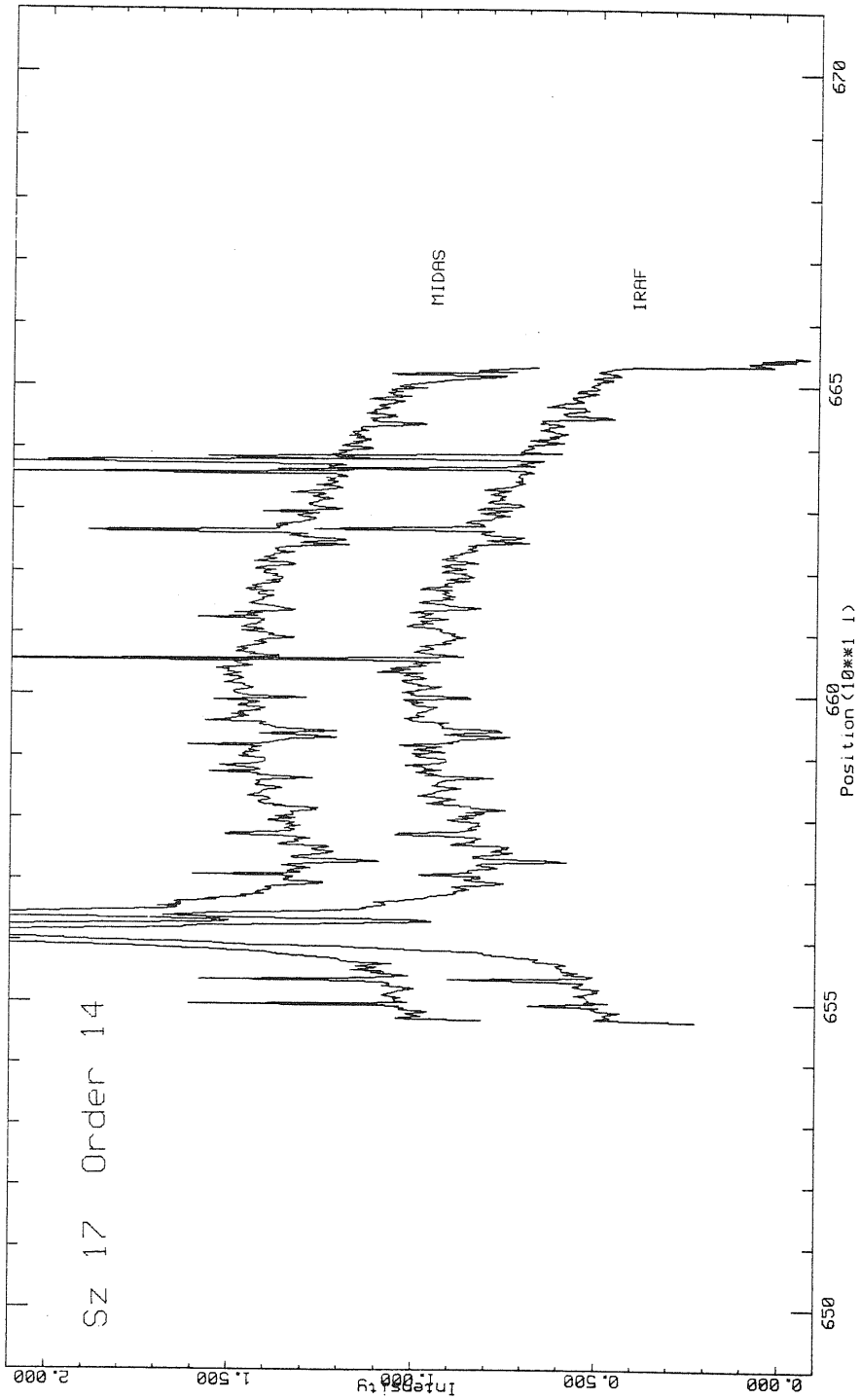
Sz 17 Order 14
MIDAS
IRAF
Intensity
0.000
0.500
1.000
1.500
2.000
650
655
660
665
670
Position (10**1)

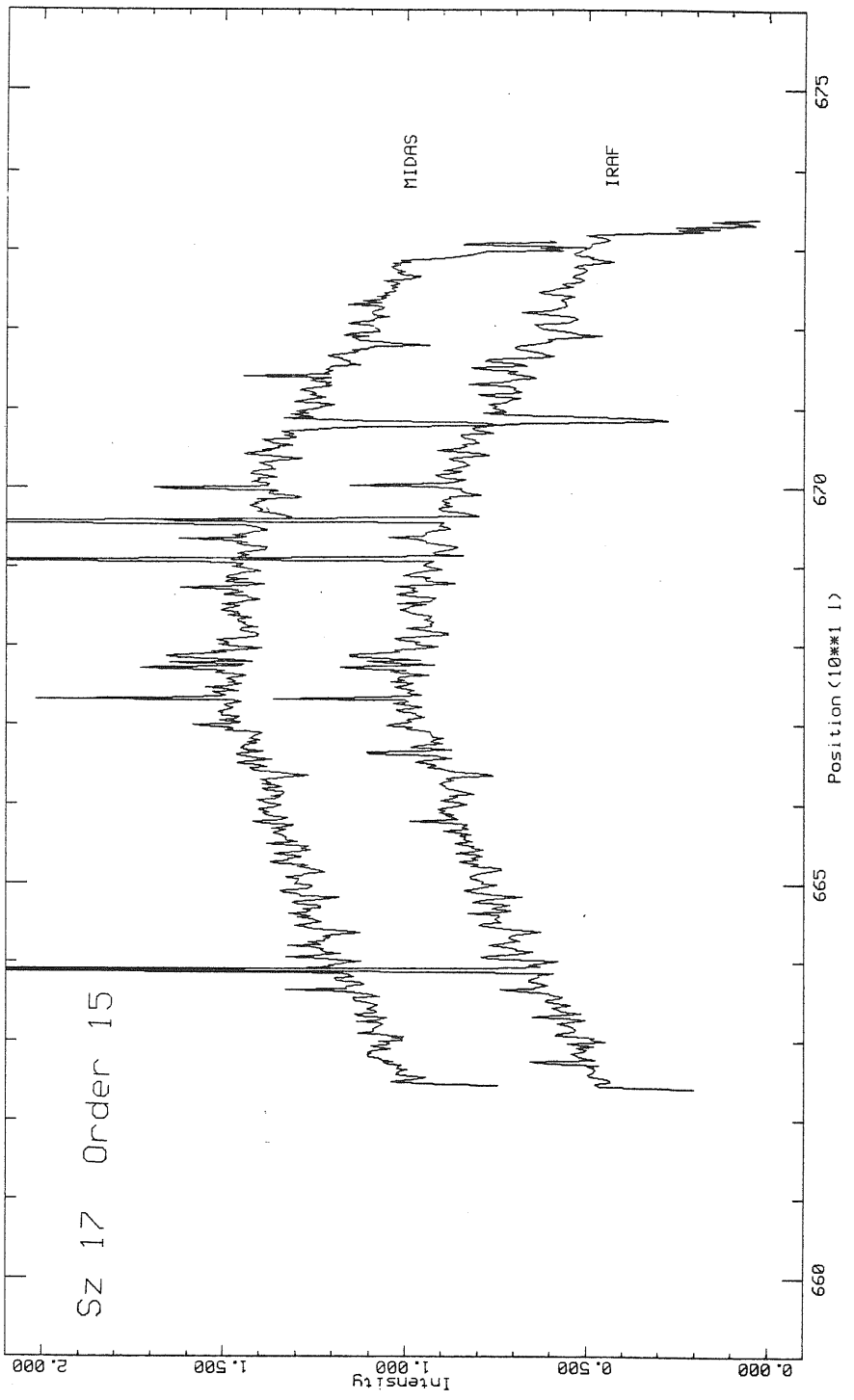
Sz 17 Order 15
MIDAS
IRAF
Intensity
0.000
0.500
1.000
1.500
2.000
660
665
670
675
Position (10**1)